Rising from the ground

Distributed drag parameterization of urban environments for numerical weather prediction

Submitted for the degree of Doctor of Philosophy by

Birgit S. Sützl

Department of Civil and Environmental Engineering
Imperial College London

January 2021

This thesis was supervised by
Dr Maarten van Reeuwijk and Dr Gabriel Rooney

I declare that this thesis presents my own work, and any work or contribution made by others is referenced appropriately.

Abstract

Urban environments in numerical weather prediction models are currently parameterised as part of the atmosphere-surface exchange at ground level. The vertical structure of buildings is represented by the average height, which does not account for heterogeneous building forms at the subgrid level. This thesis investigates aerodynamic effects of subgrid heterogeneity and develops a distributed drag parameterization that represents buildings at their real height.

Urban flow at neighbourhood scale is studied using large-eddy simulations of idealised, heterogeneous urban morphologies with identical building plan area index and frontal area index. Large differences in estimated roughness parameters and total canopy drag, which are strongly correlated to the maximum height and height variability of the buildings, mean-wind profiles and vertical momentum transport suggest that subgrid heterogeneity is inadequately represented by current models.

A height-dependent frontal area function is introduced to capture a vertical urban morphology profile with full height extent and variability. The morphology profiles correlate to the distinct distributed-drag profiles of the simulations, and a drag parameterization was derived by a third-order polynomial function of the morphology profiles. Morphology profiles were calculated for Greater London and parameterised by an exponential distribution with the ratio of maximum to mean building height as parameter.

A case study with the high-resolution London Model and the new drag parameterization appears to capture more realistic features of the urban boundary layer compared to the standard parameterization. The simulation showed increased horizontal spatial variability in total surface stress, identifying a broad range of morphology features (densely built-up areas, high-rise building clusters, parks and the river). Vertical effects include heterogeneous wind profiles, extended building wakes, and internal boundary layers. This thesis demonstrates the potential of height-distributed urban parameterizations to improve urban weather forecasting, with further research into distribution of heat- and moisture-exchange necessary.

Acknowledgements

I would like to thank my supervisors Maarten van Reeuwijk and Gabriel Rooney for their support and guidance throughout the duration of my PhD. Their insight on the subject area and enthusiasm for this project have been invaluable to the work presented in this thesis. Thank you Maarten for three years of weekly meetings and discussions, for keeping me on track by teaching me where to put my focus and energy, and how to not waste time on my perfectionism. Special thanks to Gabriel for his support during my summer placement at the Met Office, where our daily meetings helped me steer through the labyrinth of the Met Office code, and for enabling me to keep the connection to the Met Office afterwards.

I would also like to thank everyone on the uDALES team, it has been a great experience to collaborate on improving the model and working towards making it publicly available. In particular I would like to thank Tom Grylls for his help in setting me up with the code in the beginning of my project, and valuable discussions afterwards. There are many other people who helped me in my understanding of the research area, first and foremost my co-authors Anke Finnenkoetter, Sylvia Bohnenstengel, and Sue Grimmond, and other researchers I had insightful discussions with at conferences and the Urban Fluid Mechanics Special Interest Group meetings.

This work was supported by the Engineering and Physical Sciences Research Council Mathematics of Planet Earth Centre for Doctoral Training (MPE CDT, grant number EP/L016613/1). The computational resources for this work were provided by the Imperial College London High Performance Computing facilities. The support from the MPE CDT was a great resource over the past four years, and special thanks go to my cohort, who have been such a reliable network and provided continuous encouragement. Thanks to my colleagues and friends from the lab who shared the ups and downs of the PhD experience with me.

Finally I would like to thank my family and Mario, for their unconditional support and their confidence in my endeavours. Thank you Mario for providing entertainment after long days of work in the past year when seeking distraction outside home was not possible, and for all the homemade sourdough bread.

Copyright

Contents

List of figures

List of tables

List of algorithms

List of abbreviations and symbols

Abbreviations

a.g.l.	above ground level
ABL	atmospheric boundary layer
CFL	Courant–Friedrichs–Lewy (criterion)
CI	City neighbourhood
CW	Canary Wharf neighbourhood
DALES	Dutch Atmospheric Large-Eddy Simulation model
DNS	direct numerical simulation
ISL	inertial sublayer
JULES	Joint UK Land Environment Simulator
K0	JULES with Kanda et al. (2013) parameterization
K1	JULES with modified Kanda et al. (2013) parameterization
K2	JULES with modified Kanda et al. (2013) parameterization
LB	Littlebrook Power Station neighbourhood
LES	large-eddy simulation
LIDAR	light detection and ranging

LM	Met Office London Model
MD	JULES with MacDonald et al. (1998) parameterization
ML	mixed layer
MORUSES	Met Office–Reading Urban Surface Exchange Scheme
MR	Marylebone Road neighbourhood
NK	North Kensington neighbourhood
NWP	numerical weather prediction
OC	Oxford Circus neighbourhood
RAL1-M	regional atmosphere and land configuration for mid-latitudes
RANS	Reynolds-averaged Navier–Stokes equations
RSL	roughness sublayer
SGS	subgrid-scale
SH	Shard neighbourhood
TEB	Town Energy Budget model
UBL	urban boundary layer
UCL	urban canopy layer
uDALES	DALES for the urban environment
UKV	Met Office forecasting model for the United Kingdom
ULG	Urban Landscape Generator
UM	Met Office Unified Model
WA	Wapping neighbourhood

Constants

κ	von Kármán constant	0.4

σ	Stefan–Boltzmann constant	6.7×10^{-8} W m^{-2} K^{-4}
g	standard acceleration due to gravity	9.8 m s^{-2}

Subscripts

$_i$	Euclidean coordinate direction ($_x$, $_y$ or $_z$)
$_j$	second Euclidean coordinate direction ($_x$, $_y$ or $_z$)
$_k$	another subscript letter
$_n$	numeral ($_{1,2}$, . . .)

Operators

$\cdot''$	spatial variations
$\cdot'$	turbulent fluctuations
$\langle\cdot\rangle$	horizontal spatial average
$\langle\cdot\rangle_c$	comprehensive spatial average
$\bar{\cdot}$	time average

Symbols

α	exponential distribution parameter	-
α_0	MacDonald et al. (1998) parameterization constant	-
α_k	tile albedo parameter (α_c or α_r)	-
$\bar{b}$	mean building width	m
β_0	MacDonald et al. (1998) parameterization constant	-
ΔQ_S	net heat storage flux	W m^{-2}
Δt	timestep	s
Δx_i	spatial grid spacing	m
Δz_k	material thickness (Δz_b, Δz_w, or Δz_r)	m

δ_{ij}	Kronecker delta	-
ϵ	a small length scale	m
ϵ_k	tile emissivity parameter (ϵ_c or ϵ_r)	-
γ	randomness parameter	-
γ_h	height randomness	-
γ_l	layout randomness	-
$\hat{L}$	normalised and re-scaled total width function	-
$\hat{z}$	normalised height coordinate	-
λ	thermal conductivity parameter	W m^{-1} K^{-1}
λ_f	frontal area index	-
λ_g	green space area index	-
λ_p	plan area index	-
$\mathbf{e}_\theta$	unit wind vector for wind angle θ	deg
$\mathbf{e}_{\perp\theta}$	unit wind vector perpendicular to wind angle θ	deg
$\mathbf{x}_i$	point in the Euclidean space ($\mathbf{x}$ or $\mathbf{y}$)	-
$\mathcal{B}$	building	-
$\mathcal{T}$	time span	s
ν	kinematic viscosity	m^2 s^{-1}
Ω	fluid domain	-
$\partial\Omega$	fluid-building interface	-
ϕ	flow variable	various
Φ_h	stability function for heat	-
Φ_m	stability function for momentum	-

Π	modified kinematic pressure	$m^2\ s^{-2}$
Ψ_k	fraction of incoming solar radiation (Ψ_b, or Ψ_w)	-
ρ	density of air	$kg\ m^{-3}$
ρ_0	reference value of air density	$kg\ m^{-3}$
σ_H	building height standard deviation	m
$\sigma_{H,f}$	frontal area weighted building-height deviation	m
$\sigma_{H,p}$	plan area weighted building-height deviation	m
τ	kinematic shear stress/momentum flux	$m^2\ s^{-2}$
τ_0	kinematic surface stress/total canopy drag	$m^2\ s^{-2}$
τ_D	kinematic cumulative drag	$m^2\ s^{-2}$
τ_F	kinematic cumulative pressure	$m^2\ s^{-2}$
τ_{ij}^s	subgrid-scale stress tensor	$m^2\ s^{-2}$
Θ	potential temperature	K
θ	wind direction angle	deg
Θ_0	reference value of potential temperature	K
$\tilde{\alpha}$	empirically fitted distribution parameter	-
$\tilde{p}$	atmospheric pressure	Pa
$\tilde{r}$	representative building-height ratio parameter	-
Υ_k	exchange-diffuse radiation density (Υ_b, or Υ_w)	-
ζ	normalised frontal area	-
a_0	Kanda et al. (2013) parameterization constant	-
a_1	Kanda et al. (2013) parameterization constant	-
A_a	fluid area	m^2

A_F	total frontal area of buildings	m^2
A_f	frontal area of a single building	m^2
A_P	total plan area of buildings	m^2
A_p	plan area of a single building	m^2
A_T	unit plan area	m^2
B	building cross-section	-
b	building width	m
b_0	Kanda et al. (2013) parameterization constant	-
b_1	Kanda et al. (2013) parameterization constant	-
B_h	height of a cuboid-shaped building	m
B_l	length of a cuboid-shaped building	m
B_w	width of a cuboid-shaped building	m
c_0	Kanda et al. (2013) parameterization constant	-
c_1	Kanda et al. (2013) parameterization constant	-
C_D	MacDonald et al. (1998) parameterization constant	-
c_D	drag coefficient	-
c_f	friction factor	-
C_H	heat-exchange coefficient	-
C_k	tile areal heat capacity (C_c or C_r)	J K^{-1} m^{-2}
c_k	volumetric material heat capacity (c_b, c_w, or c_r)	J K^{-1} m^{-3}
C_M	momentum-exchange coefficient	-
C_n	polynomial coefficient (C_1 or C_2)	-
c_n	fitting coefficient (c_0, c_1, ...)	various

c_p	specific heat capacity of air	J kg^{-1} K^{-1}
$C_{\max}$	maximum CFL number	-
D	infinite street-canyon length	m
d	street-canyon length	m
$d_{\max}$	maximum diffusion number	-
e^s	subgrid-scale turbulent kinetic energy	m^2 s^{-2}
F	large-scale kinematic forcing	m s^{-2}
F_D	total drag force	N
f_D	volumetric drag force	m s^{-2}
f_H	stability correction	-
F_U	urban land-cover fraction	-
g_n	grid-box weighting (g_1, g_2, ...)	-
H	street-canyon height	m
h	top of the urban boundary layer	m
H/W	canyon aspect ratio	-
K^*	net shortwave-radiation flux	W m^{-2}
$K^{\downarrow}$	incoming solar radiation density	W m^{-2}
K_m	eddy viscosity	m^2 s^{-1}
L	total mean building-width function	m
l	perimeter	m
L^*	net longwave-radiation flux	W m^{-2}
$L^{\downarrow}$	downward longwave-radiation density	W m^{-2}
N	number of buildings	-

n_i	normal vector component (n_x, n_y or n_z)	-
P	a fixed kinematic pressure	$m^2\ s^{-2}$
p	kinematic pressure	$m^2\ s^{-2}$
Q	projection matrix	-
Q^*	net radiation flux	$W\ m^{-2}$
Q_E	surface latent heat flux	$W\ m^{-2}$
Q_F	anthropogenic heat flux	$W\ m^{-2}$
Q_G	ground heat flux	$W\ m^{-2}$
Q_H	surface sensible heat flux	$W\ m^{-2}$
R	street-canyon total width (street and building)	m
r	maximum to mean building-height ratio	-
$r_{bulk,k}$	tile bulk resistance ($r_{bulk,c}$ or $r_{bulk,r}$)	-
S	Normalised height-profile of a building	-
s	third-order polynomial	-
T	atmospheric temperature	K
t	time coordinate	s
T_k	tile-surface temperature (T_c or T_r)	K
T_s	soil temperature	K
U	wind speed	$m\ s^{-1}$
u_i	velocity component (u, v, or w)	$m\ s^{-1}$
u_*	friction velocity	$m\ s^{-1}$
U_{CT}	wind speed at the top of the street canyon	$m\ s^{-1}$
V	set of vertices	-

V_a	a volume of air	m^3
W	street-canyon width	m
W/R	repeating ratio	-
w_n	weight (w_1, w_2, ...)	-
X	Kanda et al. (2013) parameterization parameter	-
x_i	spatial coordinate in Euclidean space (x, y or z)	m
Y	Kanda et al. (2013) parameterization parameter	-
z'	alternative height coordinate	m
z_0	roughness length	m
z_1	height of the lowest atmospheric model level	m
z_d	displacement height	m
z_H	mean building height	m
z_m	building maximum height (OS data)	m
z_p	building principle height (OS data)	m
$z_{0,K}$	Kanda et al. (2013) roughness length	m
$z_{0,MD}$	MacDonald et al. (1998) roughness length	m
z_{0h}	roughness length for heat	m
$z_{\max}$	maximum building height	m
$z_{d,K}$	Kanda et al. (2013) displacement height	m
$z_{d,MD}$	MacDonald et al. (1998) displacement height	m
$z_{H,f}$	frontal area weighted mean building height	m
$z_{H,p}$	plan area weighted mean building height	m
z_{ML}	height of the mixed-layer	m

1

Introduction

Within the next ten years the global urban population will grow by another billion; London alongside other metropolitan areas worldwide will become a megacity with a population exceeding 10 million, according to current predictions from the United Nations' *World Urbanization Prospects* (United Nations 2019). The majority of the world's population already lives in urban agglomerations. The concentration of people, built-up infrastructure and economic activities increases the vulnerability to extreme weather events, resource scarcity and air pollution (Oke et al. 2017). Climate change over-proportionally affects urbanised areas (Hoegh-Guldberg et al. 2018) and adaptation to more extreme conditions poses an enormous challenge to urban regions around the world.

The urban climate itself is complex and shaped by many different processes. One of the intrinsic challenges of understanding urban climates arises from the heterogeneity of urban areas within and across a range of scales (Barlow et al. 2017). Urban elements include buildings of various size and shape, paved surfaces, trees, green spaces, and water (cf. Figure 1.1). Building facades and street surfaces are made of various materials with distinct properties, and the roads form a complex network. These elements interact in a non-trivial way with each other and the atmosphere above. Cities consist of neighbourhoods with very different characteristics: dense commercial centres, residential neighbourhoods, industrial zones, suburban areas or

Figure 1.1: An example of the complexity of urban environments. The interplay of many different urban elements and processes shapes the urban climate. ©User:Colin/Wikimedia Commons

parks. Together all of these elements and processes influence wind, temperature, and humidity in and above urban regions.

Understanding the complex interactions of urban climates is essential for the representation of cities in weather and climate models. Accurate urban models are necessary to improve weather forecasts and services in the most populated areas in the world. Better warnings of severe weather hazards like heat waves, flooding, and poor air quality protect millions and can greatly reduce economic impacts. Moreover, urban climate models are crucial for planning how to adapt cities for more extreme weather, and how to transform them to be more sustainable and resilient in a changing climate. To contribute to the improvement of urban models, this thesis investigates effects of heterogeneous building forms and their representation in numerical weather prediction models.

1.1 Urban climate

Most of the weather takes place in the troposphere, the lowest part of the atmosphere. Within the troposphere in the region closest to the ground, the atmosphere is directly influenced by its lower boundary, the Earth's surface.

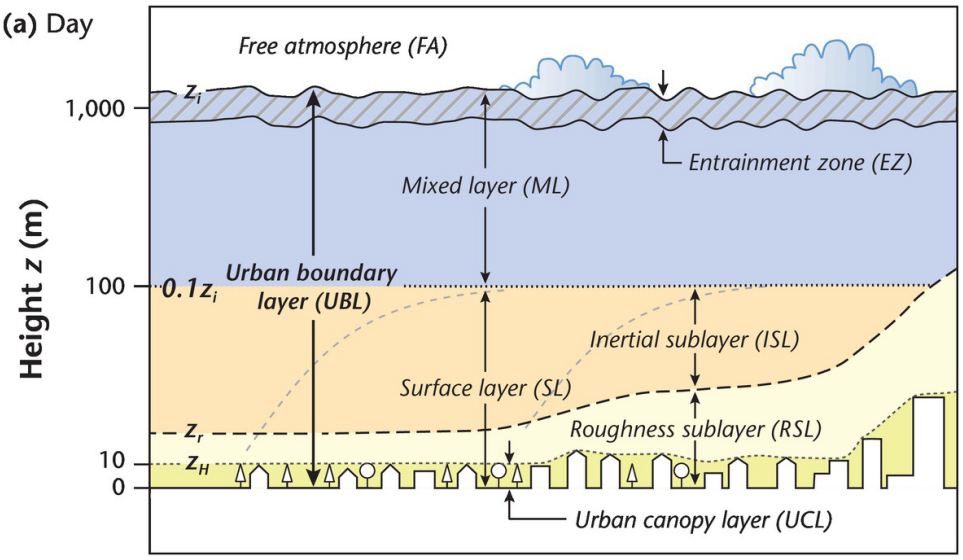

Figure 1.2: The urban boundary layer by day (Oke et al. 2017, reproduced with permission of Cambridge University Press through PLSclear). Note that the height scale is logarithmic, except near the surface.

This region of surface influence is called the atmospheric boundary layer (ABL). The atmosphere responds to surface forcings which include friction, evapotranspiration, heat transfer, pollutant emission and flow modification by terrain and obstacles (Stull 1988). The surface forcings generate turbulence, which acts as an important vertical transport process, redistributing momentum, heat, moisture, and pollutants, and therefore substantially contributing to the local weather. The remainder of the troposphere above the atmospheric boundary layer is called the free atmosphere, where the direct influence of the Earth's surface is insignificant and large-scale flow patterns determine the weather.

When urban environments are at the interface between the land and the atmosphere we speak of the urban surface, and the ABL becomes the urban boundary layer (UBL), illustrated in Figure 1.2 (Oke et al. 2017). The built-up system of a city lies within the urban canopy layer (UCL), which extends from the ground to the height of the main urban elements such as buildings or trees. The heterogeneity of this space and the complexity of its processes, including most of human activities, are what shapes the urban climate (Oke et al. 2017). From the ground up to several times

the height of the urban elements is the roughness sublayer (RSL). Inside the RSL the airflow is strongly affected by the individual urban elements and varies with spatial position. The air is forced to flow around these obstacles, which can result in regions with substantial uplift or downdraft of air. Above the roughness sublayer is the inertial sublayer (ISL), where the influence of individual elements decreases. Although some large-scale uplifts or downdrafts may be present, mean airflow is generally independent of horizontal spatial position and only depends on height above ground. A mixed layer (ML), where effects of the urban area on atmospheric properties are uniformly mixed, describes the region between the surface layer (UCL, RSL, and ISL) and the free atmosphere.

1.2 Urban heterogeneity

Surface processes on various length scales within the urban boundary layer control the exchange of energy, mass, and momentum (Oke et al. 2017). On the length scale of metres, urban elements such as the buildings and trees form units of street canyons and building blocks (Figure 1.3). The street-canyon geometry and the presence of vegetation influence absorption and reflection of solar radiation. The various materials of the urban elements have different capacities to store heat, streets and green space have a specific permeability and capacity to store water. These units create their own microclimate, affecting thermal comfort and local air quality (Best and Grimmond 2015).

On the scale of urban neighbourhoods (of order 100–1000 m, Barlow 2014), the different forms and densities of buildings change the airflow, and therefore affect the transport of momentum, heat, and air-pollution particles in urban areas. The effects of spatial heterogeneity extend to the scale of the entire city, where the neighbourhoods with their distinct flow characteristics lead to a horizontally heterogeneous flow across the urban environment. The change in surface properties between the different neighbourhoods can generate local internal boundary layers within the UBL, which grow vertically in the downstream direction and blend further with increasing height to a horizontally homogeneous flow, containing cumulative effects from the whole urban region (Barlow 2014).

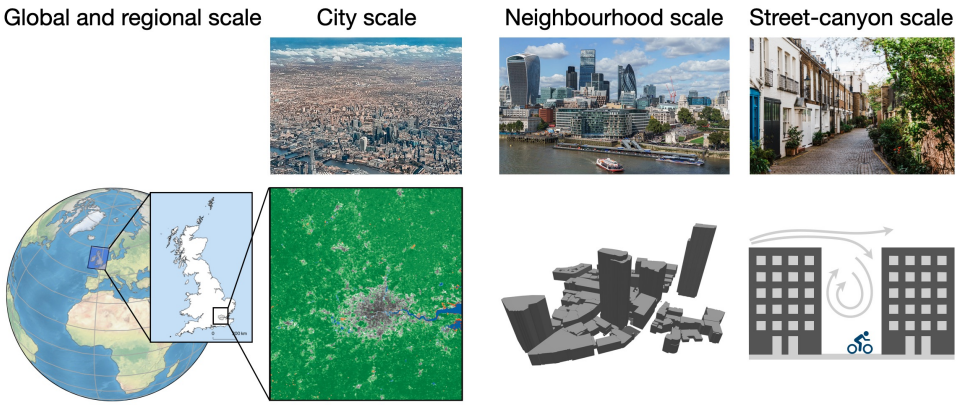

Figure 1.3: Heterogeneous urban environments and corresponding models at multiple scales. ©Top f.l.t.r.: GillyBerlin/Wikimedia Commons, User:Colin/Wikimedia Commons, Bruno Martins/Unsplash, bottom left: data from OS OpenData (Ordnance Survey (GB) 2005), second left: data from Met Office (Boutle et al. 2016), second right: data from OS MasterMap (Ordnance Survey (GB) 2019a).

1.3 Urban parameterizations in numerical weather prediction

In numerical weather prediction (NWP) and climate models, surface processes cannot be explicitly resolved and their impacts on the atmosphere therefore need to be parameterised by a simplified process. Global-scale NWP models are computed with a horizontal resolution of the order of tens of kilometres, with regional models embedded on a finer scale of several kilometres (Figure 1.3). The influence of the urban surface extends to several kilometres for a larger urban region, and many regional models therefore have parameterizations for urban areas included. Specialised regional models on the city scale even use a horizontal resolution of several hundred metres (e.g. Boutle et al. 2016), where model grid boxes contain heterogeneous neighbourhoods: one grid box may represent a cluster of high-rise buildings, and the next one may represent a park.

The vertical resolution of weather and climate models is very different from the horizontal resolution, and is typically a few to tens of metres next to the surface, and increases gradually with height to a few hundred metres in the mid-troposphere (e.g. Walters et al. 2019). Buildings therefore pro-

trude from the ground into several of the lowest vertical atmospheric model levels. However, since buildings are not explicitly resolved but being modelled as part of an urban surface, they are often described to be 'buried in the ground'.

Different processes that contribute to the relative warming of urban environments compared to their rural surroundings are parameterised by urban surface energy balance models (Grimmond et al. 2010), which are usually based on simple representations of urban areas as two-dimensional street canyons (cf. Figure 1.3). Urban energy balance models are widely used to describe interactions between the land-surface (i.e., the urban environment) and the atmosphere within NWP models. Examples of such coupled urban land-surface systems are the Town Energy Budget (TEB; Masson 2000) and MORUSES (Porson et al. 2010a,b) as part of the UK Met Office land-surface model JULES (Best et al. 2011; Clark et al. 2011).

Building form is an important aspect for parameterising aerodynamic effects, and urban areas within weather prediction models are therefore typically described by morphological parameters such the buildings' plan area index λ_p, a wind-facing frontal area index of buildings λ_f, and an average building height z_H. Many parameterizations for airflow above cities are based on these and similar surface-cover parameters (Raupach 1994; MacDonald et al. 1998; Millward-Hopkins et al. 2012; Kanda et al. 2013).

For simplified, cuboid-shaped buildings, these three morphological parameters are defined as follows. An arbitrary domain with plan area A_T has N buildings $\mathcal{B}_n$, where $n = 1, \ldots, N$, with building width $B_{w,n}$, length $B_{l,n}$, and height $B_{h,n}$. The plan area of a building is $A_{p,n} = B_{w,n}B_{l,n}$ and its frontal area is $A_{f,n} = B_{w,n}B_{h,n}$, which is the building's wind-facing area, implying that the wind direction is perpendicular to $B_{w,n}$. The plan area index (often called building density) λ_p (Figure 1.4a) is the buildings' total plan area A_P per unit plan area,

$$\lambda_p = \frac{A_P}{A_T} = \frac{\sum_n A_{p,n}}{A_T}. \tag{1.1}$$

The frontal area index λ_f (Figure 1.4b) is the total frontal area A_F per unit plan area,

$$\lambda_f = \frac{A_F}{A_T} = \frac{\sum_n A_{f,n}}{A_T}, \tag{1.2}$$

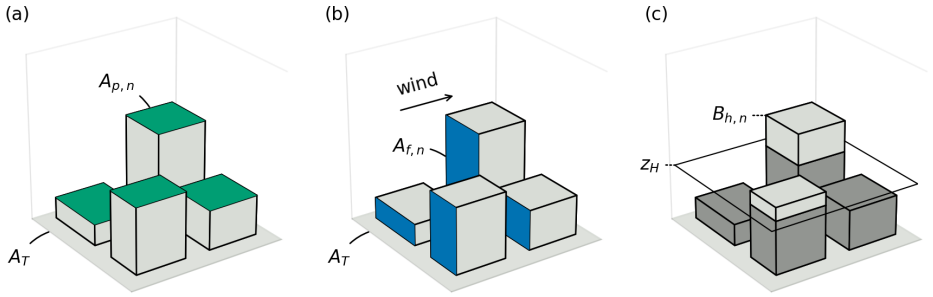

Figure 1.4: Illustration of the urban morphology parameters (a) plan area index λ_p, (b) frontal area index λ_f, and (c) mean building height z_H.

and the mean building height z_H (Figure 1.4c) is

$$z_H = \sum_n w_k B_{h,n} \tag{1.3}$$

with weights w_n such that

$$\sum_n w_n = 1, \tag{1.4}$$

which may be defined as an ordinary mean (with equal weights $w_n = 1/N$) or, for example, as a frontal area weighted average, where $w_n = A_{f,n}/A_F$ (Grimmond and Oke 1999).

1.4 Airflow studies in urban neighbourhoods

Models that parameterise the aerodynamic effects of urban areas are developed from urban studies on the neighbourhood scale, which investigate the airflow around and above buildings. Buildings exert a drag force onto the airflow, which decreases the velocity and deflects the flow. Most studies on the neighbourhood scale adopt one of two approaches (cf. Figure 1.5): 1) a bottom-up approach, which starts at idealised building geometries and gradually adds complexity; 2) a top-down approach, in which real or realistic urban morphologies are considered.

Idealised morphologies consist of simplified buildings, which are all of identical (uniform) or similar shape. Studies pursuing the bottom-up approach have a particular strength in forming an understanding of the fundamental processes governing these flows, and have brought insight on the

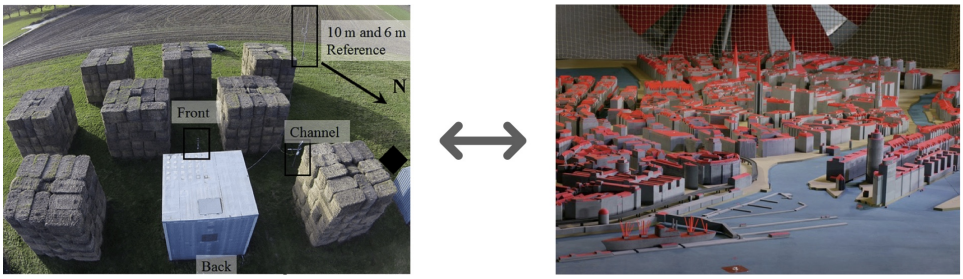

Figure 1.5: Complexity gap in urban studies between simple, idealised, and universal flows (left, Gough et al. 2019), and complex, realistic, and case-specific flows (right, Hertwig 2013, with permission).

effects of building cover, building alignment, and wind angle (Coceal et al. 2006; Kanda 2006; Neophytou et al. 2014; Cheng and Porté-Agel 2015; Castro et al. 2017). Case studies pursuing the top-down approach have complex building geometries and realistic building alignments; they create specific insights for that particular morphology. They show the complexity and rich variety of flow features at a specific location, and highlight the spatial variability of the flow field over urban sites (Carpentieri et al. 2009; Giometto et al. 2016; Hertwig et al. 2019).

Studies on simple morphologies often form the basis of models that describe the urban drag force or wind-velocity profiles over urban areas, and much progress has been made on the representation of impacts of idealised buildings. However, concepts based on idealised geometries may not match well realistic urban environments, and the effects of heterogeneity in urban morphologies – differently sized and shaped buildings – are not well understood (Barlow et al. 2017). There is a need to improve our fundamental understanding of the effect of heterogeneity on flow in urban morphologies of intermediate complexity. Realistic heterogeneity needs to be introduced without adding too many new degrees of freedom to the parameter space, such that fundamental studies remain tractable. This thesis studies urban airflow of idealised, heterogeneous environments with a particular focus on investigating subgrid heterogeneity of NWP models, by studying the variety of neighbourhood-scale flows that are represented by the same parameters in urban land-surface models.

1.5 Numerical modelling of urban airflow

Numerical models that are suitable for the study of urban airflow and related processes are models that resolve the three-dimensional flow within and above buildings, and recent developments in computing have made a variety of scientific modelling tools available and feasible to use in urban climate studies. On the smallest length scales this is done by direct numerical simulations (DNS; e.g., Coceal et al. 2006), which solve the governing Navier–Stokes equations up to very fine scales, but are computationally very expensive and thus limited in their range. A number of models exist on length scales of local neighbourhoods. The majority of them are based on the Reynolds-averaged Navier–Stokes equations (RANS), which simulate the mean flow and parameterise all turbulent fluctuations. Examples of such models are ENVI-met (Simon 2016), MITRAS (Salim et al. 2017) and MUKLIMO_3 (Sievers 2016). Large-eddy simulations (LES) resolve instantaneous airflow for the majority of the energy-containing scales of the turbulence, only parameterising the smallest eddies.

LES models are currently the only type of models that are able to capture much of the turbulence and other important features of the flow, but are still feasible to run with an ensemble of configurations and parameters. Examples of LES models for the urban environment are PALM-4U (Resler et al. 2017; Maronga et al. 2020), OpenFOAM (e.g. Castro et al. 2017) and the Dutch Atmospheric Large-Eddy Simulation model (DALES; Heus et al. 2010), which has recently been extended for the urban environment (uDALES; Tomas et al. 2016; Suter 2018; Grylls et al. 2019). The uDALES model is used in this thesis.

1.6 Scope of this work

This thesis investigates the aerodynamic effects of heterogeneous building forms from neighbourhood to city scale. The aim is to develop a model for aerodynamic drag of buildings that better represents the heterogeneity of urban environments in numerical weather prediction models. The thesis initially focuses on improving our understanding of airflow in heterogeneous neighbourhoods. A large-eddy simulation study of idealised heterogeneous

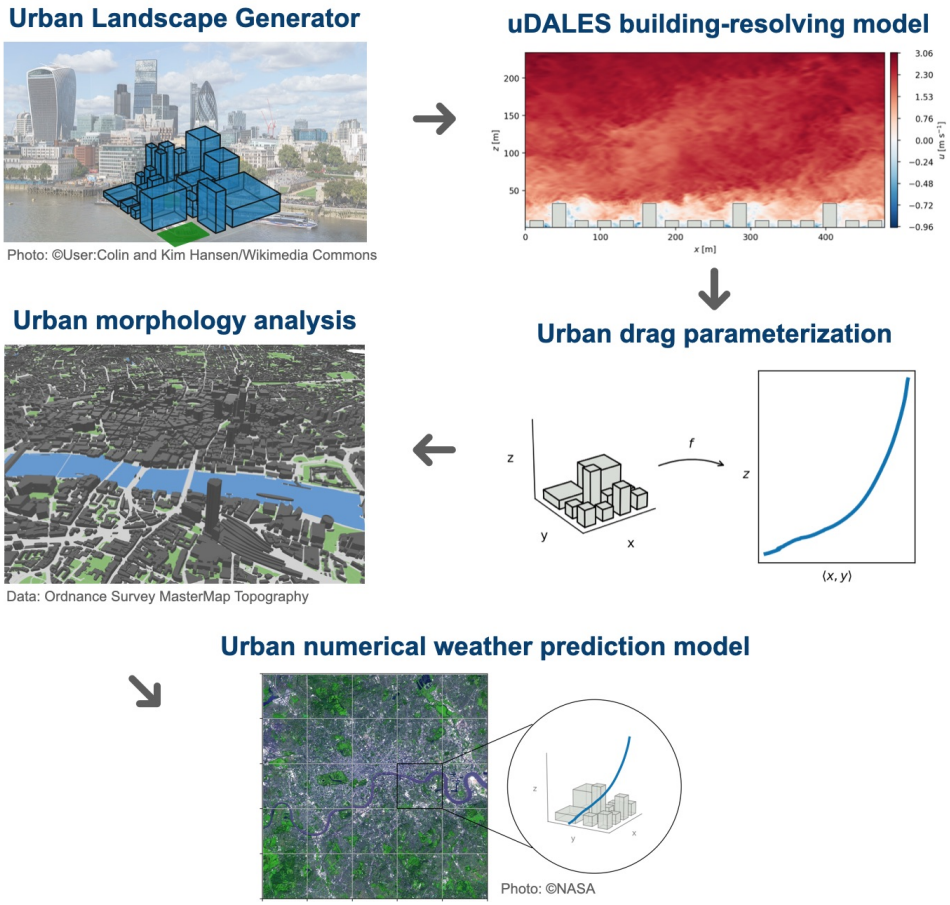

Figure 1.6: Schematic outline of the thesis objectives.

urban morphologies is conducted to explore flow structure and turbulent transport in different neighbourhoods. Based on this analysis, a height-distributed model for urban drag in developed. Thereafter, this knowledge is applied to the entire urban landscape, by implementing the distributed urban model into a high-resolution numerical weather prediction model over the Greater London area and surroundings. A case study is carried out that evaluates the new urban drag model in comparison to the standard urban parameterization. Figure 1.6 provides a schematic outline of the thesis' objectives, which are:

1. to develop a tool that generates idealised heterogeneous urban environments with prescribed plan area index and frontal area index,

2. to conduct large-eddy simulations of urban morphologies with identical

plan area index and frontal area index, and investigate the effects of heterogeneity on urban airflow,

3. to develop a parameterization model for urban drag on the neighbourhood scale,

4. to analyse the urban morphology of Greater London and extract building information as input data for the drag model,

5. to conduct a case study with the Met Office London Model to evaluate the differences between the standard urban parameterization and the new distributed drag model.

1.7 Thesis outline

The thesis is structured as follows.

Chapter 2 This chapter reviews the aerodynamic effects of urban environments. Starting with a discussion of the governing equations of urban flow, we derive a momentum-budget equation over spatially heterogeneous terrain. Assumptions on the flow forcing lead to a description of urban canopy drag, which is used throughout this thesis. In this process, the concepts of spatial- and temporal-averaging over obstacle-containing domains, steady-state flows, momentum fluxes and their decomposition into turbulent, dispersive, and viscous parts, cumulative stress functions, and total urban canopy drag are introduced.

Chapter 3 This chapter describes the large-eddy simulation model uDALES used for the building-resolving, neighbourhood-scale simulations. The development of the Urban Landscape Generator is documented, which is the tool to generate idealised and heterogeneous urban morphologies. Nine morphologies with equal plan- and frontal-area indices, but different configurations of building heights, plan areas, and street layout are generated with the Urban Landscape Generator and simulated using uDALES.

Chapter 4 This chapter presents the analysis of the neighbourhood-scale simulations. Effects on mean-flow structure and vertical momentum trans-

port are explored. Aerodynamic roughness parameters for logarithmic wind profiles are estimated, compared with values from standard parameterizations, and correlated to an extended range of building statistics. A normalised frontal area function and the LES data are used to derive a parameterization that describes the vertical distribution of drag inside the urban canopy.

Chapter 5 This chapter analyses the urban morphology of Greater London and surroundings, and performs preceding steps that are required for incorporating the distributed drag model into a high-resolution configuration of the Met Office weather forecasting model. First, a generalised description of the frontal area function is introduced, which has the objective to characterise vertical morphology profiles. These vertical profiles and other morphology parameters of Greater London and surrounding areas are subsequently calculated. Then, to simplify the required input data for the NWP model, a parameterization of the morphology profiles of Greater London is derived.

Chapter 6 This chapter provides a short review on urban parameterizations in numerical weather prediction, using the Met Office models as an example. An experimental set-up to improve the Met Office land-surface model JULES is presented, which aims to incorporate a standard drag parameterization for heterogeneous morphologies. Shortcomings of this modelling approach and potential further developments are discussed afterwards.

Chapter 7 This chapter describes the process of incorporating the distributed drag model into the Met Office London Model. Modifications to the current urban surface scheme are outlined, such that the distributed drag can be added to the momentum equations as an additional stress term. A case study is conducted for model comparison between the standard model set-up and the model including the distributed drag scheme.

Chapter 8 The concluding chapter summarises main results and discusses implications for the general development of distributed urban canopy models. It also outlines possible directions for future work.

Appendices The Appendices A–D provide supplementary information that is referred to in the relevant chapters.

1.8 Publications and novel contributions

The theoretical background in Chapter 2 is based on an established framework in the literature, which was expanded with detailed derivations. The work with the large-eddy simulation model uDALES, introduced in Chapter 3, was primarily to design and conduct simulations, with occasional code developments and improvements. The Urban Landscape Generator from Chapter 3 was developed for this study and is published on github: https://github.com/bss116/citygenerator (Sützl and van Reeuwijk 2020). The content of Chapter 4 is based on material from *'Drag distribution in idealized heterogeneous urban environments'* (Sützl, Rooney and van Reeuwijk 2021b). Parts of Chapter 2 and Chapter 3 are also based on this publication. The algorithms and data calculations presented in Chapter 5 were developed for this study. Chapter 6 combines a review of the literature with experimental changes to the model JULES, which were carried out during a summer placement at the Met Office. During this placement a prototype for the urban drag scheme was developed together with Gabriel Rooney. Gabriel Rooney implemented the final version of the drag parameterization and ran the simulations of the London Model at the Met Office, which were required for the subsequent analysis of the model outputs in Chapter 7. Parts of Chapters 5 and 7 will be combined to: *'Distributed urban drag parameterization for sub-kilometre scale numerical weather prediction'* (Sützl, Rooney, Finnenkoetter, Bohnenstengel, Grimmond and van Reeuwijk 2021a), a manuscript in preparation for submission to the Quarterly Journal of the Royal Meteorological Society.

2

Quantifying drag in urban environments

Urban settlements modify the wind by forcing it to flow around and over buildings, thus generating complicated flow structures in the wake of the buildings and producing turbulent motion around them (Belcher 2005; Oke et al. 2017). Below we review how buildings affect the mixing and vertical transport processes throughout and above the urban canopy. A momentum-budget equation may be derived by integrating the governing flow equations over the horizontal (x and y) directions, which describes the balance of horizontally averaged forces acting on the fluid, such as a large-scale pressure gradient accelerating the flow, and a drag force by the building obstacles opposing it.

Section 2.1 defines averages and decomposition of flow variables. Section 2.2 introduces the governing flow equations and derives the averaged momentum-budget equation. In Section 2.3 the individual terms of the resulting balance of forces are discussed in detail. Section 2.4 introduces the commonly used kinematic (cumulative) stress functions.

2.1 Averages and decomposition

The horizontal spatial average of a flow quantity $\phi(t, x, y, z)$ over the fluid area in the x–y-plane, denoted by Ω, is defined by

$$\langle \phi \rangle(t, z) = \frac{1}{A_a(z)} \int_\Omega \phi(t, x, y, z)\, \mathrm{d}A, \tag{2.1}$$

where $A_a(z) = \int_\Omega \mathrm{d}A$ is the fluid area at height z. For a statistically steady-state process, the Reynolds average can be obtained by taking a time average of $\phi(t, x, y, z)$ over a time span $\mathcal{T}$ longer than the typical flow-fluctuation time scale; the average is defined as

$$\overline{\phi}(x, y, z) = \frac{1}{\mathcal{T}} \int_0^{\mathcal{T}} \phi(t, x, y, z)\, \mathrm{d}t. \tag{2.2}$$

A framework for studying flow over spatially heterogeneous surfaces has been established for vegetated canopies (e.g. Raupach and Shaw 1982; Finnigan 2000; Nepf 2012), where flow variables are decomposed to isolate the effects of spatial inhomogeneity by means of a triple decomposition

$$\phi(t, x, y, z) = \langle \overline{\phi} \rangle(z) + \overline{\phi}''(x, y, z) + \phi'(t, x, y, z), \tag{2.3}$$

where $\langle \dot{} \rangle$ is a space-time mean, $\dot{}''$ represents spatial variations of the time mean, and $\dot{}'$ represents the turbulent fluctuations. This decomposition is an extension of classical Reynolds averaging, since $\overline{\phi} = \langle \overline{\phi} \rangle + \overline{\phi}''$, where $\overline{\phi}$ is the Reynolds average. Figure 2.1 illustrates the triple decomposition of the streamwise velocity component for flow in an urban environment.

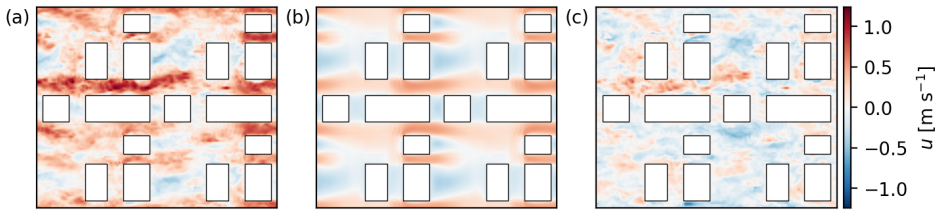

Figure 2.1: Triple decomposition of streamwise velocity u at a fixed height z. (a) the instantaneous flow field $u(t, x, y)$, (b) spatial variations of the time mean $\overline{u}''(x, y)$, and (c) turbulent fluctuations $u'(t, x, y)$. The space-time mean is $\langle \overline{u} \rangle = 0.2$ m s^{-1}. Data from simulation S7 (see Section 3.4).

2.2 Momentum-budget equation over heterogeneous surfaces

In the following derivations we highlight the governing equations to provide a better overview: the momentum equation is marked in blue, the mass continuity equation in orange.

2.2.1 Governing equations

The airflow in and above cities is described by the incompressible Navier–Stokes equations

$$\frac{\partial u_i}{\partial t} + u_j \frac{\partial u_i}{\partial x_j} = -\frac{1}{\rho_0}\frac{\partial \tilde{p}}{\partial x_i} + \nu \frac{\partial^2 u_i}{\partial x_j^2} - \frac{\rho}{\rho_0} g \delta_{i3} \tag{2.4}$$

$$\frac{\partial u_i}{\partial x_i} = 0, \tag{2.5}$$

where the Einstein summation notation has been used. In the equation above, u_i represents the velocity in the i-direction, $\tilde{p}$ the pressure, which varies with height due to hydrostatic effects and also varies in in the horizontal due to large-scale forcings, ρ is the density of air, where ρ_0 is a constant density, ν is the kinematic viscosity, g is the standard acceleration due to gravity and δ_{ij} is the Kronecker delta. We define the kinematic pressure deviation p from these forces, which can be formalised by:

$$\tilde{p} = \rho_0 p - \rho_0 F_x x - \rho_0 F_y y - \rho_0 g z, \tag{2.6}$$

where large-scale kinematic pressure forcings in the x and y directions are denoted by F_x and F_y. We will assume a constant pressure-gradient forcing

$$F_i = -\frac{1}{\rho_0}\frac{\partial P}{\partial x_i} = \text{constant} > 0 \tag{2.7}$$

for the x and y directions.

Substitution into (2.4) results in

$$\frac{\partial u_i}{\partial t} + u_j \frac{\partial u_i}{\partial x_j} = -\frac{\partial p}{\partial x_i} + \nu \frac{\partial^2 u_i}{\partial x_j^2} + \frac{(\rho_0 - \rho)}{\rho_0} g \delta_{i3} + F_i. \tag{2.8}$$

For an ideal gas, $(\rho_0 - \rho)/\rho_0 = \Theta/\Theta_0$, which yields an expression for the vertical buoyancy force in terms of potential temperature Θ with reference value Θ_0. However, in the following derivation we will assume a constant density fluid ($\rho = \rho_0$), in which case the gravitational term has no dynamic effect and there is no buoyancy force.

Using (2.5), the advective terms can be written as:

$$u_j \frac{\partial u_i}{\partial x_j} = u_j \frac{\partial u_i}{\partial x_j} + u_i \frac{\partial u_j}{\partial x_j} = \frac{\partial}{\partial x_j}\left(u_j u_i\right), \tag{2.9}$$

and substituting in (2.8) then results in

$$\boxed{\frac{\partial u_i}{\partial t} + \frac{\partial u_j u_i}{\partial x_j} = -\frac{\partial p}{\partial x_i} + \nu \frac{\partial^2 u_i}{\partial x_j^2} + F_i.} \tag{2.10}$$

2.2.2 Momentum budget

Time-averaging and spatial integration of (2.10) and (2.5) over the x–y-planes Ω yields

$$\boxed{\int_\Omega \overline{\frac{\partial u_i}{\partial t}}\,\mathrm{d}A + \int_\Omega \overline{\frac{\partial u_j u_i}{\partial x_j}}\,\mathrm{d}A = -\int_\Omega \overline{\frac{\partial p}{\partial x_i}}\,\mathrm{d}A + \int_\Omega \nu \overline{\frac{\partial^2 u_i}{\partial x_j^2}}\,\mathrm{d}A + \int_\Omega \overline{F_i}\,\mathrm{d}A,} \tag{2.11}$$

and

$$\boxed{\int_\Omega \overline{\frac{\partial u_i}{\partial x_i}}\,\mathrm{d}A = 0.} \tag{2.12}$$

Note that the order of time-averaging and spatial integration is interchangeable, since the region for spatial integration is constant in time (cf. Schmid et al. 2019). For the same reason we can commute time-averaging and spatial differentiation. Spatial integration and differentiation can be interchanged by means of the spatial averaging theorem, which was derived to describe flow in porous media (cf. Whitaker 1985):

$$\int_\Omega \frac{\partial \phi}{\partial x_i}\,\mathrm{d}A = \left(\frac{\mathrm{d}}{\mathrm{d}z}\int_\Omega \phi\,\mathrm{d}A\right)\delta_{i3} - \oint_{\partial\Omega} \phi n_i\,\mathrm{d}l. \tag{2.13}$$

Since we integrate over the full x–y plane Ω, the area integral (first term on the right hand side) has no dependency on x and y and therefore the spatial derivatives in the x- and y-directions are zero. The line integral (second

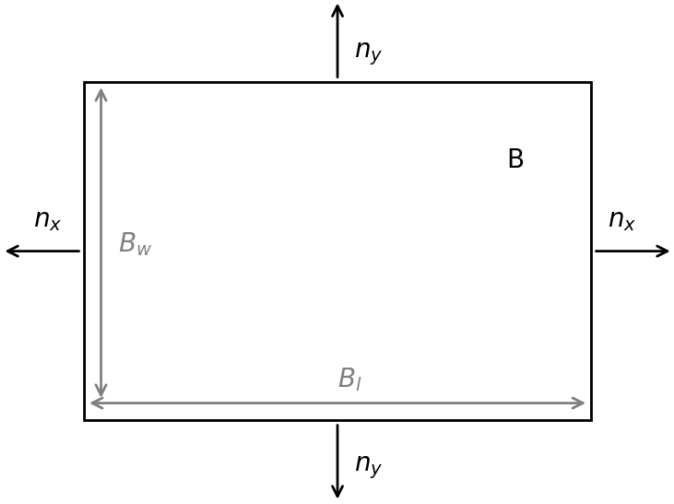

Figure 2.2: The two-dimensional normal vector components n_x and n_y at the interface between the fluid domain and a building cross-section B.

term on r.h.s.) is defined along the interface of the fluid domain with the buildings, $\partial\Omega$, with the surface normal in the x–y plane, n_i, pointing into the fluid region. Figure 2.2 sketches the interface between the fluid domain and a single building. Note that we assume n_i to be a two-dimensional vector, using the simplifying assumption that the buildings have no slanted surfaces, and that $n_z = 0$. A representation that accounts for building surfaces at any orientation requires volume-averaging over a thin slab of air, and the definition of a three-dimensional normal vector (cf. van Reeuwijk et al. 2021).

Applying Equation 2.13 to the integral continuity equation (2.12) yields

$$\int_\Omega \overline{\frac{\partial u_i}{\partial x_i}}\,\mathrm{d}A = \frac{\mathrm{d}}{\mathrm{d}z}\int_\Omega \overline{w}\,\mathrm{d}A - \oint_{\partial\Omega} \overline{u_i}\overline{n_i}\,\mathrm{d}l = \frac{\mathrm{d}}{\mathrm{d}z}\int_\Omega \overline{w}\,\mathrm{d}A = 0, \tag{2.14}$$

where the line integral equals zero, because there is no flow across the boundary (the buildings are considered impermeable) and therefore the normal velocity at the interface is zero. For the terms with spatial derivatives in (2.11) we obtain

$$\int_\Omega \frac{\partial u_j u_i}{\partial x_j}\,\mathrm{d}A = \frac{\mathrm{d}}{\mathrm{d}z}\int_\Omega w u_i\,\mathrm{d}A, \tag{2.15}$$

the viscous term is

$$\int_\Omega \nu \frac{\partial^2 u_i}{\partial x_j^2}\,\mathrm{d}A = \frac{\mathrm{d}}{\mathrm{d}z}\int_\Omega \nu \frac{\partial u_i}{\partial z}\,\mathrm{d}A - \oint_{\partial\Omega} \nu \frac{\partial u_i}{\partial x_j} n_j\,\mathrm{d}l, \tag{2.16}$$

where $\partial u_i n_j/\partial x_j$ is a directional derivative of the velocity in the orthogonal direction of the surface, and the pressure term reads:

$$\int_\Omega \frac{\partial p}{\partial x_i}\,\mathrm{d}A = \frac{\mathrm{d}}{\mathrm{d}z}\int_\Omega p\,\mathrm{d}A\delta_{i3} - \oint_{\partial\Omega} p n_i\,\mathrm{d}l. \tag{2.17}$$

Because p is the deviatoric pressure in a neutral atmosphere, $\overline{\int_\Omega p\,\mathrm{d}A} = 0$.

Furthermore, with F_i = constant, we obtain

$$\int_\Omega \overline{\frac{\partial u_i}{\partial t}}\,\mathrm{d}A + \frac{\mathrm{d}}{\mathrm{d}z}\int_\Omega \left(\overline{w u_i - \nu\frac{\partial u_i}{\partial z}}\right)\mathrm{d}A = \oint_{\partial\Omega}\left(\overline{p n_i - \nu\frac{\partial u_i}{\partial x_j}n_j}\right)\mathrm{d}l + F_i A_a. \tag{2.18}$$

For simplicity, we assume that the flow is in a statistically steady state, which implies that the z-direction is the only independent variable. Division by the total area of the x–y plane A_T then yields

$$\frac{\mathrm{d}}{\mathrm{d}z}\frac{1}{A_T}\int_\Omega \left(\overline{w u_i - \nu\frac{\partial u_i}{\partial z}}\right)\mathrm{d}A = F_i\frac{A_a}{A_T} - f_{D,i}, \tag{2.19}$$

where

$$f_{D,i} = -\frac{1}{A_T}\oint_{\partial\Omega}\left(\overline{p n_i - \nu\frac{\partial u_i}{\partial x_j}n_j}\right)\mathrm{d}l. \tag{2.20}$$

2.2.3 Flow-variable decomposition

Introducing the spatial-average notation as in (2.1) gives

$$\frac{\mathrm{d}}{\mathrm{d}z}\frac{A_a}{A_T}\left\langle \overline{w u_i - \nu\frac{\partial u_i}{\partial z}}\right\rangle = F_i\frac{A_a}{A_T} - f_{D,i}. \tag{2.21}$$

Triple decomposition of the space-time averaged velocity variables using (2.3) results in (cf. Nikora et al. 2007; Schmid et al. 2019, and derivation in Appendix A)

$$\langle\,\overline{w u_i}\rangle = \langle\overline{w}\rangle\langle\overline{u}_i\rangle + \langle\overline{w}''\overline{u}_i''\rangle + \langle\overline{w' u_i'}\rangle. \tag{2.22}$$

Velocities at solid boundaries are zero (no-slip boundary condition), together with the continuity equation (2.14) (no change in averaged vertical velocity along z) this implies that $\langle\overline{w}\rangle(z) = 0$ everywhere. The first term of the right hand side of (2.22) is therefore zero. With the general averaging properties $\langle\phi''\rangle = 0$ and $\overline{\phi'} = 0$ and application of the spatial averaging theorem, we further obtain:

$$\left\langle \overline{\nu\frac{\partial u_i}{\partial z}} \right\rangle = \left\langle \overline{\nu\frac{\mathrm{d}\langle\overline{u}_i\rangle}{\mathrm{d}z}} \right\rangle + \left\langle \overline{\nu\frac{\partial \overline{u}_i''}{\partial z}} \right\rangle + \left\langle \overline{\nu\frac{\partial u_i'}{\partial z}} \right\rangle = \nu\frac{\mathrm{d}\langle\overline{u}_i\rangle}{\mathrm{d}z}. \tag{2.23}$$

Finally, substituting these terms in (2.21) yields:

$$\boxed{-\frac{\mathrm{d}\tau_i}{\mathrm{d}z} = F_i\frac{A_a}{A_T} - f_{D,i},} \tag{2.24}$$

where

$$\tau_i = -\frac{A_a}{A_T}\left(\langle\overline{w}''\overline{u}_i''\rangle + \langle\overline{w'u_i'}\rangle - \nu\frac{\mathrm{d}\langle\overline{u}_i\rangle}{\mathrm{d}z}\right). \tag{2.25}$$

Since the spatial average is defined as an intrinsic quantity of the flow variable, a correction term of the area ratio of fluid to total plane area $A_a(z)/A_T$ arises in Equation 2.25. Changes in fluid area with height are substantial in urban areas, and therefore this term cannot be neglected. In the following we denote

$$\frac{A_a(z)}{A_T}\langle\cdot\rangle(z) = \langle\cdot\rangle_c(z), \tag{2.26}$$

which is also known as superficial (Nikora et al. 2007) or comprehensive (Xie and Fuka 2018) spatial average. This simplifies the notation to

$$\boxed{-\frac{\mathrm{d}\tau_i}{\mathrm{d}z} = \langle F_i\rangle_c - f_{D,i},} \tag{2.27}$$

with

$$\tau_i = -\langle\overline{w}''\overline{u}_i''\rangle_c - \langle\overline{w'u_i'}\rangle_c + \nu\frac{\mathrm{d}\langle\overline{u}_i\rangle_c}{\mathrm{d}z}. \tag{2.28}$$

2.3 Force balance for streamwise velocity

The sum of all terms in Equation 2.27 is zero, and the equation therefore states the balance of forces. For an illustration of the force balance, the airflow is assumed only in the x-direction with the streamwise velocity component $u_i = u$ and we denote $\langle F_x\rangle_c = F(z)$, $\tau_x(z) = \tau(z)$ and $f_{D,x}(z) = f_D(z)$.

Equation 2.27 then simply reads

$$F(z) + \frac{\mathrm{d}\tau}{\mathrm{d}z}(z) - f_D(z) = 0 \tag{2.29}$$

with

$$F(z) = -\frac{1}{\rho_0}\left\langle \frac{\mathrm{d}P}{\mathrm{d}x} \right\rangle_c (z), \tag{2.30}$$

$$\tau(z) = -\langle \overline{w}''\overline{u}'' \rangle_c(z) - \langle \overline{w'u'} \rangle_c(z) + \nu \frac{\mathrm{d}\langle \overline{u} \rangle_c}{\mathrm{d}z}(z), \tag{2.31}$$

and

$$f_D(z) = -\frac{1}{A_T} \oint_{\partial\Omega} \left(\overline{p} n_x - \nu \left(\frac{\partial \overline{u}}{\partial x} n_x + \frac{\partial \overline{u}}{\partial y} n_y \right) \right) \mathrm{d}l. \tag{2.32}$$

A negative pressure gradient $\mathrm{d}P/\,\mathrm{d}x$ results in acceleration of airflow from higher pressure towards lower pressure, the averaged forcing $F(z)$ is therefore a positive force, thus an acceleration term and a source of momentum.

The gradient of the momentum flux $\frac{\mathrm{d}\tau}{\mathrm{d}z}(z)$ describes the transport of momentum from higher altitudes, where the wind is faster, driven by large-scale flows and undisturbed from the influence of surface elements, down towards the surface, where surface friction and building drag generate resistance and lower velocities. This is a shear force acting throughout the atmosphere with equal acceleration and deceleration, and therefore a momentum transport term. The term $\tau(z)$ represents the averaged total kinematic shear stress (turbulent and viscous), which describes the vertical momentum transfer. It consists of the dispersive flux $\langle \overline{w}''\overline{u}'' \rangle_c(z)$, which represents the vertical transport due to the spatial inhomogeneity in the mean flow, the turbulent momentum flux $\langle \overline{w'u'} \rangle_c(z)$, and the viscous momentum flux $-\nu \frac{\partial \langle \overline{u} \rangle_c}{\partial z}(z)$.

The volumetric aerodynamic drag $f_D(z)$ describes the air resistance of the obstacles. The pressure contributions are a force normal to the obstacles and are referred to as form drag [first integral term in (2.32)]. The frictional force related to molecular diffusion when air is moving parallel to the surface of the obstacles is called skin (or viscous) drag [second and third integral term in (2.32)]. Aerodynamic drag is a force acting opposite the fluid motion, decreasing the velocity and therefore $f_D(z)$ is a deceleration term and a momentum sink.

The implications of an assumption of steady flow are that the time-averaged forces balance and are unchanging over time. The force balance

also provides a quantitative description of the different sublayers in the urban boundary layer (cf. Belcher 2005):

$$\text{ISL:} \qquad \frac{\mathrm{d}}{\mathrm{d}z}\langle\overline{w'u'}\rangle = F \tag{2.33}$$

$$\text{RSL:} \qquad \frac{\mathrm{d}}{\mathrm{d}z}\left(\langle\overline{w'u'}\rangle + \langle\overline{w}''\overline{u}''\rangle\right) = F \tag{2.34}$$

$$\text{UCL:} \qquad \frac{\mathrm{d}}{\mathrm{d}z}\left(\langle\overline{w'u'}\rangle_c + \langle\overline{w}''\overline{u}''\rangle_c\right) = F - f_D \tag{2.35}$$

Note that above the buildings $\langle\cdot\rangle(z) = \langle\cdot\rangle_c(z)$, and that we have ignored viscous terms by assuming high Reynolds number flow. Far above the surface in the inertial sublayer (ISL), the only force acting on the fluid is the constant pressure-gradient force, which is balanced by the constant rate of downward momentum transport, initiated by the surface. Coming closer towards the buildings in the roughness sublayer (RSL), the mean flow becomes inhomogeneous due to the presence of obstacles below, and spatial patterns emerge in mean-flow quantities. Vertical transport initiated by the obstacles on the surface corresponds to a dispersive flux in the force balance that changes with height. Within the bottom urban canopy layer (UCL), all downwards-transported momentum from the upper layers is absorbed by the building drag. An illustration of the balancing forces in the urban sublayers is shown in Figure 2.3a.

2.4 Cumulative stresses and volume forces

Integrating the streamwise momentum budget (2.29) from some height z within the urban boundary layer to its top at height h,

$$\int_z^h F(z')\,\mathrm{d}z' = -\int_z^h \frac{\mathrm{d}\tau}{\mathrm{d}z'}(z')\,\mathrm{d}z' + \int_z^h f_D(z')\,\mathrm{d}z', \tag{2.36}$$

we obtain

$$\tau_F(z) = \tau(z) + \tau_D(z), \tag{2.37}$$

where the non-negative cumulative stress functions for pressure and drag are given by

$$\tau_F(z) = \int_z^h F(z')\,\mathrm{d}z', \tag{2.38}$$

and

$$\tau_D(z) = \int_z^h f_D(z')\,\mathrm{d}z'. \tag{2.39}$$

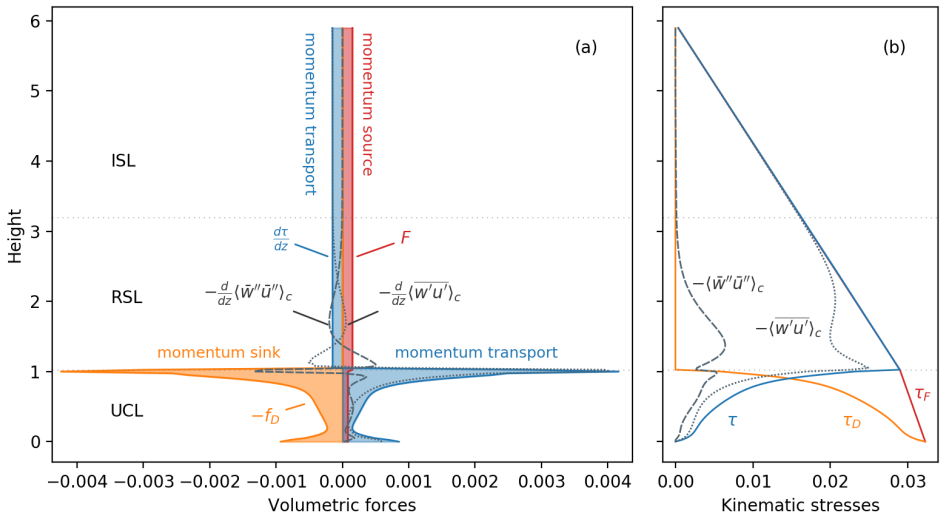

Figure 2.3: Momentum budget in the urban boundary layer. (a) Force balance of pressure F (momentum source) and drag f_D (momentum sink). Momentum transport $\mathrm{d}\tau/\mathrm{d}z$ consists of change of turbulent $-\mathrm{d}\langle\overline{w'u'}\rangle_c/\mathrm{d}z$ (dotted line) and dispersive $-\mathrm{d}\langle\overline{w}''\overline{u}''\rangle_c/\mathrm{d}z$ (dashed line) momentum fluxes. (b) Kinematic stresses τ_F, τ_D, and τ show the areas under F, f_D, and $-\mathrm{d}\tau/\mathrm{d}z$, integrated downwards. Data from simulation S1 (see Section 3.4).

Figure 2.3b illustrates the kinematic stresses in Eq. 2.37. The stress profile of the constant pressure force $\tau_F(z)$ does not extend as a straight line due to the volume occupied by buildings within the UCL. The function $\tau_D(z)$ accumulates the drag force exerted by the buildings from the highest building point throughout the urban canopy layer, reaching the total canopy drag at the ground surface. There, total net momentum sinks and sources are equal, which means that $\tau_D(0) = \tau_F(0) \equiv \tau_0$, where the kinematic surface stress τ_0 represents the effective drag of the urban canopy.

The total drag force F_D due to the urban canopy is thus given by

$$\begin{aligned} F_D &= \rho_0 A_T \int_0^h f_D(z')\,\mathrm{d}z' = \rho_0 A_T \int_0^h F(z')\,\mathrm{d}z' \\ &= \rho_0 F_x \int_0^h A_a(z')\,\mathrm{d}z' = \rho_0 F_x V_a, \end{aligned} \tag{2.40}$$

where $V_a = \int_0^h A_a(z')\,\mathrm{d}z'$ is the volume of air inside the domain.

3

Large-eddy simulations of urban neighbourhoods

Regional numerical weather prediction models typically represent buildings by ground-based surface-cover parameters such as plan area index λ_p (buildings' plan area per unit plan area) and frontal area index λ_f (buildings' frontal area per unit plan area). The vertical extent of buildings is often simply represented by an average building height z_H. These geometric parameters are used to describe the aerodynamic effect of buildings, commonly in terms of a logarithmic wind profile with a displacement height z_d and roughness length z_0 (e.g., Porson et al. 2010a). However, there are large uncertainties associated with estimating the functional relation between the surface geometry and the aerodynamic roughness parameters (Grimmond and Oke 1999; Hagishima et al. 2009; Kanda et al. 2013; Kent et al. 2017).

Moreover, real urban canopies have a vertical structure, where building density and frontal area vary with height. Several studies have highlighted that an average building height is an insufficient representation of the real urban environment and that the maximum building height, even in case of an isolated tall building, has a disproportionately large impact on the velocity and building drag of urban areas (Xie et al. 2008; Millward-Hopkins et al. 2011; Kanda et al. 2013; Hertwig et al. 2019).

This chapter describes a study set-up to systematically explore aero-

dynamic effects of heterogeneous building forms. Large-eddy simulations of urban neighbourhoods with identical λ_p and λ_f, but different configurations of building heights, plan areas, and street layout are to be investigated. These urban morphologies would have the same representation in some NWP models (e.g. the same normalised roughness length z_0/z_H in MacDonald et al. 1998). By studying their individual flow responses, we therefore explore the heterogeneity on the NWP subgrid level.

Section 3.1 gives a brief motivation for large-eddy simulations and Section 3.2 introduces the large-eddy simulation model uDALES. The development of the Urban Landscape Generator, which is the tool to create heterogeneous urban morphologies with prescribed plan area index and frontal area index, is documented in Section 3.3. Section 3.4 describes the set-up of nine different morphologies and the numerical simulations.

3.1 Large-eddy simulations

Turbulence is generated by both mechanical and thermal processes (Oke et al. 2017). Mechanical turbulence is a result of wind shear. In urban settings, this is generated by the urban form: flow displacement by buildings, wakes, and surface friction generate velocity gradients, the flow becomes dynamically unstable and turbulent eddies are created, leading to a cascade of energy to smaller scales. Thermal turbulence is caused by the release of heat from the urban elements: air close to building- and street-surfaces heats up and rises as thermals, which creates temperature gradients and turbulent mixing with the surrounding, cooler air. The dynamic stability of the atmosphere describes the dominant production type of turbulence (Oke et al. 2017). Under neutral stability, mechanical production prevails, whereas unstable stability characterises the dominance of thermal turbulence production. Since we are interested in studying effects of heterogeneous building forms, we will be studying a neutral atmosphere and ignore any buoyancy effects (e.g. from surface heating).

The vital role of turbulence in vertical transport processes was discussed in the previous chapter. Large-eddy simulations (LES) resolve a large portion of the energy-containing turbulent eddies in the flow, and parameterise only the small eddies below a certain filter width. LES models are there-

fore able to capture important dynamical processes such as unsteady flow separation and vortex shedding associated with flow in urban canopies, and approximate the dynamics on smaller scales, which have a more universal character (Pope 2000). In most LES models, including uDALES, the filter width is identical to the spatial grid resolution, which means that turbulent motion on length scales below the grid-cell size (subgrid-scale, SGS) need to be parameterised (Heus et al. 2010).

3.2 uDALES model

uDALES is a large-eddy simulation model for urban environments, which is capable of modelling a variety of urban case studies (Tomas et al. 2015, 2016; Suter 2018; Grylls et al. 2019, 2020; Grylls and van Reeuwijk 2021; Sützl et al. 2021b). The model extends the Dutch Atmospheric Large-Eddy Simulation model (DALES, Heus et al. 2010), with the capability to place building blocks in the domain, using an immersed boundary method (Tomas 2016). DALES is designed for studies of the physics of the atmospheric boundary layer, including cloudy, moist, convective and stable boundary layers. It has been used for over 30 years and is one of the most all-round tested available LES codes for studies of atmospheric processes, being tested both in intercomparison and against observational studies (Heus et al. 2010).

The extension uDALES has a surface energy balance scheme (Suter 2018), which models radiation, heat- and moisture-exchange between the building- and street-surfaces, as well as an atmospheric chemistry scheme (Grylls et al. 2019) to model dispersion and chemical reactions of pollutants. uDALES has been validated against wind- and water-tunnel data for idealised geometries (Tomas 2016; Tomas et al. 2016) and against wind-tunnel data for a realistic urban environment including passive scalar dispersion (Grylls 2019).

The immersed boundary method (Tomas 2016) models the solid building boundaries by adapting body force terms in the grid cells adjacent to the boundaries, such that there is no flow through the building walls. The buildings need to conform to the grid, which means that diagonal or slanted surfaces cannot be represented by the immersed boundary method. Subgrid-scale dynamics close to the building walls and street surface are paramet-

erised by logarithmic wall functions (Uno et al. 1995; Suter 2018).

The governing equations of motion with neutral atmospheric stability of uDALES are

$$\frac{\partial u_i}{\partial x_i} = 0, \tag{3.1}$$

$$\frac{\partial u_i}{\partial t} = -\frac{\partial u_i u_j}{\partial x_j} - \frac{\partial \Pi}{\partial x_i} - \frac{\partial \tau_{ij}^s}{\partial x_j} + F_i, \tag{3.2}$$

with (filtered) velocity components u_i along the spatial directions x_i, time t, and the modified kinematic pressure $\Pi = \frac{p}{\rho_0} + \frac{2}{3}e^s$, where p is the pressure, ρ_0 is the density of air and e^s is the subgrid-scale turbulent kinetic energy. Furthermore, τ_{ij}^s is the deviatoric subgrid-scale momentum flux tensor and F_i represents other forces on the flow, including large-scale forcings and the immersed boundary forcing.

The subgrid stresses are modelled as

$$\tau_{ij}^s = -K_m \left(\frac{\partial u_i}{\partial x_j} + \frac{\partial u_j}{\partial x_i} \right), \tag{3.3}$$

where K_m represents the eddy viscosity, which is modelled using the Vreman (2004) subgrid-scale scheme. The numerical scheme for spatial discretization is second-order central differences on a staggered Arakawa C-grid, where pressure and the subgrid-scale turbulence kinetic energy are defined at grid-cell centres, and the velocity components at different grid-cell sides. The time integration scheme is explicit third-order Runge–Kutta, where the timestep Δt is adapted at each iteration such that Δt is limited by the Courant–Friedrichs–Lewy (CFL) criterion

$$\Delta t \left| \frac{\widetilde{u}_i}{\Delta x_i} \right| \leq C_{\max} \tag{3.4}$$

and diffusion number

$$\Delta t \sum_i \frac{K_m}{\Delta x_i^2} \leq d_{\max}, \tag{3.5}$$

where Δx_i denotes the spatial grid spacing (Heus et al. 2010). We use $C_{\max} = 1.5$ and $d_{\max} = 0.25$ (cf. Tomas 2016).

3.3 Urban Landscape Generator for heterogeneous morphologies

The Urban Landscape Generator (ULG) is an algorithm generating randomised urban landscapes, which was developed for this thesis. It is designed as a procedural algorithm to generate a range of idealised heterogeneous urban morphologies that have a prescribed plan area index λ_p and frontal area index λ_f. Generic urban morphologies have the advantage over real city data that they allow us to gradually move from idealised layouts, as they have been used for studies of urban airflow, to more complex and realistic layouts with a controlled change of parameters. It is further possible to generate arbitrarily many maps with similar descriptive morphology parameters, which is particularly useful to understand the heterogeneity within such a parameter set. The tool is available as open-source code at https://github.com/bss116/citygenerator (Sützl and van Reeuwijk 2020).

3.3.1 Procedural generation of urban morphologies

Procedural modelling, which describes algorithms generating output based on a set of rules and some input parameters, can be applied amongst other things to generate structures of natural growth, including plants, trees or even entire cities (Kelly and McCabe 2006; Smelik et al. 2014). Fractals in particular are generated by recursive algorithms that produce scale invariant and self-similar structures which are well observed in nature, for instance in the formation of snowflakes and in plant growth, and are also attributed to the organic growth of cities (Batty and Longley 1994). Models for procedural generation of cities are available for computer-graphics applications (e.g. Parish and Müller 2001; Aliaga et al. 2008; Biljecki et al. 2016), however, these models focus on visual outputs and often do not produce three-dimensional buildings, which are required for urban fluid dynamics simulations.

The Urban Landscape Generator is designed to gradually introduce more realistic features to idealised urban environments, such as variable building heights and shapes, and more complex street networks. The ULG creates fractal-like street networks by dividing building blocks into smaller blocks

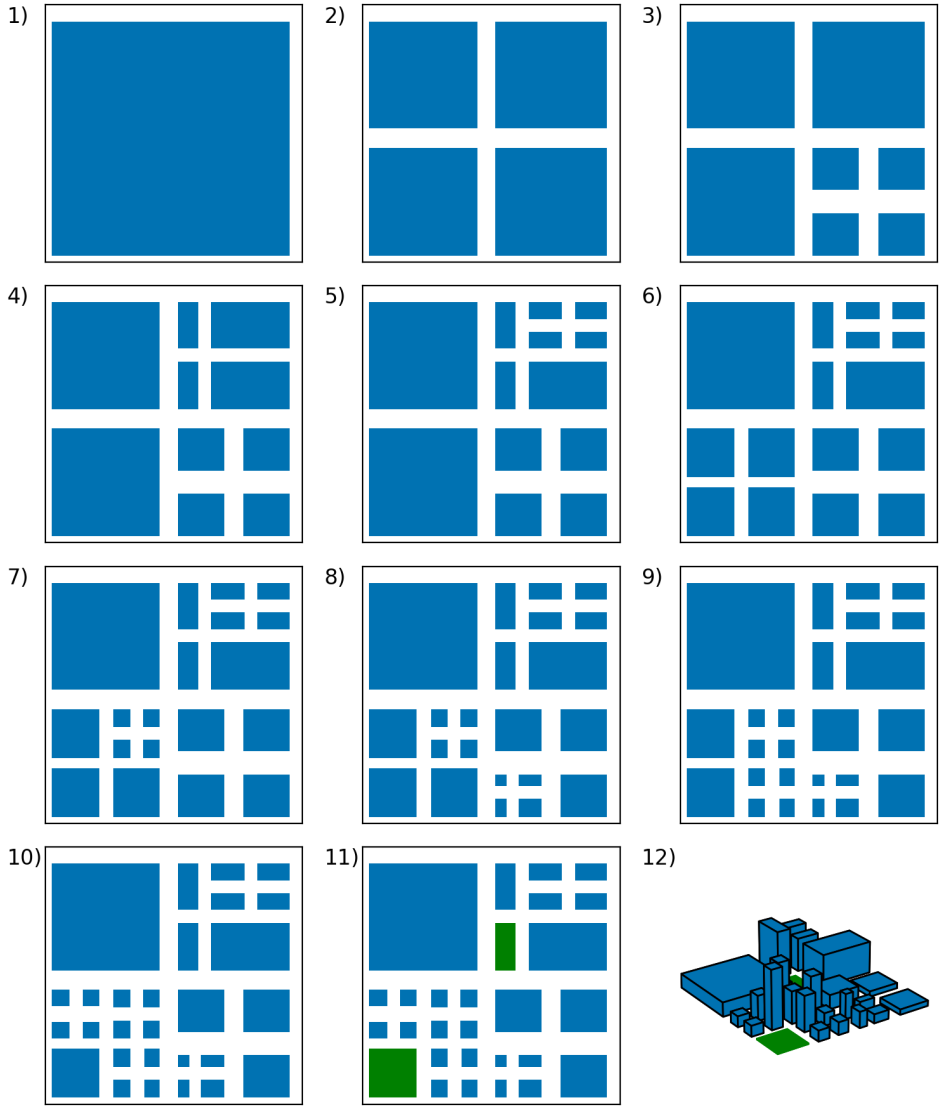

Figure 3.1: Step-by-step generation of a random urban landscape with the ULG.

until the target building plan area density is reached. Building heights are then chosen to reach the target frontal area density. The resulting buildings are cuboid-shaped and their faces are aligned in the streamwise and cross-stream directions. The ULG has parameters to control the level of randomness in the urban morphology. Layouts with little randomness are similar to the set-ups of generic block simulations, i.e. similar shaped and aligned blocks, as previously used in studies of idealised urban geometries

Algorithm 3.1 Main loop of the Urban Landscape Generator (ULG).

 # Input: domain D (with area A_D), target plan area index λ_p, target frontal area index λ_f, fractal type $\mathcal{F}$, layout randomness γ_l, height randomness γ_h.

 # Output: three-dimensional blocks $\{B_{3D}\}$.

function GENERATE FRACTAL LAYOUT(D, λ_p, λ_f, $\mathcal{F}$, γ_l, γ_h)

Set the initial block $\{B\} = D$ with block area $A_B = A_D$.

while $A_B > A_D\lambda_p$ **do**

B_n = CHOOSE A BLOCK($\{B\}$, $\mathcal{F}$)

B_{n_1}, B_{n_2}, B_{n_3}, B_{n_4} = GENERATE NEW BLOCKS(B_n, γ_l)

Sum up block areas A_B.

$\{B_{3D}\}$ = ADD HEIGHTS($\{B\}$, λ_f, γ_h)

return $\{B_{3D}\}$

(e.g. Coceal et al. 2006). A more organic city layout can be obtained by increasing the randomisation. The resulting layouts are of self-similar structure, this means that they have similar statistical properties at many scales and therefore they are also useful to describe urban landscapes on different scales, for instance they can describe both the layout of individual buildings and the layout of entire similar structured neighbourhoods.

3.3.2 Urban Landscape Generator algorithm

At the start the Urban Landscape Generator initialises the full domain as first block. The algorithm then chooses a street intersection within the block to subdivide the block into four new blocks. For as long as the sum of the newly created block areas is larger than the target plan area, the algorithm continues subdividing blocks. Figure 3.1 illustrates the steps of the algorithm to generate a two-dimensional layout. Once the target plan area density is reached, the algorithm attributes heights to each block to generate a three-dimensional urban landscape. Looping over all blocks, the building height is increased until the overall target frontal area density is met. The main routine of the ULG algorithm is summarised as a pseudo-code in Algorithm 3.1.

To generate an urban morphology including park areas, a green space

Algorithm 3.2 Choosing a block from the current layout for further subdivision. Different fractal types return different blocks.

function CHOOSE A BLOCK(blocks, fractal type $\mathcal{F}$)
  if $\mathcal{F}$ is 'random' **then**
    Select a random block.
  if $\mathcal{F}$ is 'hierarchical' **then**
    Select the next block on same level of hierarchy.
    If there is none, select the first block on the hierarchy level below.
  if $\mathcal{F}$ is 'cascade' **then**
    Select the largest block on the hierarchy level below.
  return selected block

density λ_g may be specified. In such case, the algorithm creates blocks based on $\tilde{\lambda}_p = \lambda_p + \lambda_g$. After finalising the two-dimensional layout, the algorithm selects one or several blocks that together have a plan area approximately equal to λ_g and converts them into green space. A layout with green space is shown in Figure 3.2f.

Fractal types On the street level, heterogeneity is introduced by specifying a fractal type, which determines how a block is chosen for subdivision (Algorithm 3.2). The 'hierarchical' type chooses the blocks in a set order, such that all blocks on the same level of hierarchy are divided first, before going into a lower hierarchy level. This type produces fairly idealised structures, the simplest of which is a regular grid. With the 'cascade' type, each iteration goes down one level of hierarchy. The block that is further subdivided is the largest block of the most recently created blocks. This type creates fractal-structures in the most intuitive way, which are entirely scale-invariant. The 'random' type selects a random block out of all available blocks. If the selected block is too small for further subdivision, the algorithm selects the next suitable block. This type is designed to better resemble the organic growth of cities. Figure 3.2 shows layouts generated with the different fractal types.

Randomisation Different block shapes are generated using randomness parameters that control street widths and intersections, and the height of

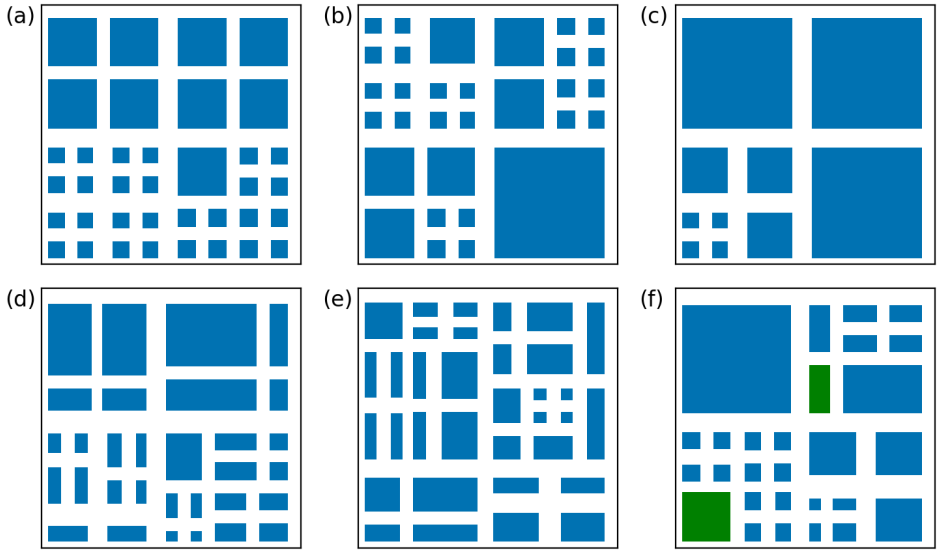

Figure 3.2: Fractal types and randomness of the Urban Landscape Generator. (a) Hierarchical layout, no randomness ($\gamma_l = 0$). (b) Random layout, no randomness. (c) Cascade layout, no randomness. (d) Hierarchical layout with randomness ($\gamma_l = 0.6$). (e) Random layout with randomness ($\gamma_l = 0.7$). (f) Random layout with randomness ($\gamma_l = 0.4$) and green space.

blocks. The ULG draws sample values from a probability distribution across a given interval, which is defined using a randomness parameter γ. The following distribution is implemented in the ULG, which allows to gradually move from idealised to more heterogeneous building forms (Algorithm 3.3): No randomness $\gamma = 0$ returns a pre-set value from the interval. With randomness $\gamma = 1$ the algorithms chooses freely from the given interval. For $0 < \gamma < 1$, the algorithm chooses points such that the probability of obtaining the pre-set value is γ, the remaining probability is uniform across the rest of the interval. Algorithm 3.3 is written as a separate module to the code and can therefore easily be modified or replaced, e.g. with a distribution based on morphology data.

The subdivision of a block is controlled by the layout-randomness parameter γ_l (Algorithm 3.4). Realistic values for street widths of various types (e.g. high street, residential street; following Department for Transport 2007) are defined for each level of hierarchy. For the subdivision, two street widths are sampled from these intervals using Algorithm 3.3, and two subdi-

Algorithm 3.3 Default probability density function of the ULG used for randomisation of layouts and heights.

function RANDOMISER(I, S, γ)

 # Sample random number R from interval I and standard output S with randomness $0 \leq \gamma \leq 1$.

Define uniform distribution $U(I)$ over interval I.

Define probability density function $p(x \in I) = (1 - \gamma)S + \gamma U(I)$.

Draw a random number R from $p(x)$.

return R

Algorithm 3.4 Generation of four new blocks by subdividing an existing block, applying layout randomisation.

function GENERATE NEW BLOCKS(B_n, γ_l)

Define possible street widths W and the standard width W_S.

Select two widths w_x, w_y with RANDOMISER(W, W_S, γ_l).

Define possible subdivision points for both block sides L_x, L_y with mid-points M_x, M_y.

Select points i_x with RANDOMISER(L_x, M_x, γ_l) and i_y with RANDOMISER(L_y, M_y, γ_l).

Divide block B_n at intersection (i_x, i_y) with street widths (w_x, w_y) into new blocks B_{n_1}, B_{n_2}, B_{n_3}, B_{n_4}.

return B_{n_1}, B_{n_2}, B_{n_3}, B_{n_4}

visions (one for each side of the block) are randomly assigned: the probability of obtaining the mid-points of the block sides is γ_l, the remaining probability is uniform across the rest of the block sides, obeying certain margins at the edges. The two widths and subdivision points define the new street intersection that divides the block into four new blocks.

The height of the blocks is randomised using the height-randomness parameter γ_h (Algorithm 3.5). Uniform heights are added to the blocks with probability $1 - \gamma_h$; the probability of a random height from a range of possible values is γ_h.

Algorithm 3.5 Loop to attribute heights to blocks, applying height randomisation.

function ADD HEIGHTS($\{B\}$, λ_f, γ_h)
  # Adds heights to blocks B_n in $\{B\}$ and returns 3D blocks $\{B_{3D}\}$.
  Calculate the block's total frontal area A_F.
  while $A_F \leq A_D \lambda_f$ **do**
    Define possible block heights H and a standard height H_S.
    Select a height with RANDOMISER(H, H_S, γ_h) and add to block.
    Sum up block frontal areas A_F.
    Go to the next block.
  return $\{B_{3D}\}$

3.4 Simulation of idealised heterogeneous urban environments

3.4.1 Layout set-up

Nine different urban morphologies S1–S9 were set up using the Urban Landscape Generator. All layouts have a plan area index of $\lambda_p = 0.45$–0.46 and frontal area index of $\lambda_f = 0.22$, but different numbers, shapes and heights of buildings. The values for λ_p and λ_f are representative for compact urban environments, such as residential neighbourhoods (Grimmond and Oke 1999; Oke et al. 2017). The morphologies of S1–S9 are generic urban layouts which span from idealised, uniform building forms to more complex, heterogeneous building shapes and heights. The layouts are illustrated in Figure 3.3.

Layout S1 contains a single block with the plan area and height matching λ_p and λ_f. Layouts S2–S4 were generated with a 'hierarchical'-type street network without any randomness. The plan area of S3 and S4 is identical, however layouts S1–S3 have uniform building heights, whereas S4 has non-uniform building heights. Note that S1 and S2 have approximately the same structure but at different scales. However, the length scale bounding the flow (in this case the model domain, or the inversion height in the environment) produces different flows, as will be evident later. Layout S5 was generated with the 'hierarchical'-type street network and some randomness regarding the intersection points, street widths and building heights. Layouts S6–S9 have a 'random'-type street network and also randomness in

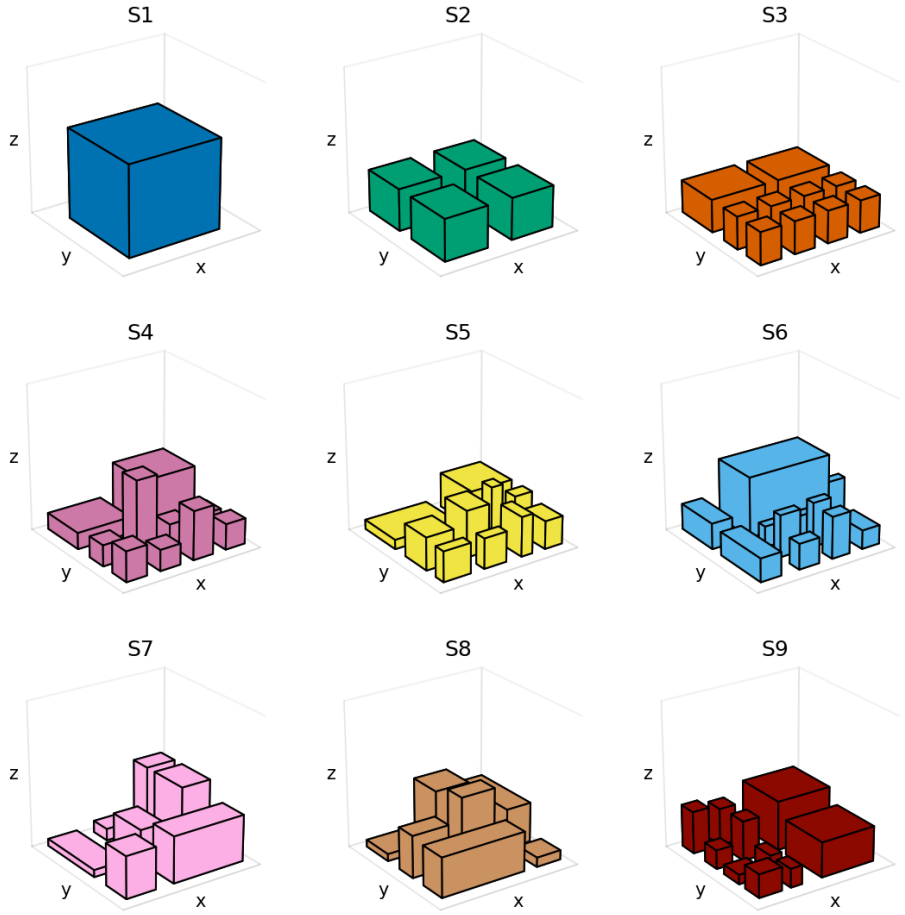

Figure 3.3: Heterogeneous morphologies for simulations S1–S9, generated with the urban landscape generator.

the street intersections, widths and building heights, thus representing the most heterogeneous layouts.

The morphologies can be described by their building geometry statistics, which are shown in Table 3.1. The most commonly used quantities (apart from λ_p and λ_f) focus on building heights. They are the mean building height z_H (Equation 1.3 with $w_n = 1/N$), the maximum building height $z_{\max} = \max_n B_{h,n}$, and the building height standard deviation

$$\sigma_H = \sqrt{\sum_n w_n (B_{h,n} - z_H)^2} \tag{3.6}$$

with $w_N = 1/N$. From these three parameters it becomes clear that a

	N	z_H [m]	$z_{H,f}$ [m]	$z_{H,p}$ [m]	$z_{\max}$ [m]	σ_H [m]	$\sigma_{H,f}$ [m]	$\sigma_{H,p}$ [m]
S1	1	39	39	39	39	0	0	0
S2	4	18	18	18	18	0	0	0
S3	10	14	14	14	14	0	0	0
S4	10	14.1	18.07	14.05	32	7.62	8.42	7.31
S5	10	14.5	15.57	11.29	22	4.63	4.03	5.78
S6	10	15	17.28	18.39	26	5.67	7.13	7.72
S7	7	16.29	20.5	15.38	27	8.91	7.17	8.95
S8	7	15.86	19.6	15.88	28	8.68	5.8	7.53
S9	10	12.5	15.91	15.72	21	5.3	4.77	5.09

Table 3.1: Building statistics for morphologies S1–S9: number of buildings N, average building height z_H, maximum building height $z_{\max}$, average building height weighted by the frontal area $z_{H,f}$, average building height weighted by the plan area $z_{H,p}$, building-height standard deviation σ_H, building-height standard deviation weighted by frontal area $\sigma_{H,f}$ and by plan area $\sigma_{H,p}$.

major difference in the nine morphologies is whether the layouts have uniform building heights (S1–S3) or non-uniform building heights (S4–S9). To further quantify differences in the layouts, we use two additional definitions of mean height (cf. Grimmond and Oke 1999): an average height $z_{H,f}$ where each building height is weighted by its frontal area ($w_n = A_{f,n}/A_F$), and an average height $z_{H,p}$ where buildings are weighted by their plan area ($w_n = A_{p,n}/A_P$). Weighted standard deviations $\sigma_{H,f}$ and $\sigma_{H,p}$ are defined as in Equation 3.6 with the respective weights and weighted means.

3.4.2 Numerical set-up

The simulation domain-size is 480 × 240 × 234 m with a horizontal resolution of 2 m. The vertical resolution is constant at 1 m for the lower half of the grid cells and stretched thereafter with a stretching ratio of 1.01. Each layout describes a 120 × 120 m region and is repeated eight times within the domain (see Fig. 3.4). With the domain length in the streamwise direction about twice the domain height, large eddies can fully traverse the domain without interference. Repeating the layouts within the domain improves the converge of the averages in the spatially inhomogeneous parts

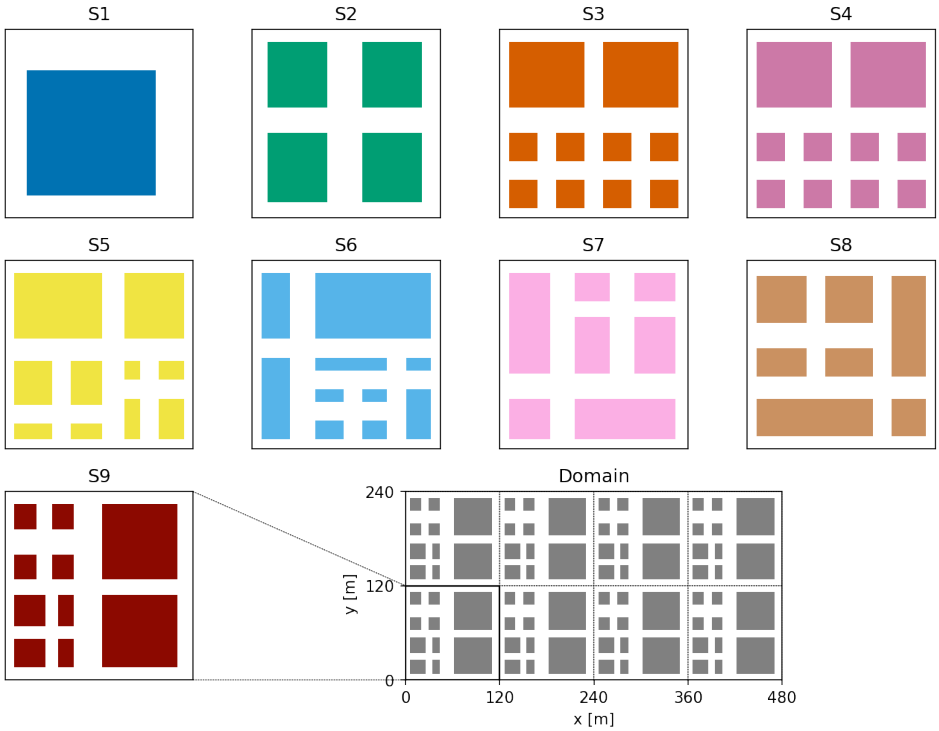

Figure 3.4: Building plan area of simulations S1–S9. Layouts are repeated eight times within the simulation domain.

of the flow (i.e. within the roughness sublayer). A very large domain with many repeating layouts could indeed be considered as ensemble average over the layout. Although eight repetitions are far too few for a representative ensemble average (and therefore it is essential to average in time as well), testing the simulations with a single, four, and eight layouts has shown that more repetitions generally yield faster convergence of turbulence statistics.

Periodic boundary conditions (BCs) are applied in the lateral directions, which implies that the simulations capture the atmospheric flow in a larger urban area with similar morphology characteristics outside the modelled domain. Periodic BCs further allow for statistically stationary boundary layers, which means that the flow is horizontally homogeneous and stationary in the inertial sublayer. This allows us to express the mean and turbulent state of the boundary layer by one-dimensional vertical profiles, that are representative for the whole domain. The domain-top boundary condition for momentum is free-slip (no flow through the boundary), and the boundary

	Simulations
Grid size	240×120×180
Domain size [m]	480×240×234
Flow forcing [m s^{-1}]	$\langle u \rangle = 2$
x momentum BC	Periodic
y momentum BC	Periodic
top momentum BC	Free-slip
bottom momentum BC	No-slip
building momentum BC	No-slip
Run-up time [s]	10,000
Averaging period [s]	80,000

Table 3.2: Details of the simulation set-up and boundary conditions (BCs).

conditions at the bottom and building facets are no-slip (the flow velocity is zero at the boundary) via the wall-functions.

For each of the simulations the domain-average wind velocity is kept constant at $\langle u \rangle = 2$ m s^{-1}, and the pressure-gradient forcing therefore varies in time. Since the drag will be different for each of the urban morphologies, this implies that the associated average pressure-gradient forcing will be different for each simulation. The simulation set-up is summarised in Table 3.2.

3.4.3 Averaging time scales

The simulations are spun up for 10,000 s, after which the pressure-gradient forcing of the simulations has stabilised. Examples of the pressure-gradient forcings for simulations S7 and S4, sampled every 5 s, are shown in Figures 3.5a and 3.6a. An averaging time of 20,000 s after the spin-up is sufficient to produce converged statistics for the momentum budget. This means that the pressure-gradient forcing derived from the statistical data does not significantly vary with longer averaging times. A visual representation of stable momentum-budget statistics is that the slope of the total vertical momentum flux is a straight line, which means that the average momentum-exchange is constant in the ISL and independent of time (cf. Figures 3.5b–d and 3.6b–d).

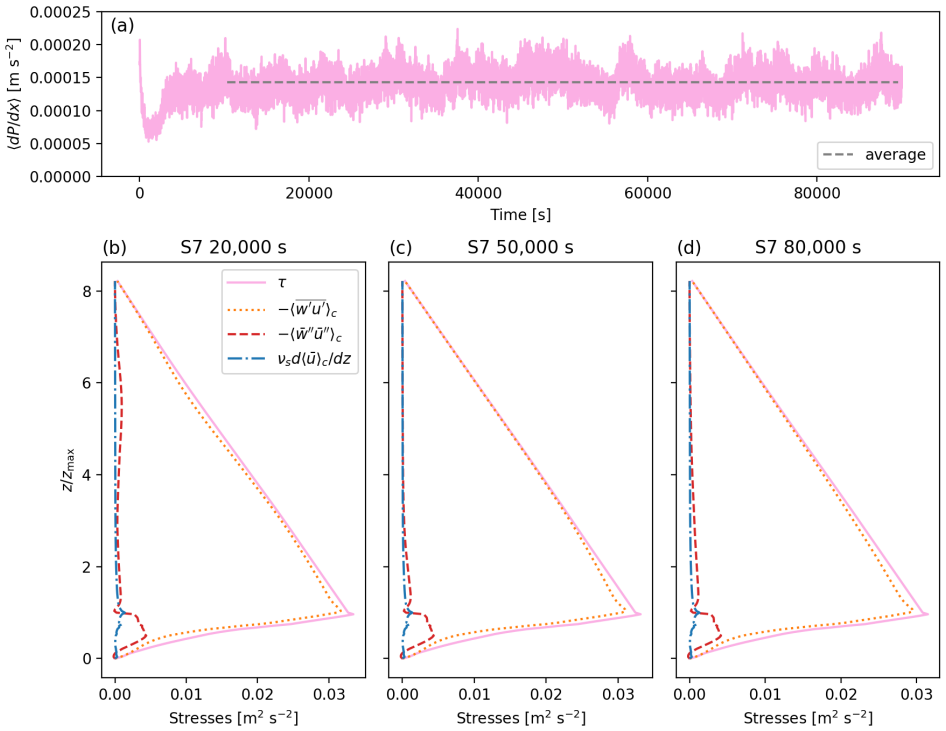

Figure 3.5: Convergence of turbulence statistics for simulation S7. (a) Pressure-gradient forcing at 5 s sampling time and 80,000 s-average (dashed grey line). Simulations with 20,000 s (b), 50,000 s (c) and 80,000 s (d) averaging time after 10,000 s spin-up.

For the correct attribution of dispersive stresses, a much longer averaging time is required (Coceal et al. 2006). We tested several averaging times (20,000 s, 50,000 s, 60,000 s and 80,000 s) for all nine simulations. Most simulations seemed to be converged or nearly-converged by 50,000 s. Therefore, the dispersive fluxes between averaging times 50,000 s and 80,000 s are near-identical. An example of converged statistics at these averaging times is shown in Figure 3.5c and d (dispersive stresses are dashed red lines). The simulations S3 and S4 appear to have longer transient phases. While the shape of the dispersive flux within the canyon is largely unchanged for the tested averaging times (cf. the dispersive flux of S4 below $z/z_{\max} = 1$ in Figure 3.6b–d), above the canyon signs of slowly evolving mean streamwise circulations may appear even after considerable averaging time. These structures are counter-rotating mean circulations above the buildings, which

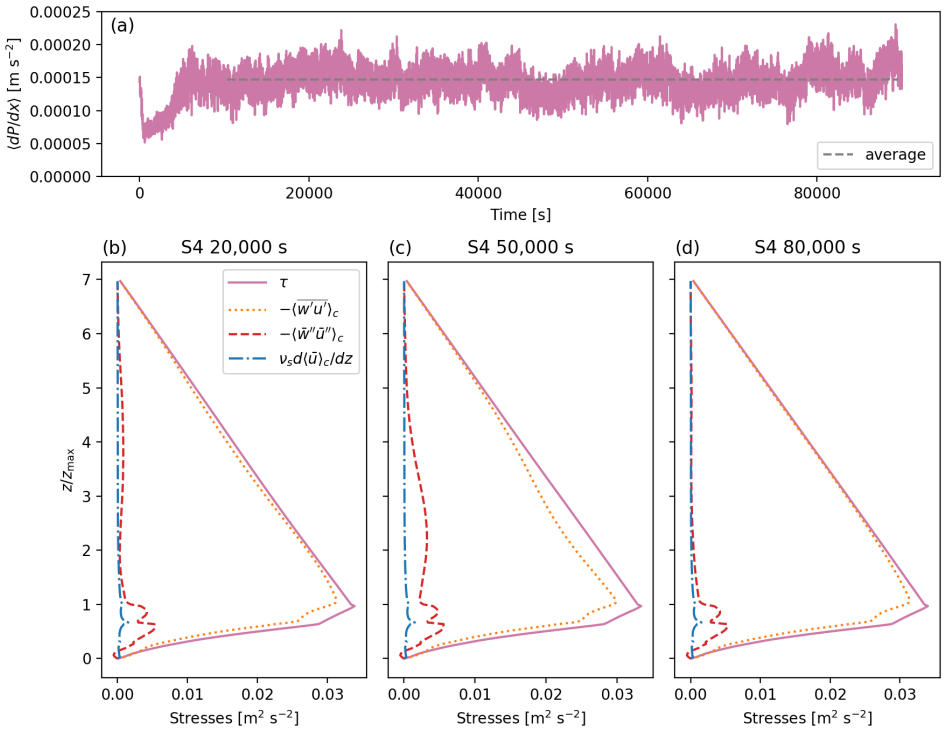

Figure 3.6: Convergence of turbulence statistics for simulation S4. (a) Pressure-gradient forcing at 5 s sampling time and 80,000 s-average (dashed grey line). Simulations with 20,000 s (b), 50,000 s (c) and 80,000 s (d) averaging time after 10,000 s spin-up.

manifest in increasing dispersive stresses above the canyon with a peak in dispersive stresses at the height of the cores of these eddies (cf. Coceal et al. 2006), as seen for 50,000 s averaging time in Figure 3.6c. With 80,000 s averaging times, these slow-transient structures in the dispersive flux above the canyon were averaged out (Figure 3.6d). Simulation runs with averaging time of 80,000 s were used for further analysis. Simulation S3 experiences more persistent slow-transient flow structures, and we therefore increased the averaging time to 100,000 s for this simulation to obtain converged statistics.

4

Neighbourhood-scale simulation results

This chapter analyses the simulation data of idealised, heterogeneous urban neighbourhoods. Starting with an example of the complexity of the instantaneous flow (Section 4.1), we discuss the vertical mean-flow profiles thereafter in Section 4.2. To assess how these flows may be parameterised, we estimate aerodynamic roughness parameters (displacement height z_d and roughness length z_0) for logarithmic wind profiles in Section 4.3. First, a friction velocity u_* is calculated from the total urban canopy drag, and the aerodynamic roughness parameters are estimated from the mean-wind profiles. These parameters are then compared with values predicted from the standard parameterizations in MacDonald et al. (1998) and Kanda et al. (2013), and afterwards correlated to the building statistics of the different morphologies. Section 4.4 analyses the vertical transport of horizontal momentum, including the separate contributions of turbulent and dispersive momentum fluxes. Section 4.5 proposes an new parameterization for airflow in urban environments. A normalised frontal area function and the simulation data are used to derive a model that describes the vertical distribution of drag inside the urban canopy. Contrary to parameterizations for logarithmic wind profiles which model urban areas in NWP as boundary conditions to the governing flow equations, the proposed parameterization

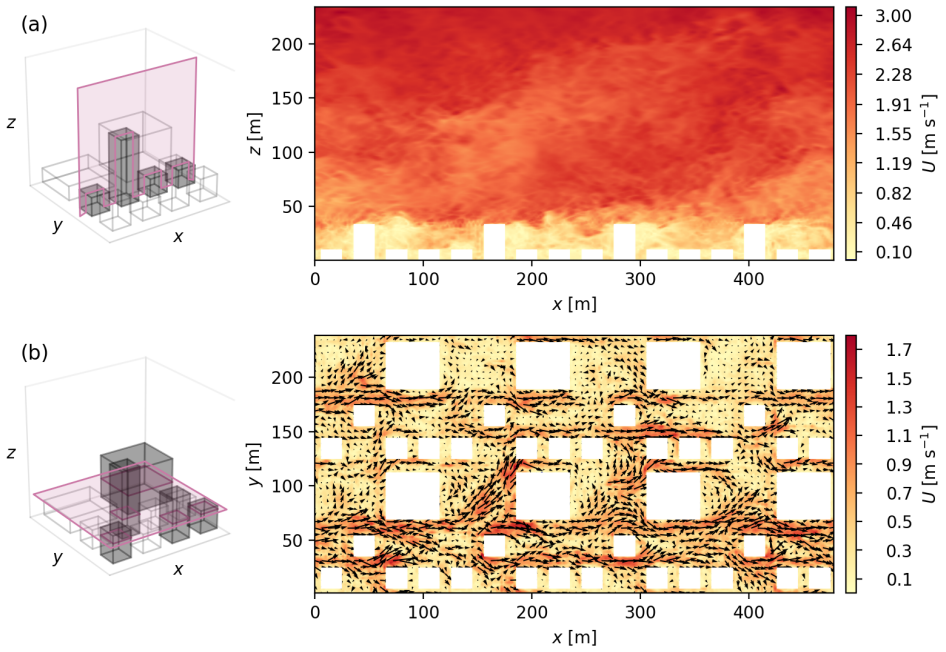

Figure 4.1: Instantaneous wind-speed field of simulation S4 in a vertical (a) and horizontal (b) section.

presents a height-dependent, explicit stress term which is directly added to the momentum equations.

4.1 Instantaneous flow fields

Instantaneous flow fields reveal significant features of the fully developed turbulent flow around buildings. Figure 4.1a shows a vertical section of instantaneous horizontal wind speed $U(t,x,y,z) = \sqrt{u(t,x,y,z)^2 + v(t,x,y,z)^2}$ for simulation S4, which has heterogeneous building heights. The influence of the buildings extends well above the maximum height and particularly the wakes of tall buildings show wind sheltering effects (Xie et al. 2008). The flow shows great spatial variability despite the repeated layouts. Figure 4.1b shows a horizontal section of the same wind field with wind velocity components $(u(x,y), v(x,y))$. Within the urban canyon, street corridors are important for redistributing the displaced air, with much higher wind speeds than more sheltered areas of the domain. The complex flow around the buildings varies substantially in wind speed and direction.

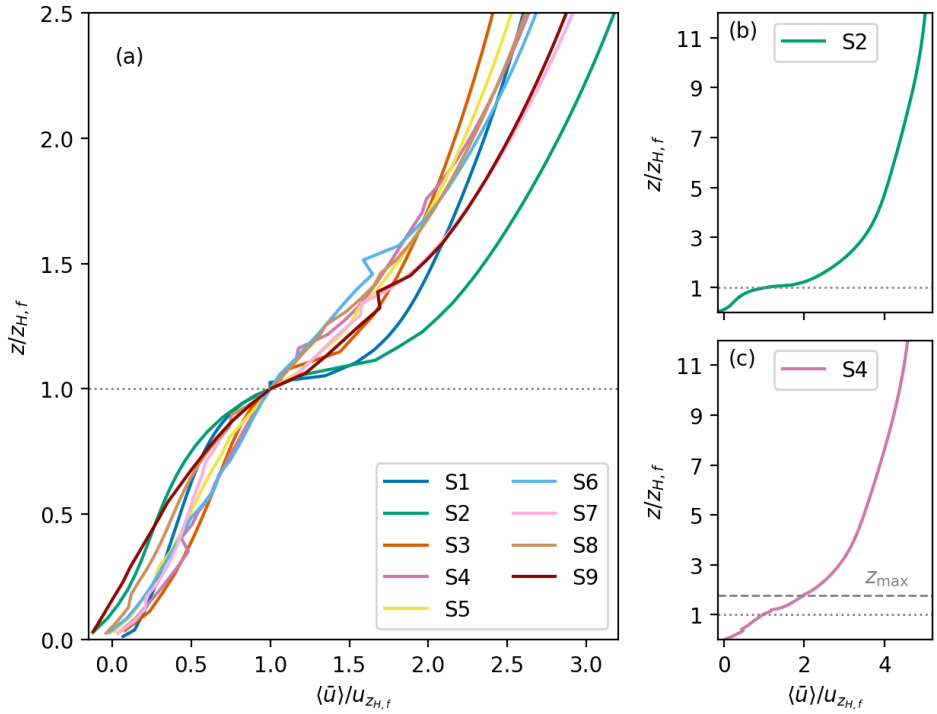

Figure 4.2: Normalised wind profiles of simulations S1–S9 in and above the urban canopy (a). Wind profiles of simulation S2 with uniform building heights (b) and simulation S4 with non-uniform building heights (c).

4.2 Mean flow

Figure 4.2 shows profiles of the average streamwise wind velocity $\langle\overline{u}\rangle(z)$, with height and wind normalised by the weighted mean height $z_{H,f}$ and mean wind velocity at this height, respectively. The mean-wind profiles of simulations with uniform building heights (S1–S3) are evidently distinct from simulations with non-uniform building heights (S4–S9). Wind profiles of the simulations with uniform building heights show a clear separation in within-canopy flow and above-canopy flow with an inflection point around the top of the buildings. Within the canopy, airflow is obstructed by buildings and the velocity profile has a concave shape. Above the canopy, a typical boundary-layer profile develops quickly and the velocity profile changes to a convex shape. Simulations S4–S9 with heterogeneous building heights lack a clear separation in above- and within-canopy flow. The velocity profiles

within the canopy change more gradually compared to the uniform height simulations and their shapes are not clearly concave; an inflection point is not evident. The difference between the wind profiles of uniform S2 (b) and non-uniform S4 (c) is illustrated in Figure 4.2.

4.3 Aerodynamic roughness parameters

It is commonly assumed that the wind profile in the inertial sublayer can be approximated by a logarithmic profile (Tennekes 1973)

$$\langle \overline{u} \rangle(z) = \frac{u_*}{\kappa} \ln\left(\frac{z - z_d}{z_0}\right), \tag{4.1}$$

where u_* is the friction velocity, $\kappa = 0.4$ is the von Kármán constant, z_d is the displacement height and z_0 is the momentum roughness length. The parameters z_d and z_0 are of interest for weather or climate models, as they are often used to determine wind profile or exchange fluxes for near-surface flows over urban areas (see Chapter 6). Figure 4.3 illustrates the log law in Equation 4.1 with a given wind profile over uniform-height obstacles. It shows the logarithmic profile approximation of the wind by the right hand side of (4.1).

4.3.1 Estimation of roughness parameters

The displacement height and roughness length can be estimated with different methods from given observational or numerical data. An advantage of LES over observational data is the availability of complete vertical profiles of mean wind velocity $\langle \overline{u} \rangle(z)$. The friction velocity can be directly derived from (2.40) by

$$\tau_0 = F_D/(\rho_0 A_T) = F_x(V_a/A_T), \tag{4.2}$$

where $u_* = \sqrt{\tau_0}$ (recall that τ_0 is a kinematic stress).

Because the pressure gradient forcing F_x is not directly specified for the simulations in this study, the average $\overline{F_x}$ is estimated from the constant rate of downward momentum transfer in the inertial sublayer:

$$-\frac{\mathrm{d}\tau}{\mathrm{d}z}(z) = \frac{\mathrm{d}}{\mathrm{d}z}\langle \overline{w'u'} \rangle(z) = \overline{F_x}. \tag{4.3}$$

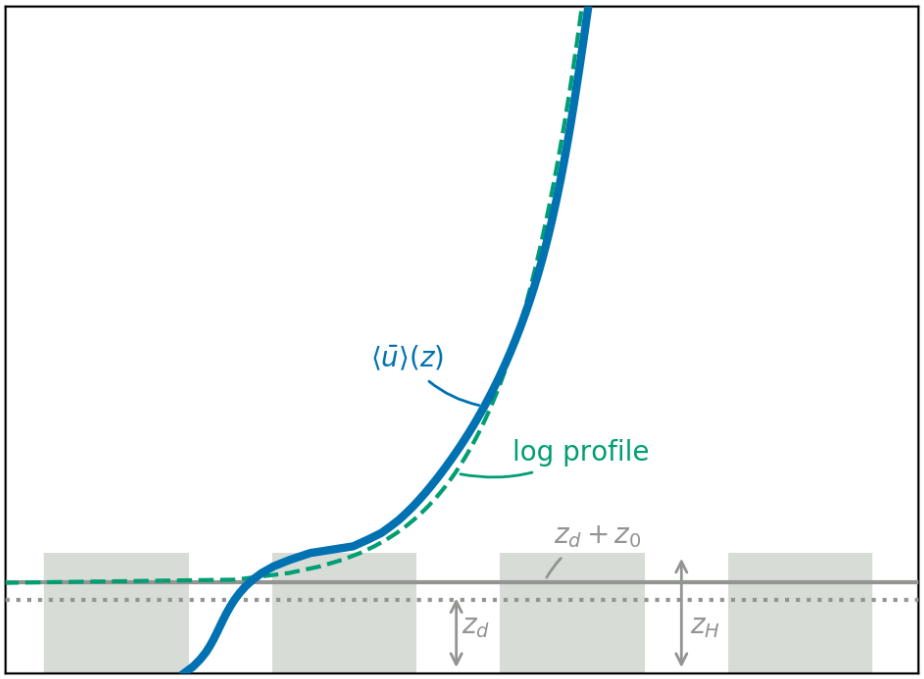

Figure 4.3: An illustration of the logarithmic wind law. The wind profile $\langle \bar{u} \rangle(z)$ over uniform-height obstacles (blue line) can be approximated by the logarithmic profile on the right hand side of (4.1) (dashed green line).

The average forcing $\overline{F_x}$ is calculated from a least-squares fit for $\tau(z)$ against z within the ISL. The friction velocities for simulations S1–S9 are shown in Table 4.1.

With u_* determined a priori, z_0 and z_d can be obtained by rewriting (4.1) as

$$z = z_0 \exp\left(\frac{\kappa}{u_*}\langle \overline{u} \rangle(z)\right) + z_d. \tag{4.4}$$

Given z and $\langle \overline{u} \rangle(z)$, linear regression can be used to estimate parameters z_d and z_0 as the slope and intercept of a least-squares fit.

Fitting range

The log law is assumed to be valid in the ISL, therefore only wind velocities from within the ISL should be used for the linear regression. Several fitting ranges were tested for the linear regression, and the logarithmic wind profiles resulting from the different parameter fits are shown in Figure 4.4.

First we tested the range of $[z_{\max} + 0.2z_H, z_{\max} + z_H]$ for each simulation, which is used by Kanda et al. (2013) for the same method of estimating z_d and z_0. This range is clearly still within the RSL, and the resulting logarithmic wind profiles are diverging from the simulation wind profiles above the height of $2z_{\max}$. We subsequently tested several fitting regions that are likely to be within the ISL: $[2z_{\max}, 2z_{\max} + 2z_H]$, $[3z_{\max}, 3z_{\max} + 2z_H]$, and $[4z_{\max}, 4z_{\max} + 2z_H]$ for each simulation. However, these ranges may exceed an upper limit to the log law with respect to the boundary-layer height, as argued in Jimenez (2004) for example. The resulting logarithmic wind profiles of these fitting ranges generally match well the wind-profile data above the height of $2z_{\max}$ and these three fitting ranges are used for further analysis.

Fitted wind profiles

For simulation layouts with uniform building heights, there is little difference between the different ISL fitting ranges, and the logarithmic wind profiles yield a good approximation to the LES wind profiles even within the RSL. For layouts with non-uniform building heights there can be significant differences in the logarithmic wind profiles, depending on the fitting range. The estimated logarithmic wind profiles vary strongly below the height of $2z_{\max}$, particularly for simulations with larger friction velocity and larger building-height variation (larger σ_H), showing that the log-law relation breaks down near the surface for strongly heterogeneous building heights. These strong variations in the lower parts of the logarithmic profiles suggest that the region where a logarithmic profile may be suitable is at least a length scale of height variation above the buildings. The difference between uniform and non-uniform layouts in Figure 4.4 can be seen for instance between the simulations S2 and S4.

A higher fitting range generally results in higher displacement heights and lower roughness lengths, and a better agreement between the estimated logarithmic and LES wind profiles higher up. Conversely, a lower range results in lower displacement heights and higher roughness lengths, with better agreement of the wind profiles closer to the canopy top. A similar trend is reported by Kanda et al. (2013) for their tests of various fitting regions. For the high fitting range and heterogeneous building-height mor-

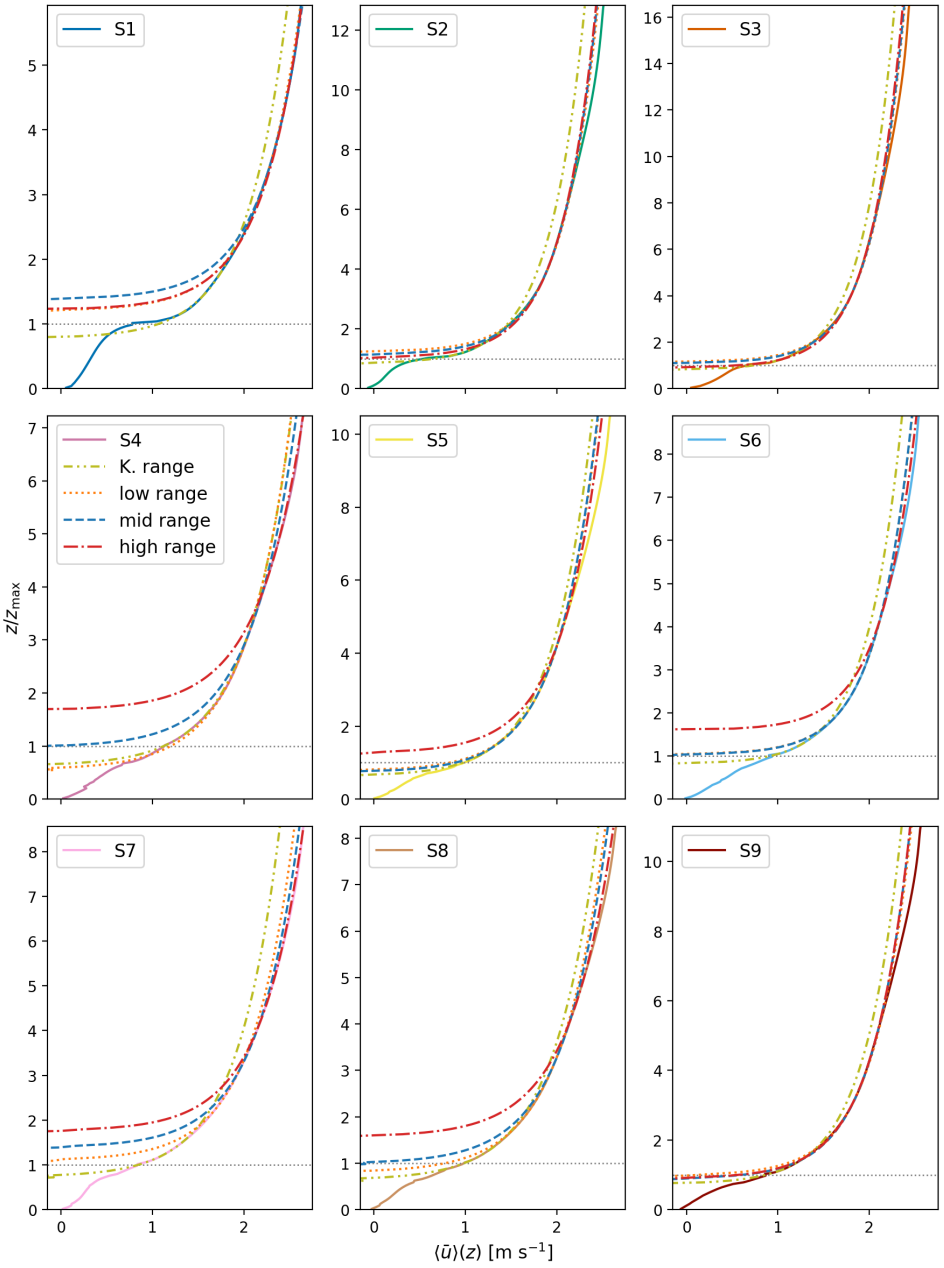

Figure 4.4: Estimated logarithmic wind profiles of S1–S9 with different fitting ranges: K. range = $[z_{max} + 0.2z_H, z_{max} + z_H]$, low range = $[2z_{max}, 2z_{max} + 2z_H]$, mid range = $[3z_{max}, 3z_{max} + 2z_H]$, high range = $[4z_{max}, 4z_{max} + 2z_H]$.

phologies, we observe a higher value for $z_d + z_0$ (this is the height where the logarithmic wind profile crosses the z-axis), whereas for homogeneous height

layouts this value is lower. For the low fitting range the values for $z_d + z_0$ are either lower or similar to the mid fitting range, with no particular distinction between homogeneous and heterogeneous building heights. Extending the fitting ranges to a longer interval by adding $3z_H$ to the start point did not significantly change the fits. Ranges of the estimated roughness parameters are presented in Table 4.1.

Fitting with a priori displacement height

An alternative calculation for the displacement height (e.g. used in Kanda et al. 2013; Castro et al. 2017; Giometto et al. 2017) follows a hypothesis by Jackson (1981), that the displacement height corresponds to the centre of moment of the forces acting on the buildings. In other words the displacement height is assumed to be the height level of the mean momentum sink. The centre of mass of a function is given by the first moment divided by the zeroth moment (i.e. the total mass). The centre of mass of the volumetric drag function is

$$\frac{\int_0^h z f_D(z)\,\mathrm{d}z}{\int_0^h f_D(z)\,\mathrm{d}z} = \frac{h\tau_D(0) - \int_0^h \left(\tau_D(0) - \tau_D(z)\right)\,\mathrm{d}z}{\tau_D(0)} = \frac{\int_0^h \tau_D(z)\,\mathrm{d}z}{\tau_0}, \tag{4.5}$$

which follows from integration by parts.

Rewriting the log law to

$$\ln(z - z_d) = \frac{\kappa}{u_*}\langle\overline{u}\rangle(z) + \ln(z_0) \tag{4.6}$$

yields an alternative form for linear regression, where the parameters κ/u_* and $\ln(z_0)$ are slope and intercept of a least-squares fit. Using (4.5) as estimate for z_d and consequently also $u_* = \sqrt{\tau_0}$, we must assume that κ is the variable parameter. Linear regression with fitting region $[3z_{\max}, 3z_{\max}+2z_H]$ yields new von Kármán parameters ranging from 0.29-0.37 and consistently lower displacement heights compared to the previous method. A reason for this may be that using the centroid of drag does not consider any displacement effects from dispersive fluxes in the roughness sublayer, opposed to the purely statistical fit of z_d. The lower displacement heights are partly compensated for by higher estimates for roughness length, compared to the previous log-law fits. However, a well-defined displacement height as the centre of drag comes at the cost of losing a fixed value for the von Kármán

	u_* [m s^{-1}]	z_d [m]	z_0 [m]	$z_{d,J}$ [m]	$z_{0,J}$ [m]	κ_J
S1	0.18	46.86–53.83	0.5–0.54	28.81	1.88	0.32
S2	0.15	18.54–22.12	0.36–0.38	12.52	0.9	0.34
S3	0.14	12.69–16.08	0.23–0.25	10.93	0.46	0.36
S4	0.19	17.72–53.45	0.77–1.22	14.84	2.59	0.33
S5	0.17	16.17–27.7	0.63–0.74	10.39	1.18	0.37
S6	0.15	26.71–41.48	0.26–0.32	15.11	0.85	0.34
S7	0.18	29.65–47.51	0.59–0.8	15.61	3.16	0.29
S8	0.19	22.46–43.91	0.83–1.11	14.11	2.41	0.34
S9	0.16	18.64–20.53	0.51–0.53	11.5	1.03	0.35

Table 4.1: Estimated values of logarithmic law parameters for simulations S1–S9. First column shows the friction velocity u_* estimated from LES data. Ranges for displacement height z_d and roughness length z_0 in second and third column are estimated with a least-squares fit from the logarithmic law. Values estimated using the Jackson (1981) hypothesis are labelled with a subscript J, including the then variable von Kármán parameter κ_J.

parameter, as the variability in κ shows. Using a constant $\kappa = 0.4$ instead of the estimated lower values would result in poor agreement between the wind and logarithmic profiles. Values for estimated z_d, z_0 and κ using (4.6) are listed in Table 4.1.

4.3.2 Comparison of roughness parameters

Figure 4.5 shows the estimated aerodynamic roughness parameters for each simulation, and compares them to values obtained from two standard parameterizations: MacDonald et al. (1998) and Kanda et al. (2013). The displacement height z_d and roughness length z_0 are normalised by the average height z_H of each simulation. A large spread in estimated roughness parameters for similar λ_p and λ_f is evident from this figure. It further shows that even with a detailed velocity height-profile and known friction velocity, the estimated displacement height z_d and roughness length z_0 for heterogeneous morphologies cannot be uniquely identified, because they depend on the selected fitting range of the data. Whilst this may partially be attributed to the limited domain height used in the simulations, it demonstrates intrinsic

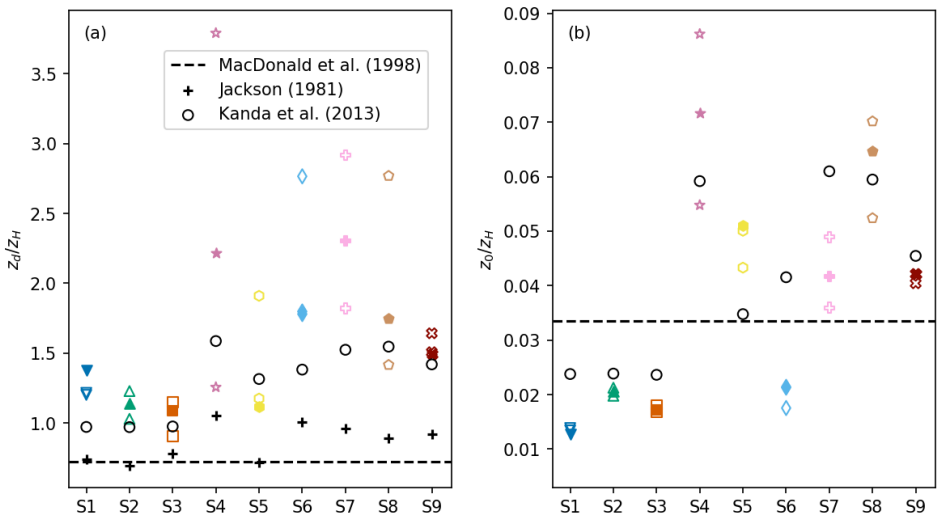

Figure 4.5: Estimations for aerodynamic roughness parameters for S1–S9 from the LES data. Estimations are from three different fitting ranges (markers, the 'mid range' fitting range values are shown as filled markers) and using the Jackson (1981) hypothesis (plus-markers) for estimating z_d. Values from the MacDonald et al. (1998) parameterization (dashed line) and Kanda et al. (2013) parameterization (circles) are shown for comparison.

uncertainty in estimates for z_0 and z_d.

The MacDonald et al. parameterizations depend only on the parameters plan area index λ_p, frontal area index λ_f and average building height z_H, and the normalised quantities z_d/z_H and z_0/z_H therefore map to a single value for all simulations. Kanda et al. additionally consider the parameters maximum building height $z_{\max}$ and standard height deviation σ_H, which yields different values of z_d/z_H and z_0/z_H for each simulation. The two paramteterizations are further discussed in Section 6.1. The range of values using these parameterization does not encompass all values estimated from the data fit. Particularly the displacement heights of simulations with faster friction velocities are underestimated by these parameterizations. The lower displacement height of MacDonald et al. (1998) is related to the fact that no building effects above the average building height are considered. The lower displacement heights from Kanda et al. may be partly explained by their usage of a lower fitting range ($[z_{\max} + 0.2z_H, z_{\max} + z_H]$) for estimating the log-law parameters, which generally results in lower displacement heights.

4.3.3 Scaling of roughness parameters

The average building height z_H is usually taken as the scaling length for the roughness parameters (MacDonald et al. 1998 and other parameterizations, see citations in Kent et al. 2017); however also $z_{\max}$ and σ_H are suggested to be important indicators for roughness parameters in the logarithmic law (Millward-Hopkins et al. 2012; Kanda et al. 2013; Kent et al. 2017). In the following, we investigate potential scaling parameters, and more generally the effects of building morphology on aerodynamic roughness. This is achieved by correlating the urban morphology statistics from Table 3.1 in Chapter 3 to z_d, z_0 and the friction factor $c_f = 2\tau_0/U^2$ as a non-dimensional and velocity-independent representation of friction. The values of z_d and z_0 are taken from the mid-range fitting region $[3z_{\max}, 3z_{\max} + 2z_H]$. It should be noted that our aim is to elicit which parameters correlate strongly with c_f, z_d and z_0, not to provide improved parameterizations of these quantities, since these would require a much larger dataset.

Figure 4.6 shows the correlations of a linear regression between the roughness parameters c_f, z_d and z_0 and average height z_H, maximum height $z_{\max}$, and $z_H, z_{\max}$ combined with the standard deviation of heights σ_H. Perhaps the most striking aspect of this figure is that the average building height z_H correlates very weakly with c_f, z_d and z_0 (Figure 4.6a–c). The weighted average heights $z_{H,f}$ and $z_{H,p}$ also show no significant correlation, with the exception of $z_{H,f}$ correlating to z_d (Figure 4.7a–f). This finding is consistent with Hagishima et al. (2009), Millward-Hopkins et al. (2011), Zaki et al. (2011) and Kanda et al. (2013). Furthermore, the maximum height $z_{\max}$ correlates strongly with both the friction factor and the displacement height (Figure 4.6d–f), as the only parameter from the morphology statistics in Table 3.1. Higher correlations are obtained for combining parameters to a multiple linear regression. Both average height z_H combined with the building-height standard deviation σ_H (Figure 4.6g–i), and the maximum height $z_{\max}$ combined with height deviation σ_H (Figure 4.6j–l) show strong correlations for c_f, z_d and z_0.

In agreement with Kanda et al. (2013), we conclude that $z_{\max}$ is more likely to be the relevant scaling length for z_d. The maximum height shows a better correlation than the average height parameters z_H and $z_{H,p}$ (only

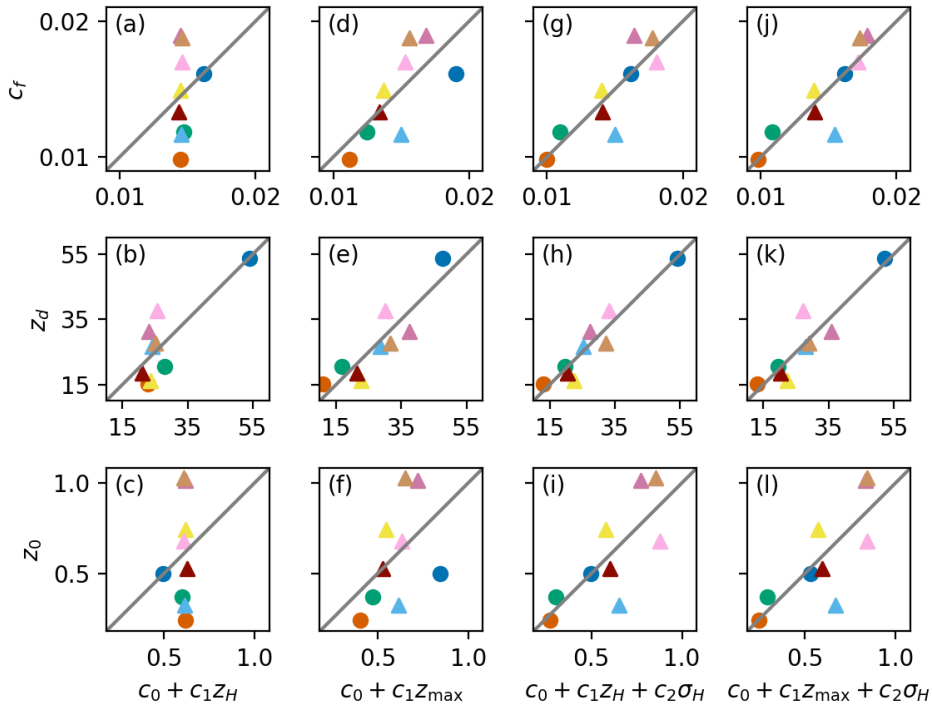

Figure 4.6: Correlations between urban morphology and log-law parameters of S1–S9 part 1. The vertical axes show the log-law parameters of friction factor c_f (a, d, g, j), displacement height z_d (b, e, h, k) and roughness length z_0 (c, f, i, l). On the horizontal axes are the urban morphology parameters with the respective best fit coefficients c_n. Note that the coefficients differ for each of the subplots. Uniform height simulations S1–S3 are shown with circles, non-uniform S4–S9 with triangles.

the frontal-area weighted average height $z_{H,f}$ has a comparable correlation to the displacement height), and also correlates for c_f and z_0, which is not the case for the average heights. The height structure of buildings clearly affects roughness parameters, which suggests that $z_{\max}$ and σ_H are important indicators for the length scale of surface variation.

4.4 Vertical transport

Figure 4.8 shows the vertical momentum fluxes $\tau(z)$, which have all different slopes due to the difference in the pressure-gradient forcings (recall that the volume flux was prescribed). The integral effect of drag is given

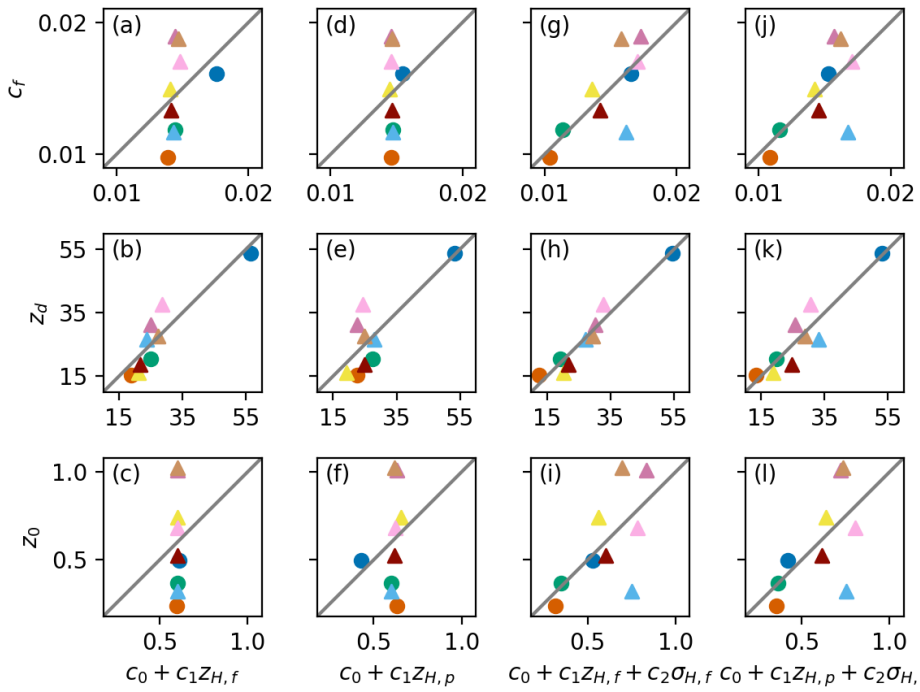

Figure 4.7: Correlations between urban morphology and log-law parameters of S1–S9 part 2. The vertical axes show the log-law parameters of friction factor c_f (a, d, g, j), displacement height z_d (b, e, h, k) and roughness length z_0 (c, f, i, l). On the horizontal axes are the urban morphology parameters with the respective best fit coefficients c_n. Note that the coefficients differ for each of the subplots. Uniform height simulations S1–S3 are shown with circles, non-uniform S4–S9 with triangles.

by the different kinematic surface stresses τ_0, which vary greatly between the simulations. From simulation S3 with the lowest canopy drag to simulation S4 with the highest canopy drag, the surface stress roughly doubles. This once more highlights that the interaction of urban morphology and the atmospheric boundary layer is not determined solely by the plan- and frontal-area indices.

Several physical processes in urban environments initiate vertical momentum transport. Mixing from turbulent eddies is the main contribution to the vertical momentum transport, although dispersive momentum fluxes, which represent the effects of spatial inhomogeneity of the mean flow, also play a role in the roughness sublayer and canopy layer. Figure 4.9 illustrates

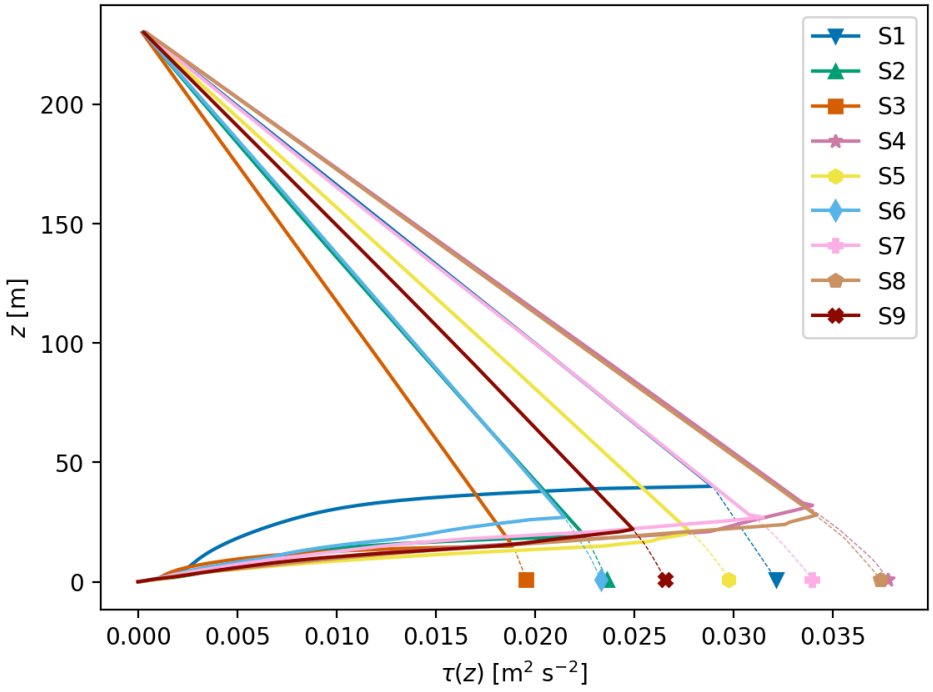

Figure 4.8: Vertical fluxes of horizontal momentum τ (solid lines), stress profiles τ_F (dotted lines), and kinematic surface stresses τ_0 (markers) of simulations S1–S9.

these vertical flux profiles for the simulations. The profiles are taken from 80,000 s (100,000 s for S3) averages. In the simulations S1–S9, both turbulent and total momentum fluxes reach their maximum at the top of the urban canopies. The overall contribution of dispersive momentum fluxes is about 5% of the total momentum fluxes. Subgrid momentum fluxes, which represent unresolved momentum fluxes in regions of high shear, contribute a maximum of 1% of the total momentum fluxes and are only present at heights with large horizontal surfaces (i.e. the ground and building tops).

Locally, dispersive fluxes are significant and can make up to 50% of the total fluxes at some heights within the canopy. Except for S1, all dispersive fluxes peak within the canopy layer. Above the canopy, the dispersive fluxes quickly reduce and turbulent fluxes become dominant. Non-zero dispersive fluxes range up to 2–6 times the maximum building height, suggesting a roughness sublayer up to these heights. For uniform building heights (S1–S3) the RSL does not extend further than three building heights. The shape of the dispersive flux varies with the building layout. In simulations

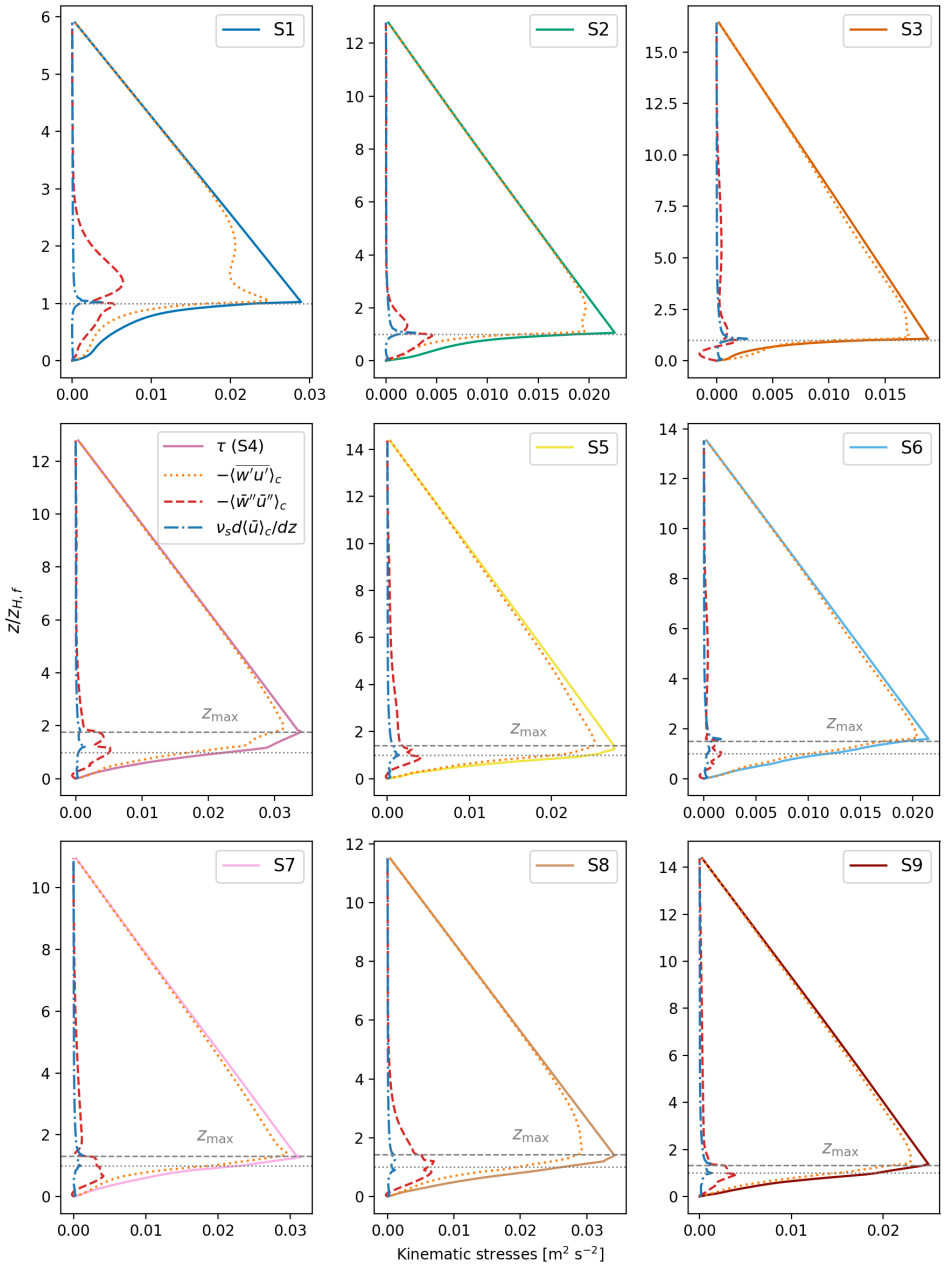

Figure 4.9: Stress profiles of simulations S1–S9. The profiles are: total momentum (solid lines), turbulent (dotted), dispersive (dashed) and subgrid-scale (dashed dotted) stresses. The mean building height $z_{H,f}$ (dotted grey) and maximum building height (dashed grey) are indicated as horizontal lines.

with uniform building heights (S1–S3), the dispersive downward momentum transport increases continuously with height up until the canopy top. Heterogeneous building heights (S4–S9) show more variation in the dispersive transport, due to several height levels where the flow is displaced above the building tops and decelerates. Dispersive fluxes within the urban canopies are larger for heterogeneous simulations with larger total canopy drag (S4, S7, S8). The downward dispersive momentum transport peaks typically below the canopy top, and often around the frontal area weighted average height. Some simulations have re-circulation zones with strong flows in the opposite direction to the driving flow near the bottom surface, so that the dispersive fluxes change sign.

4.5 Drag parameterization

The cumulative drag function $\tau_D(z)$ describes the accumulation of building drag in the urban canopy layer towards the ground. Figure 4.10a shows the cumulative drag profiles of all simulations S1–S9. The profiles vary strongly for each of the simulations with no apparent trend. The drag increases quickly at the top of the buildings, which is evident from the profiles of simulations S1–S3. We may further assume that the buildings' surface area higher up contributes more drag, due to the generally higher wind velocities at higher altitudes. In order to measure the effects of the wind-facing building surfaces relative to a reference level, a descriptor of the vertical structure of the building layouts is needed, which will be a generalised version of the frontal area index λ_f.

Let $L(z)$ be the buildings' total width at height z, which is the distribution of the wind-facing surface area of the buildings with height. The buildings' total frontal area is then given by

$$A_F = \int_0^h L(z)\,\mathrm{d}z \tag{4.7}$$

and the frontal area index is therefore

$$\lambda_f = \frac{1}{A_T}\int_0^h L(z)\,\mathrm{d}z. \tag{4.8}$$

In the simulations S1–S9, the wind orientation and the buildings are aligned with the x-axis. The total width is $L(z) = \sum_n B_{w,n}(z)$, where $B_{w,n}(z)$

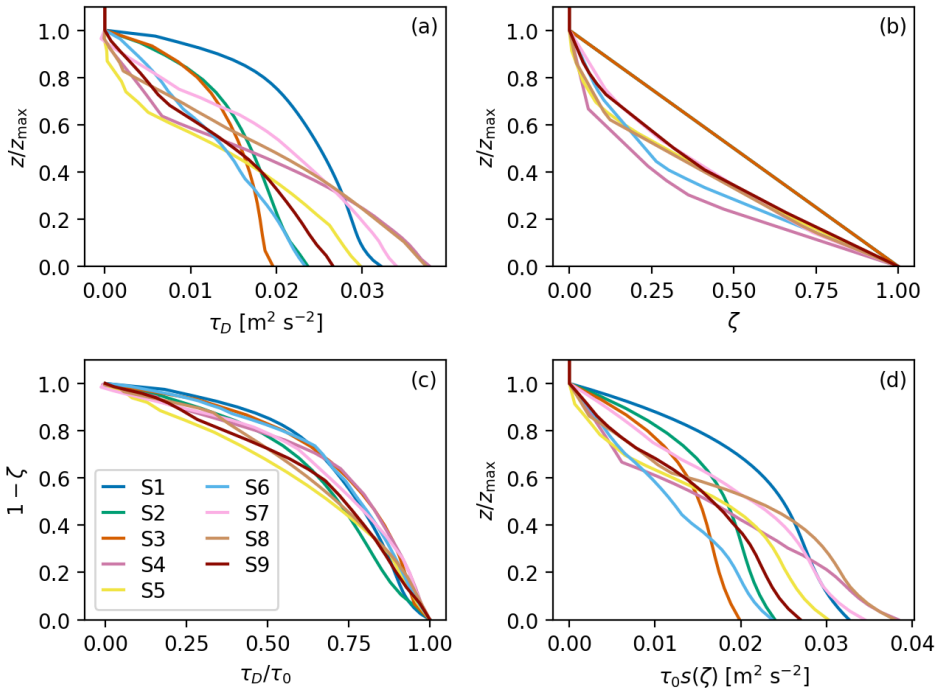

Figure 4.10: Cumulative drag functions of S1–S9 and their parameterizations. (a) cumulative drag $\tau_D(z)$, (b) normalised frontal area function $\zeta(z)$, (c) correlation between these, and (d) estimated cumulative drag $\tau_0\, s(\zeta(z))$.

denotes the width of building $\mathcal{B}_n$ at height z, which is constant with height and zero above the building height. A detailed discussion of $L(z)$ is given in Chapter 5.

The (dimensionless) normalised frontal area

$$\zeta(z) = \frac{1}{A_F} \int_z^h L(z')\, \mathrm{d}z' \tag{4.9}$$

shown in Figure 4.10b can be used to serve as an alternative height representation of the buildings where $\zeta = 0$ represents the top of the buildings and $\zeta = 1$ represents ground level. The normalised frontal area describes the fraction of the total frontal area above height z. Because the height coordinate is scaled as $z/z_{\max}$, the ζ-profiles of layouts S1–S3 with uniform building-heights overlap to a linear function with constant slope. Morphologies with non-uniform building heights have piecewise linear functions $\zeta(z)$.

The LES data reveal a strong relationship between the cumulative drag and the vertical building structure, represented by $\zeta(z)$. Figure 4.10c shows

that plotting $\tau_D(z)/\tau_0$ as a function of $1-\zeta(z)$ (which is 0 at the ground and 1 at the top of the buildings) results in a collapse of the data. The collapsed data can be fitted reasonably well using a single third-order polynomial of the form

$$s(\zeta) = C_1\zeta^3 + C_2\zeta^2 + (1 - C_1 - C_2)\zeta \tag{4.10}$$

with $C_1 = 1.88$ and $C_2 = -3.89$. The polynomial function s describes the height-dependent contribution to the drag relative to the morphology ζ. While the values of C_1 and C_2 represent the best fit for the particular set of λ_p, λ_f in this study, the fact that the drag distribution function s is not a linear function of ζ confirms the physical intuition that the tallest buildings impose a disproportionally large amount of drag on the flow. The larger contribution of taller buildings is consistent with previous findings (Xie et al. 2008). Testing the polynomial regression with different degrees shows that the three-degree polynomial captures sufficiently well the vertical shape of $\tau_D(z)$, and increasing the degree of the polynomial does not result in significantly more accurate approximations.

Equation 4.10 enables direct evaluation of the cumulative canopy-drag profile

$$\tau_D(z) = \tau_0\, s(\zeta(z)), \tag{4.11}$$

provided that the net total canopy drag τ_0 is known. Figure 4.10 shows the estimated profiles in (d), which closely resemble the data in (a), demonstrating that the distribution of the urban canopy drag can be reconstructed using only the building layout and an estimation for the total canopy drag.

By differentiating (4.11), the volumetric drag term can be determined as

$$f_D(z) = -\frac{\mathrm{d}\tau_D}{\mathrm{d}z}(z) = -\tau_0 \frac{\mathrm{d}s}{\mathrm{d}\zeta}\frac{\mathrm{d}\zeta}{\mathrm{d}z}(z) = \tau_0 \frac{L(z)}{A_F}\frac{\mathrm{d}s}{\mathrm{d}\zeta}(\zeta(z)). \tag{4.12}$$

The term $L(z)/A_F$ is the fraction of the frontal area at height z to the total frontal area, which expresses that the wind-facing area of the buildings play a key role in the production of drag. The weighting by $\mathrm{d}s/\,\mathrm{d}\zeta$, which is a nonlinear function of the building layout $\zeta(z)$, represents that the production of drag is not necessarily constant across the urban canopy. The volumetric drag force in (4.12) is suitable to parameterise the momentum sink of buildings by adding it as a forcing term to the governing momentum equations of a model that does not explicitly resolve the flow around buildings.

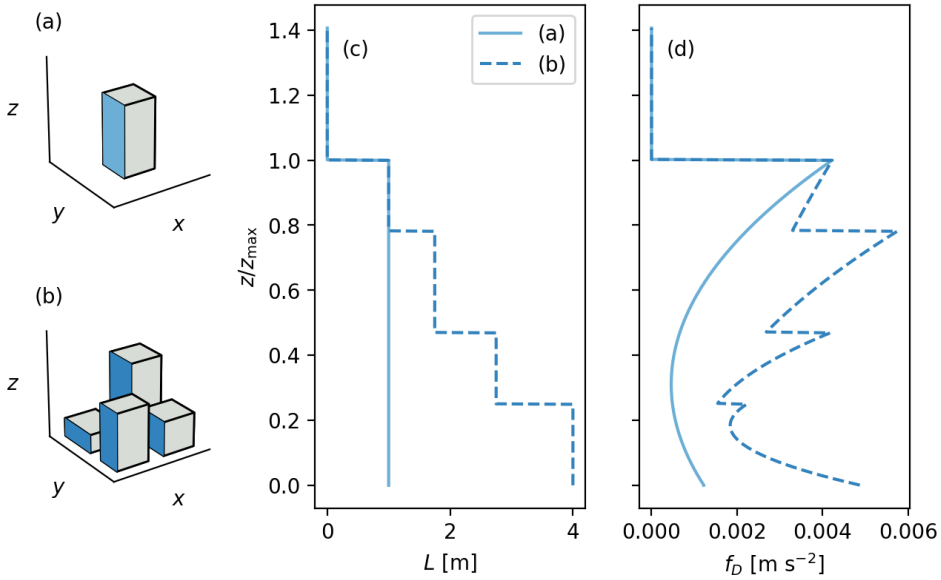

Figure 4.11: Illustration of the derived relation between building geometry and volumetric drag. Geometries of a single building (a, solid line) and several heterogeneous buildings (b, dashed line) with corresponding (c) building width L and (d) volumetric drag f_D.

Figure 4.11 shows two generic examples, one of a single uniform building and one of several heterogeneous building forms, which illustrate the drag distribution throughout the canopy given by Equation 4.12. Because the cumulative drag has been fitted with a cubic polynomial function, the volumetric drag profile is quadratic in shape. For a single building, the volumetric drag initially decreases above the ground, then increases nonlinearly towards the top of the building, where most drag is produced. The volumetric drag for multiple buildings with heterogeneous shapes and heights combines the drag of individual buildings in a nonlinear way, with spikes in volumetric drag clearly indicating each building top.

Equation 4.12 generalises the canopy drag model for uniform buildings of Coceal and Belcher (2004) and Belcher (2005). Based on the pressure force on a single building, the authors derive a volumetric drag force

$$\rho_0 f_D(z) = \frac{1}{2}\rho_0 c_D U^2 \lambda_f \frac{1}{z_H}, \tag{4.13}$$

where c_D is a drag coefficient. Note that for consistency with the definition

of volumetric drag (Equation 2.20) in Chapter 2, (4.13) is not divided by the fluid area as in the original model. N uniform buildings with heights z_H yield a constant total width function $L(z) = NB_w$ below z_H and total frontal area $A_F = NB_w z_H$, which implies that $L(z)/A_F = 1/z_H$ for $z \leq z_H$. Belcher (2005) assumes constant canopy drag, in which case $s(\zeta) = \zeta$ and hence $\mathrm{d}s/\,\mathrm{d}\zeta = 1$. The volumetric drag $f_D(z) = \tau_0/z_H$ with total (kinematic) urban canopy drag

$$\tau_0 = \frac{1}{2} c_D U^2 \lambda_f \tag{4.14}$$

is therefore equivalent to Equation 4.12 with uniform buildings and constant canopy drag.

4.6 Discussion

The heterogeneity of an urban site was shown to strongly influence the vertical structure of mean flow and dispersive vertical momentum transport. At equal average wind velocity, the total surface drag varies as much as almost a factor two between a uniform and strongly heterogeneous morphology. Regression analysis showed that the variations are correlated to the height structure of buildings, particularly to the maximum building height $z_{\max}$ and height variation σ_H, rather than averaged height z_H.

Developing parameterizations for heterogeneous building morphologies based on the logarithmic wind profile is challenging. First, even with a detailed velocity height-profile and known friction velocity, there are intrinsic uncertainties in estimating the displacement height z_d and roughness length z_0. Second, our results indicate that current well-known parameterizations of the log law such as MacDonald et al. (1998) and Kanda et al. (2013) cannot sufficiently capture the large spread of roughness-parameter values, even with additional building statistics such as the maximum height $z_{\max}$ and height variation σ_H.

These findings suggest that a model of urban areas based on logarithmic velocity profiles and where the momentum sink is modelled at a single point, that is as a boundary condition to the wind velocities at ground level, is ill-suited to represent the range of flow behaviour from heterogeneous urban morphologies.

An exploration of the vertical structure of the canopy drag revealed that at first sight, there is very little that the different simulations have in common. However, the normalised frontal area, which encapsulates the height-distribution of the surface area, was shown to be able to roughly collapse all distributed stress profiles on a single curve. This paved the way to a parameterization of the drag distribution via a third-order polynomial (Equation 4.10). Importantly, this relationship is not linear and the top of the urban canopy, i.e. the highest building in the morphology, produces significantly more drag than the buildings below. Contrary to the standard modelling approach, this parameterization considers the vertical structure of the heterogeneous morphologies and models the momentum sink distributed over the height of the urban canopy.

In the following chapters we will explore the potential of the distributed drag parameterization by adopting the scheme for a city-scale numerical weather prediction model. We will use the London Model, which is a high-resolution version of the Met Office Unified Model over Greater London and surrounding regions. For this purpose, we need a generalisation of the normalised frontal area function, which takes different wind directions and more complex building geometries into account, which is derived in the following chapter. The distributed drag model relies on the total canopy drag as an input parameter, for which we will use the Coceal and Belcher model in Equation 4.14.

5

Characterising the urban morphology of Greater London

This chapter describes the analysis of the urban morphology of Greater London and its surroundings from Ordnance Survey data of all the individual buildings in this area. This was necessary for the study of the distributed drag parameterization (Section 4.5) in the context of the London Model, a high-resolution regional numerical weather prediction model from the Met Office, which will be discussed in more detail in Section 7.1.1. The default urban morphology input parameters of the London Model are the mean building height z_H, plan area index λ_p, and frontal area index λ_f. These parameters provide insufficient information to be able to use the distributed drag parameterization, which requires the vertical morphology profiles $\zeta(z)$ as input parameter for each grid box. Hence the morphology profiles $\zeta(z)$ are calculated and for consistency, the default urban morphology input parameters are also updated. First, a generalisation of the buildings' total width function $L(z)$, upon which $\zeta(z)$ profiles are based, is introduced (Section 5.1). The buildings' total width $L(z)$ describes the height-distribution of the wind-facing surface area of buildings, uniformly averaged over all wind

directions. Section 5.2 outlines the calculation of the urban morphology parameters and vertical morphology profiles for the London Model domain. Once $L(z)$ and $\zeta(z)$ are calculated for each grid box, an analysis is conducted to parameterise $\zeta(z)$ based on the ratio of the maximum to mean building height $r = z_{\max}/z_H$ (Section 5.3). The great advantage of this approach, apart from the insight it gives about the morphology in London, is that the only additional input to the London Model is the maximum building height $z_{\max}$. A few general remarks on the findings of this chapter are made in Section 5.4.

5.1 Vertical urban morphology profiles

The frontal area of a solid object is commonly used in describing the drag force with respect to the surrounding fluid. A height-distributed frontal area index for buildings, which is based on height increments of the frontal area, has previously been proposed for the vertical representation of buildings (Di Sabatino et al. 2008, 2010; Millward-Hopkins et al. 2012). This section provides a formal definition and practical computation method for the width of a building at any height, which corresponds to the height increments of the building's frontal area. A height-dependent building width function and height-dependent profiles describing the full urban morphology are deduced afterwards.

5.1.1 Width of a building cross-section

Consider the two-dimensional, horizontal building cross-section B at a fixed height. This is the set containing all elements that constitute the building (grey shaded area in Figure 5.1). Let $\mathbf{e}_\theta = (\cos\theta, \sin\theta)$ be the unit wind vector for a wind angle θ and $\mathbf{e}_{\perp\theta} = (\sin\theta, -\cos\theta)$ a unit vector perpendicular to it. The building width $b(B, \theta)$ (in direction $\mathbf{e}_{\perp\theta}$) is defined as the distance between two lines parallel to $\mathbf{e}_\theta$, such that B is entirely between these two lines (Moszynska 2006).

This definition is equivalent to projecting the building cross-section onto a vector perpendicular to $\mathbf{e}_\theta$, and calculating the length of the projected cross-section. For the calculation of the building width it is sufficient to consider a small subset of B. The building cross-section is enclosed by a

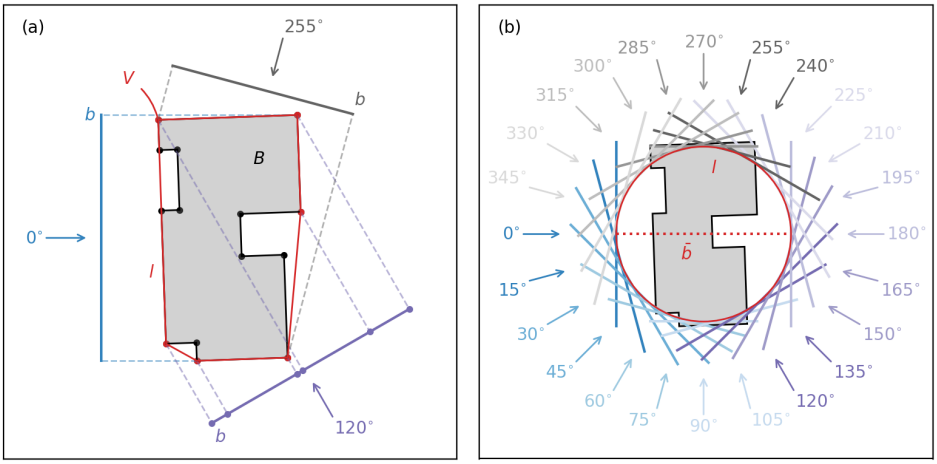

Figure 5.1: The width $b(B, \theta)$ of a building cross-section B. (a) Building widths $b(B, \theta)$ for wind angles $\theta = 0°, 120°$, and $255°$; vertices V (red dots) describing the minimal convex polygon that encloses B (red polygon) and has perimeter $l(V)$. (b) Building mean width $\bar{b}(B)$ (red dotted line) and circle with perimeter $l(V)$ (red circle).

unique minimal convex polygon (i.e. the boundary of the convex hull of B; red polygon in Figure 5.1a) with vertices V (red dots in Figure 5.1a). These vertices V are a subset of the building corners that describe the shape of B (red and black dots in Figure 5.1a), and they are the only elements of B that are needed for calculating $b(B, \theta)$. Projecting the building vertices in V onto $\mathbf{e}_{\perp\theta}$ and calculating the distance between the two outermost projected vertices may be written as:

$$b(B, \theta) = \max\left(\|Q\mathbf{x} - Q\mathbf{y}\| : \mathbf{x}, \mathbf{y} \in V\right), \tag{5.1}$$

with the projection matrix

$$Q = \mathbf{e}_{\perp\theta}{\mathbf{e}_{\perp\theta}}^T = \begin{pmatrix} (\sin\theta)^2 & -\sin\theta\cos\theta \\ -\sin\theta\cos\theta & (\cos\theta)^2 \end{pmatrix}. \tag{5.2}$$

Figure 5.1a shows building widths of a building cross-section for several wind angles and illustrates the projection of vertices from V.

In realistic scenarios the wind angle varies frequently, for which it is useful to consider the average width with respect to all wind directions.

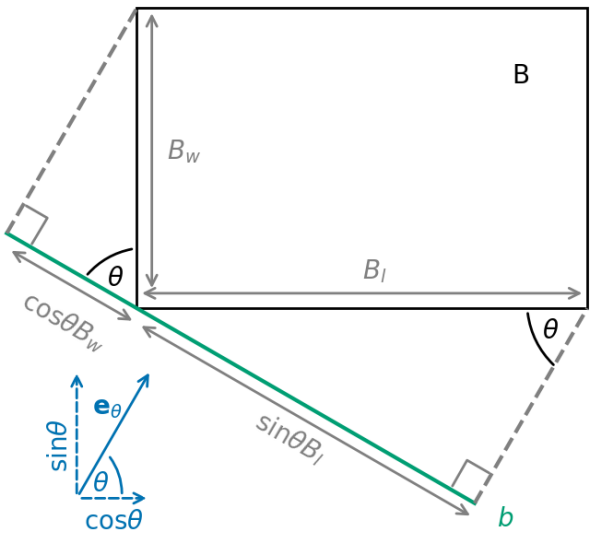

Figure 5.2: Building width $b(B, \theta)$ for a rectangular building cross-section.

The building's mean width $\bar{b}(B)$ is given by (Moszynska 2006)

$$\bar{b}(B) \equiv \frac{1}{2\pi} \int_0^{2\pi} b(B, \theta)\ \mathrm{d}\theta = \frac{l(V)}{\pi}, \tag{5.3}$$

where $l(V)$ is the perimeter of the convex polygon described by V. This relation states that the mean width is equivalent to the diameter of a circle with the same perimeter as the minimal convex polygon enclosing B (cf. $l(V)$ in Figure 5.1a and b).

5.1.2 Example: rectangular buildings

An intuitive example of the building width is presented for a rectangular building with width B_w and length B_l (see Figure 5.2). The building cross-section of a rectangular building is a convex set and therefore equal to its convex hull, which implies that V consists of the four building corners. To calculate the building width, we first note that for any $\mathbf{x} = (x_1, x_2)$, $\mathbf{y} = (y_1, y_2)$:

$$\|Q\mathbf{x} - Q\mathbf{y}\| = |\sin\theta(x_1 - y_1) - \cos\theta(x_2 - y_2)|, \tag{5.4}$$

which is shown in Appendix B. For simplicity, let us assume that the four building corners are given by $(0,0)$, $(B_l,0)$, (B_l,B_w), and $(0,B_w)$. There are six possible combinations of building corners for $\|Q\mathbf{x}-Q\mathbf{y}\|$, which may give the maximum projected length, depending on the wind angle θ: $|\sin\theta B_l|$, $|\sin\theta B_l-\cos\theta B_w|$, $|\cos\theta B_w|$, $|-\cos\theta B_w|$, $|-\sin\theta B_l-\cos\theta B_w|$, and $|-\sin\theta B_l|$. We can write this as

$$\max\left(\|Q\mathbf{x}-Q\mathbf{y}\|\right)=|\sin\theta|B_l+|\cos\theta|B_w. \tag{5.5}$$

The building's mean width is thus given by

$$b(B,\theta)=|\sin\theta|B_l+|\cos\theta|B_w, \tag{5.6}$$

which may equally be derived using trigonometric identities (on the right triangles indicated in Figure 5.2).

Averaging over all wind directions yields:

$$\begin{aligned}\bar{b}(B)&=\frac{1}{2\pi}\int_0^{2\pi}\left(|\sin\theta|B_l+|\cos\theta|B_w\right)\ \mathrm{d}\theta &(5.7)\\ &=\frac{2}{\pi}\int_0^{\pi/2}\left(\sin\theta B_l+\cos\theta B_w\right)\ \mathrm{d}\theta &(5.8)\\ &=\frac{2}{\pi}\left[-\cos\theta B_l+\sin\theta B_w\right]\Big|_0^{\pi/2} &(5.9)\\ &=\frac{2}{\pi}(B_l+B_w). &(5.10)\end{aligned}$$

The mean width may also be directly derived from the relation in Equation 5.3: the perimeter of the rectangular building is $l(V)=2(B_l+B_w)$ and we obtain the mean width $\bar{b}(B)=2(B_l+B_w)/\pi$.

5.1.3 Vertical building-width function

The shape of the building cross-section B may change with height. We will informally denote this by $B(z)$, such that we can express height-dependent functions of building width $b(B(z),\theta)$ and building mean width $\bar{b}(B(z))$. The frontal area A_f of a building for wind angle θ is derived by height-integration of the building width,

$$A_f(\theta)=\int_0^h b(B(z),\theta)\ \mathrm{d}z, \tag{5.11}$$

which is consistent with the typical definition of a frontal area (e.g., Grimmond and Oke 1999).

The calculation of the building mean width is computationally inexpensive and straightforward with Equation 5.3 and it is therefore useful as a basis for calculating vertical profiles and morphology parameters over urban areas; in this case for the grid boxes of the NWP model. For a grid box with buildings described by the vertical building cross-section profiles $B_n(z)$, we define the buildings' total (mean) width at height z as

$$L(z) = \sum_n g_n \bar{b}(B_n(z)), \tag{5.12}$$

where g_n is a weighting equal to the fraction of building area within the grid box to account for buildings that are only partially contained within it. The total frontal area A_F (note the capital subscript $_F$, as compared to A_f for a single building) is then defined as a wind-directional averaged total frontal area, and A_F is thus given by integrating the total width with respect to height

$$A_F = \int_0^h L(z)\ \mathrm{d}z. \tag{5.13}$$

This definition is consistent with the classical description (Section 1.3) as the sum of all the buildings' frontal areas:

$$\begin{aligned} A_F &= \sum_n A_{f,n} = \sum_n \int_0^h \bar{b}(B_n(z))\ \mathrm{d}z = \int_0^h \sum_n \bar{b}(B_n(z))\ \mathrm{d}z \\ &= \int_0^h L(z)\ \mathrm{d}z. \end{aligned} \tag{5.14}$$

We have assumed that all buildings are fully contained within the grid-box (i.e. $g_n = 1$). Note that by summing up the building-width contributions of each building in the grid box in (5.12), we do not account for reduced wind-facing surfaces from buildings next to one another or sheltering effects from buildings in close proximity. Frontal areas A_F calculated by this method will therefore tend to be larger than frontal areas calculated by methods that project all building fronts onto one plane and determine A_F as the area of this projection. The (dimensionless) normalised frontal area function can now be formally defined as (note that this definition is the same as the ad hoc formulation for cuboid buildings in Equation 4.9)

$$\zeta(z) = \frac{\int_z^h L(z')\ \mathrm{d}z'}{\int_0^h L(z')\ \mathrm{d}z'} = \frac{1}{A_F} \int_z^h L(z')\ \mathrm{d}z'. \tag{5.15}$$

5.2 Urban morphology of Greater London

5.2.1 Ordnance Survey building data

Urban morphology datasets for the London Model domain are derived for this study using the Ordnance Survey MasterMap Topography Layer – Building Height Attribute data at 1 m resolution, updated in April 2019 (Ordnance Survey (GB) 2019a). The data are given in the British National Grid reference system. The analysed region covers approximately 125 × 140 km^2 from Lat 51°, Lon -1.15° to Lat 52.25°, Lon 0.78° (455000, 120000 to 590000, 265000 on the British National Grid) and extends over the Greater London area and its surroundings. The data coverage is shown in Figure 5.3 and the extent of the domain is indicated by the red box. The London Model domain contains approximately 9.4 million buildings. Data for around 5 % of the domain area are missing, all of which are outside Greater London (note the blank spaces in Figure 5.3). For these regions the original London Model input data are used.

A building in the OS MasterMap Topography Layer is represented by a polygon defining the footprint of the building and attributed with two heights: the maximum height z_m and the principal height z_p (Ordnance Survey (GB) 2017). The maximum height represents the highest point of the building extracted from the Digital Surface Model, relative to the height datum. It could represent any structure that is of sufficient size to be captured in the Digital Surface Model and may include industrial chimney stacks and any structures that may be present on top of the building. Chimneys on residential buildings are excluded from this measurement. The principal height captures the height of the main structure of the building excluding the roof. In buildings with multiple heights, for example a main two-storey building with a smaller single-storey extension, the principal height is calculated from the larger area, i.e. the two-storey part. Figure 5.4 illustrates examples of the two building heights in a residential (a) and an industrial building (b).

We approximate the three-dimensional building shape by assuming a building area equal to the building footprint below z_p, and a pyramid-shaped roof between z_p and z_m (cf. Algorithm 5.1). The building cross-section de-

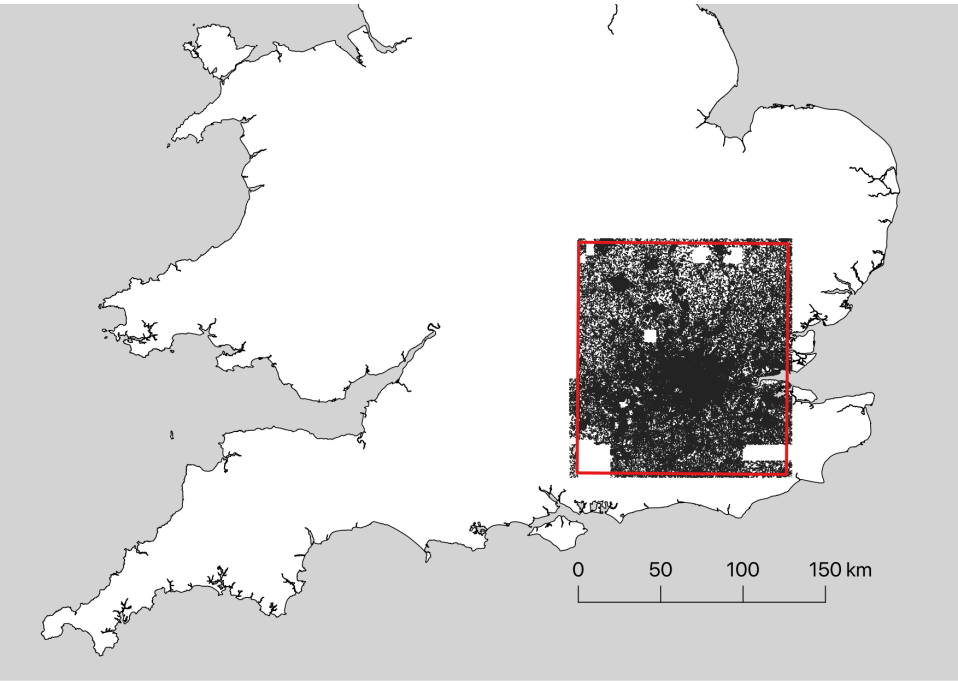

Figure 5.3: Coverage of OS building data (Ordnance Survey (GB) 2019a) and London Model domain (red). Great Britain contour data from OS OpenData (Ordnance Survey (GB) 2005).

creases by a constant factor from the principal to the maximum building height, and the slope of the roof is therefore dependent on the height difference between these two parameters. Figure 5.4 (c) and (d) illustrate these geometry assumptions for the residential and industrial building examples.

5.2.2 Urban morphology calculations

For the calculation of the model urban morphologies, the domain was split into the 420 × 380 (159,600) grid boxes of the London Model. The grid spacing is 0.003 degrees of longitude and latitude on a rotated pole grid, which has its North pole at Lat 37.5°, Lon 177.5°. As such, the model equator, where the grid is most square, goes through the centre of the UK. Due to the relatively small domain of the London Model, the corresponding grid spacing on the British National Grid is approximately constant and we used a spacing of $\Delta x = 334.5$ m and $\Delta y = 333.7$ m.

The following quantities were calculated for each grid box: the mean

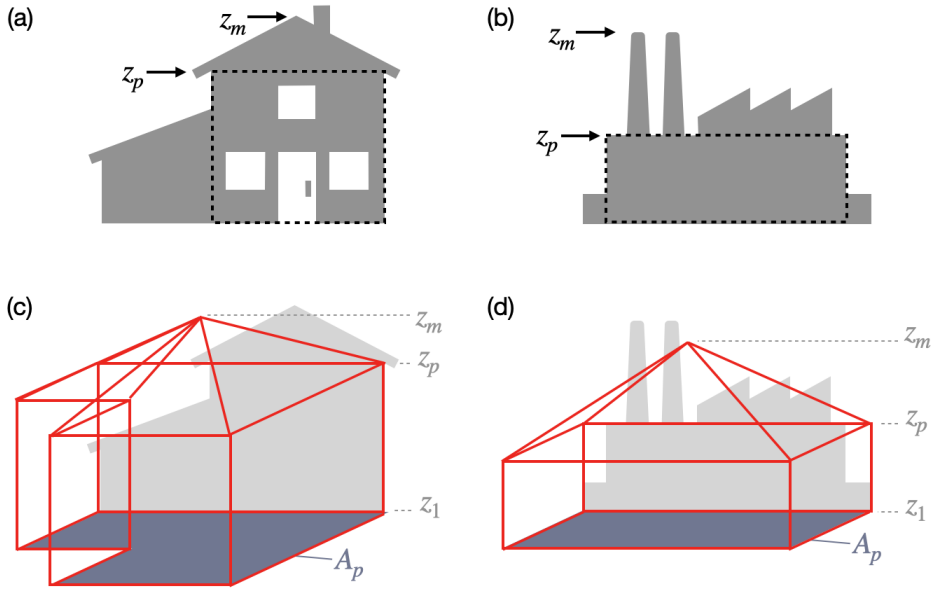

Figure 5.4: Building representation for OS building data. Principal z_p and maximum z_m heights and the principal part of a building (dashed black lines) for a residential (a) and industrial (b) building. Building footprint A_p and three-dimensional representation (red contours) of the residential (c) and industrial (d) building. The ground level is indicated by z_1.

width function $L(z)$, the plan area index λ_p, the frontal area index λ_f, the mean building height z_H, and the maximum building height $z_{\max}$. The mean width $L(z)$ was defined in (5.12). The grid box frontal area index is given by

$$\lambda_f = \frac{A_F}{A_T} = \frac{1}{A_T}\int_0^h L(z')\,\mathrm{d}z', \tag{5.16}$$

following the definition of the total frontal area A_F by (5.13) and a grid-box plan area of $A_T = \Delta x \Delta y$. The plan area index is calculated in the usual way by $\lambda_p = A_P/A_T$, where $A_P = \sum_n g_n A_{p,n}$ and $A_{p,n}$ are the buildings' plan areas. We define the mean building height of the grid box as

$$z_H = \frac{A_F}{L(0)}. \tag{5.17}$$

This quantity resembles a weighted average (cf. definition in Equation 1.3), where each building height $B_{h,n}$ is weighted by the building's mean width

Algorithm 5.1 Calculation of the normalised height-profile $S(z)$ of a pyramid-shaped building.

function GET VERTICAL PROFILE(building)

$$S(z) = \begin{cases} 1, & z < z_p \\ \frac{z_m - z}{z_m - z_p}, & z_p \leq z < z_m \text{ and } z_p \neq z_m \\ 0, & \text{else.} \end{cases}$$

return $S(z)$

at ground level $B_{w,n} = \bar{b}(B_n(0))$:

$$\frac{A_F}{L(0)} = \sum_n g_n \frac{A_{f,n}}{L(0)} = \sum_n g_n \frac{\int_0^h \bar{b}(B_n(z))\,\mathrm{d}z}{L(0)} = \sum_n g_n \frac{\bar{b}(B_n(0))B_{h,n}}{L(0)} \tag{5.18}$$

$$= \sum_n g_n \frac{B_{w,n}}{\sum_n B_{w,n}} B_{h,n}, \tag{5.19}$$

where the weights are

$$w_n = \frac{B_{w,n}}{\sum_n B_{w,n}} \tag{5.20}$$

and $B_{h,n}$ is the building height we obtain from integrating the normalised height-profile of the building (Algorithm 5.1). For pyramid-shaped buildings with principal height z_p and maximum height z_m this is $B_h = (z_p + z_m)/2$. The maximum height of all buildings in the grid box is denoted as

$$z_{\max} = \max_n(z_{m,n}), \tag{5.21}$$

where $z_{m,n}$ are the maximum heights of the individual buildings. The grid-box maximum building height does not distinguish whether a building is partially or fully situated within the grid box.

Algorithms 5.1 and 5.2 describe the calculation of the grid-box morphology parameters and vertical profiles. The following steps were taken for each building $\mathcal{B}_n$:

1. assign to which grid box(es) the building belongs, taking into account that buildings may be part of multiple grid boxes;

2. calculate the building's mean width $\bar{b}_n$ and plan area $A_{p,n}$ from the building footprint;

Algorithm 5.2 Calculations of urban morphology parameters and profiles for given buildings and grid-box locations. Parameter definitions are given in Section 5.2.2.

function EXTRACT MORPHOLOGIES(buildings, grid boxes)
  for all grid boxes **do**
    Initialise A_P, $L(z)$, $z_{\max}$.
  for all buildings **do**
    selected grid boxes = CONTAINS BUILDING(grid boxes, building)
    $S(z)$ = GET VERTICAL PROFILE(building)
    a = GET PLAN AREA(building)
    b = GET MEAN WIDTH(building)
    for grid box **in** selected grid boxes **do**
      g = GET WEIGHTING(building, grid box)
      $A_P = A_P + ag$
      $L(z) = L(z) + bS(z)g$
      $z_{\max} = \max(z_{\max}, \text{MAX HEIGHT(building)})$
  for all grid boxes **do**
    Frontal area $A_F = \int_0^h L(z)\,\mathrm{d}z$
    Frontal area index $\lambda_f = A_F/A_T$
    Plan area index $\lambda_p = A_P/A_T$
    Mean height $z_H = A_F/L(0)$

3. determine the vertical mean width function $\bar{b}(B_n(z))$ from $\bar{b}_n$ and the three-dimensional building shape;

4. add $\bar{b}(B_n(z))$ to $L(z)$ and $A_{p,n}$ to A_P in the appropriate grid box(es);

5. where necessary update the grid-box maximum building height $z_{\max}$.

The grid-box' plan area index λ_p, frontal area index λ_f, and mean height z_H are determined in a final step, after the calculations for each building are concluded.

The resulting values for λ_p, λ_f and z_H were further compared with the original input values of the London Model grid boxes and increased to match the original values, if they were below them. (This means in particular that all values are greater than zero, as there is a minimum threshold for these parameters in the original data.) The gaps in the OS building data were

filled with the original data and the maximum height at these grid boxes is assigned a value of $z_{\max} = 2.3 z_H$. This is the average ratio of maximum to mean building height of the new data.

5.3 Parameterising London's morphology profiles

Figure 5.5 illustrates three examples of the total width $L(z)$ and the corresponding normalised frontal area $\zeta(z)$, calculated from the OS building data for some London Model grid boxes. Figure 5.5a–b are grid boxes in central London. Here, (a) contains a historical neighbourhood with $z_H =$ 21 m and $z_{\max} = 44$ m, (b) contains high-rise buildings that go well beyond the vertical axis of 100 m ($z_{\max} = 224$ m) with average height $z_H = 33$ m. Figure 5.5c shows one of the grid boxes with a uniform building height, with $z_H = 18$ m.

To reduce the complexity of the required model input, the vertical profiles $L(z)$ and $\zeta(z)$ are parameterised in terms of the mean building height z_H and maximum building height $z_{\max}$ of the grid box. It is possible to directly compare the vertical functions amongst the grid boxes by a change of variables $\hat{z} = z/z_{\max}$, such that the re-scaled and normalised $\hat{L}(\hat{z})/A_F$ functions and $\zeta(\hat{z})$ are defined on the interval $[0, 1]$. The $\hat{L}(\hat{z})/A_F$ profiles are categorised according to the ratio of the maximum to the mean building height of the corresponding grid box, $r = z_{\max}/z_H$.

The data are split into the following six bins: $r = 1$, $r \in (1, 2]$, $r \in (2, 3]$, $r \in (3, 4]$, $r \in (4, 5]$, $r > 5$. Figure 5.6 shows the spatial distribution of r for the London Model domain and the relative frequency of each bin. The first category, $r = 1$, classifies grid boxes with uniform buildings, where the maximum height is equal to the mean height. Less than 1 % of all the London Model domain grid boxes fall into this category, and they have very low building densities ($\lambda_p < 0.02$), usually with only one or two buildings inside. Approximately half of the grid boxes have a building-height ratio $r \in (1, 3]$, the remaining three categories contain the other 10 % of the grid boxes that include buildings; overall 40 % of the grid boxes do not include any buildings. The average building-height ratio is $r = 2.3$. A high r is generally associated with a large heterogeneity in building heights. For example, grid boxes with high-rise building clusters like in the London City

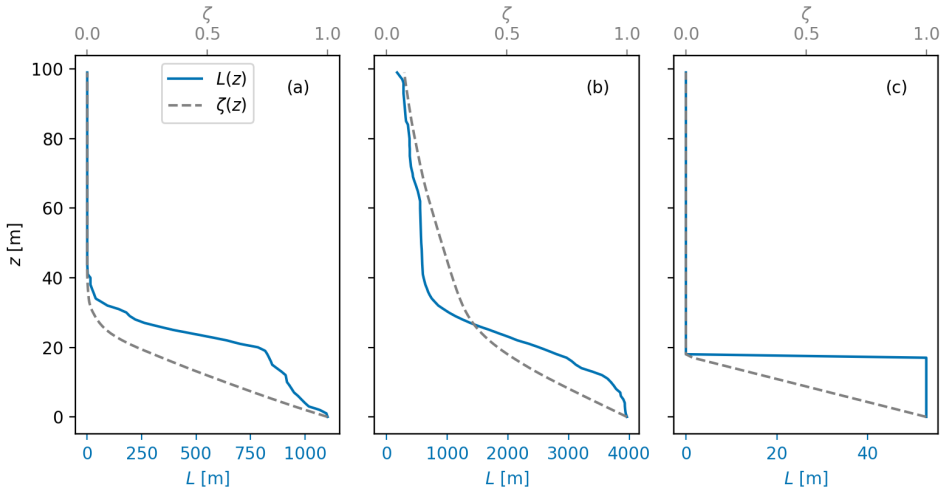

Figure 5.5: Examples of mean width $L(z)$ (solid line) and corresponding normalised frontal area $\zeta(z)$ (dashed line) for grid boxes containing (a) a historical neighbourhood, (b) high-rise buildings, and (c) buildings with equal heights. The different ranges of the two functions are indicated at the bottom and top.

area have typical ratios of 6–8. The Shard with its 304 m is the highest building in the domain. It is situated on the border of two grid boxes which have values of $r = 15$ and $r = 17$. However, also sparsely populated grid boxes with a single tall structure, e.g. a transmission tower, fall into the $r > 5$ category.

Averaging the functions $\hat{L}(\hat{z})/A_F$ for each of the bins yields six distinct profiles $\langle\hat{L}\rangle(\hat{z})/A_F$ (Figure 5.7a). The functions integrate to unity and therefore resemble a distribution function. The data fit well to an exponential distribution that is modified to be non-zero on the interval $[0, 1]$:

$$\frac{L}{A_F}(\hat{z};\alpha) = \begin{cases} \dfrac{\alpha\exp(-\alpha\hat{z})}{1-\exp(-\alpha)}, & \hat{z}\in[0,1], \\ 0, & \text{otherwise}, \end{cases} \tag{5.22}$$

with $\alpha > 0$.

Empirical values for α are derived from a curve fit of the six averaged profiles to (5.22). Afterwards these empirically fitted coefficients $\tilde{\alpha}$ are related to the building-height ratio r. The values $\tilde{r} = 1, 1.5, 2.5, 3.5, 4.5, 6$ are chosen to represent the bins. Linear regression between $\tilde{r}$ and the empirical

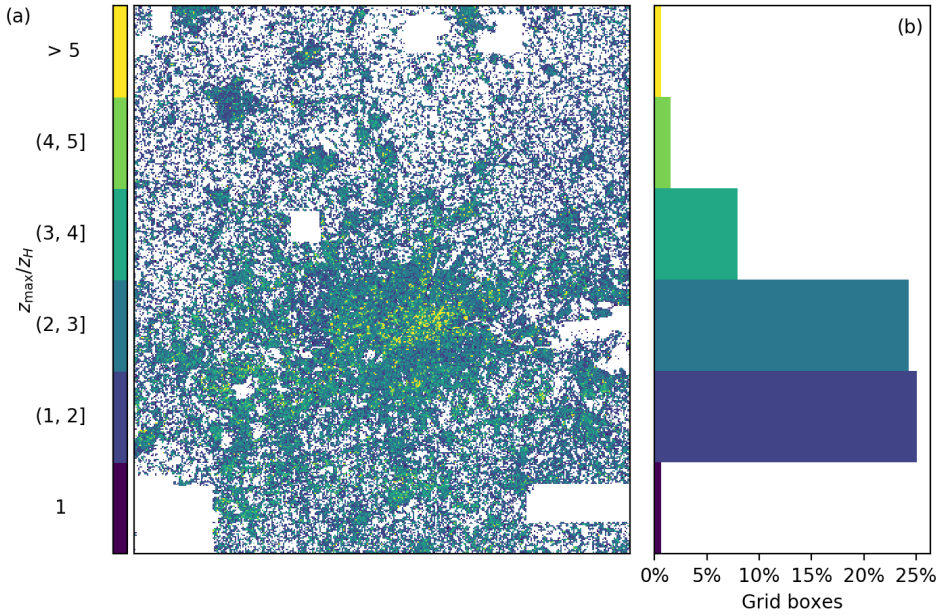

Figure 5.6: Building height ratio $r = z_{\max}/z_H$ categorised into six bins with their (a) spatial distribution and (b) relative frequency in the London Model domain.

values $\tilde{\alpha}$ gives the following approximation:

$$\alpha(r) = 1.355r - 0.7807. \tag{5.23}$$

The fit of the empirical coefficients to the building-height ratio works remarkably well, as shown in Figure 5.7b. The resulting profiles, in which $L(\hat{z}; \alpha(r))/A_F$ are estimated entirely based on r, are illustrated in Figure 5.7c. The functions capture well the gradual change from a uniform profile ($r = 1$) to one that has its weight at lower $\hat{z}$ values (i.e. relatively closer to the ground) with increasing r values. Repeated analysis with a larger number of bins yields very similar results, which suggests a robust relationship between the building-height ratio r and the shape of the averaged $\hat{L}(z)$ functions, and indeed that a parametric function like Equation 5.22 is an appropriate parameterization for the total width profiles.

Integration of (5.22) for some height $\hat{z} \in [0, 1]$ to the top of the buildings

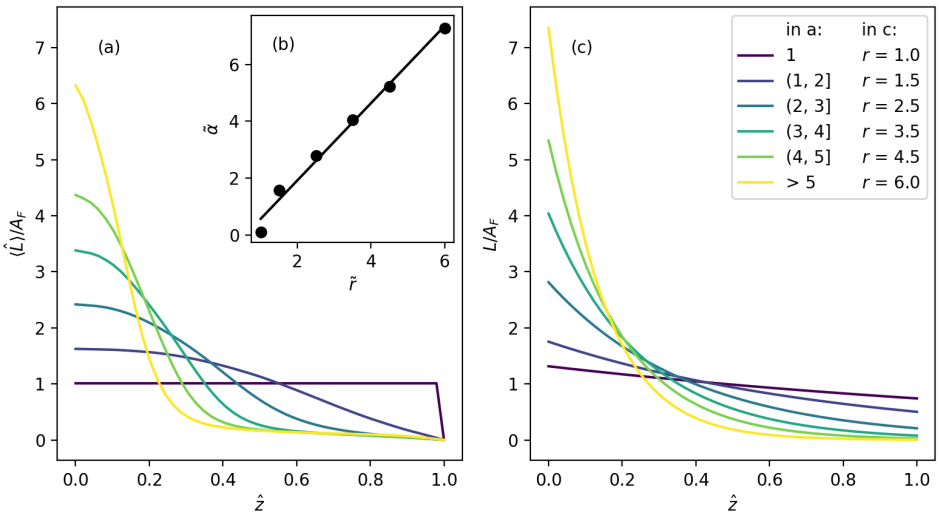

Figure 5.7: Parameterising total width profiles $L(z)$ as a function of building-height ratio $r = z_{\max}/z_H$. (a) Normalised and averaged total width functions $\langle\hat{L}\rangle(\hat{z})/A_F$. (b) Correlation between bin values $\tilde{r}$ and estimated $\tilde{\alpha}$ from curve fitting $\langle\hat{L}\rangle(\hat{z})/A_F$ to $L(\hat{z};\alpha)/A_F$. (c) The functions $L(\hat{z};\alpha(r))/A_F$ parameterising the total width functions. Note that the normalised height $\hat{z}$ in (a) and (c) is shown on the horizontal axis.

results in

$$\begin{aligned}\int_{\hat{z}}^{1}\frac{L(z')}{A_F}\,\mathrm{d}z' &= \int_{0}^{1}\frac{L(z')}{A_F}\,\mathrm{d}z' - \int_{0}^{\hat{z}}\frac{L(z')}{A_F}\,\mathrm{d}z' = 1 - \frac{1-\exp(-\alpha\hat{z})}{1-\exp(-\alpha)} \\ &= \frac{\exp(-\alpha\hat{z}) - \exp(-\alpha)}{1-\exp(-\alpha)} = \frac{\exp(\alpha(1-\hat{z}))-1}{\exp(\alpha)-1}.\end{aligned} \tag{5.24}$$

Substitution of (5.22) into the definition of $\zeta(z)$ (5.15) therefore results in an analytical expression for the normalised frontal area

$$\zeta(z) = \begin{cases}\dfrac{1-\exp(\alpha(1-z/z_{\max}))}{1-\exp(\alpha)}, & z \le z_{\max} \\ 0, & z > z_{\max}\end{cases} \tag{5.25}$$

with $\alpha = 1.355 z_{\max}/z_H - 0.7807$.

5.4 Discussion

This chapter described the calculation of urban morphology parameters and the parameterization of vertical morphology profiles of Greater London. The

objective was to obtain the required input parameters to run the London Model with the distributed drag parameterization, and this study does not intend an in-depth analysis of the urban morphology. However, a few general remarks on the distribution of urban morphology parameters are made in the following.

First note that urban morphology parameters are always dependent on the grid resolution. Appendix D illustrates the morphology parameters computed for a central London area at several different grid resolutions. While the mean values for λ_p, λ_f, and z_H remain similar at different resolutions, the variability increases with higher resolutions. This means that lower grid-box values occur more often (e.g. grid boxes with almost no buildings inside, that is $\lambda_p \approx 0$), and also a higher frequency and more extreme values towards the other end of the parameter distribution (e.g. higher z_H values through high-rise building clusters covering an entire grid box). The maximum building heights behave differently, which is due to λ_p, λ_f, and z_H being grid-box average quantities, whereas $z_{\max}$ is not and therefore changes more between different grid resolutions. Section 7.2.5 discusses the distribution of morphology parameters in more detail and also provides a comparison with the original London Model data.

Concerning the vertical morphology profiles and their parameterization with the building-height ratio $z_{\max}/z_H$, the first thing to notice is that there are very few grid boxes that contain entirely uniform buildings. Many studies of urban airflow are based on these idealised building forms, and the lack of such morphologies in the real data highlights the need for more studies with morphologies of intermediate complexity.

The parameterization of the $\zeta(z)$ profiles uses the maximum to mean building-height ratio as a way to quantify the heterogeneity of the grid boxes. A similar parameter is also used by the Kanda et al. (2013) parameterization for aerodynamic roughness parameters (the parameter X, discussed in Section 6.1.2). Most grid boxes have height-ratio values between 1 and 3. The idealised heterogeneous morphologies studied in the previous chapter are on the lower end of this range, and simulation S4 has the highest ratio amongst the simulations with $r = 1.8$.

The representation of the $\zeta(z)$ profiles by an exponential distribution with $z_{\max}/z_H$ as the independent variable is remarkable, as it is not evident

why London's morphology would be described by such a distribution. It would be intriguing to find out whether this distribution is specific to London or whether this is a universal relation amongst cities. However, the $z_{\max}/z_H$ ratio changes with grid resolution, because $z_{\max}$ changes with resolution (cf. Figures D.7 and D.8) and it not clear whether the linear dependence of the morphology profiles from $z_{\max}/z_H$ remains for other resolutions.

The final remark is on the choice of the morphology profiles. The buildings' total width $L(z)$ was defined from a practical (i.e. easy to compute) perspective. More formally, $L(z)$ could be expressed by a line integral in a similar way to the volumetric drag term $f_D(z)$. The volumetric drag integrates the pressure differences around the buildings, and the frontal area related morphology profile therefore seems the most appropriate choice. Another vertical profile for urban morphologies may be defined by the buildings' total floor area $A_P(z)$, that is the total area occupied by buildings at each height level. This function may be more suitable for representing other aspects of the urban morphology (e.g. vertically distributed energy consumption).

6

Improving drag parameterizations in JULES

On the scale of numerical weather prediction models, urban areas are considered as a particular type of 'surface', and the effects of urban areas on the atmosphere are therefore modelled as part of the exchange between the solid land surface and the atmosphere. There are many different urban land-surface models (Grimmond et al. 2010), which aim to represent the effects of buildings and impervious surfaces without explicitly resolving them. The most widely used type of urban parameterizations are single-layer urban canopy models (Garuma 2018), in which buildings are represented by idealised street canyons and their aerodynamic effects (i.e., the form drag) are modelled via a surface momentum-exchange flux for the lowest height level of the atmospheric model. More sophisticated multi-layer canopy models interact with the atmosphere over several vertical levels (e.g. Martilli et al. 2002).

Urban land-surface models also represent the significant impacts of urban areas on temperature, air pollution and the water cycle. Urban heat islands occur when urban areas are warmer than their rural surroundings (Best and Grimmond 2015; Oke et al. 2017). Different processes contribute to the relative warming of urban environments. Incoming solar radiation and outgoing longwave radiation are absorbed and 'trapped' (through multiple

reflections) by the buildings. Human activities such as energy usage for heating and cooling of buildings generate heat emissions, and lack of water and vegetation means that radiation is transformed into heat rather than moisture. The material properties of buildings and paved surfaces enhance absorption and reduce reflection of solar radiation. The large thermal inertia of these materials means that the energy is released more slowly throughout the day, resulting in higher temperatures at night (Best and Grimmond 2015). These processes are described by the (urban) surface energy balance (Oke et al. 2017):

$$\Delta Q_S = Q^* - Q_H - Q_E + Q_F, \tag{6.1}$$

where ΔQ_S is the net heat storage of the urban fabric, Q^* the net radiation, Q_H the sensible heat flux, Q_E the latent heat flux, and Q_F the anthropogenic heat flux.

This chapter provides a short review on urban parameterizations in numerical weather prediction on the basis of the Met Office models. First, aerodynamic roughness parameterizations are discussed, which are the key modelling components for urban drag (Section 6.1). Then the single-layer urban canopy model framework in the Met Office Unified Model is discussed in more detail, which serves as an example of urban land-surface models in regional NWP (Section 6.2). An experimental set-up to improve the land-surface model JULES, by incorporating a heterogeneous morphology parameterization, is presented in Section 6.3, discussing shortcomings and potential for developments of this modelling approach.

6.1 Urban roughness parameterizations

This section reviews two parameterizations for aerodynamic roughness parameters, which relate vertical wind-speed profiles in the inertial sublayer to the underlying urban morphology (cf. Equation 4.1). The parameterization by MacDonald et al. (1998), which is used in the Met Office urban land-surface model, is based on analytical investigations and wind-tunnel data for square and staggered arrays of cubes. The urban morphology is represented by the plan area index λ_p, frontal area index λ_f, and mean building height z_H. Kanda et al. (2013) aim to better represent aerodynamic roughness parameters for heterogeneous morphologies, for which they propose a

parameterization that incorporates two additional morphology parameters: the maximum building height $z_{\max}$ and the standard deviation of building heights σ_H. Their model is based on a least-squares fit with data from over 100 large-eddy simulations of real urban areas in Japan and more than 20 idealised morphologies. Kent et al. (2017) provide a comprehensive review and assessment of several aerodynamic roughness parameterizations, including the two aforementioned methods. Their analysis of wind-speed profiles of a central London neighbourhood demonstrates that agreement with observations improves when parameterizations consider the height heterogeneity of urban areas.

6.1.1 MacDonald et al. roughness parameterization

The MacDonald et al. (1998) displacement height is estimated by

$$z_d = \left(1 + \alpha_0^{-\lambda_p}(\lambda_p - 1)\right) z_H \tag{6.2}$$

and the roughness length is

$$z_0 = \left(\left(1 - \frac{z_d}{z_H}\right) \exp\left(-\left(0.5\beta_0 \frac{C_D}{\kappa^2}\left(1 - \frac{z_d}{z_H}\right)\lambda_f\right)^{-0.5}\right)\right) z_H \tag{6.3}$$

with parameters $\alpha_0 = 4.43$, $\beta_0 = 1$, and $C_D = 1.2$ for staggered array-type buildings, and $\kappa = 0.4$. Figure 6.1 illustrates the two roughness parameters z_d and z_0 as functions of λ_p and λ_f, normalised by the mean building height z_H. The roughness length z_0 from (6.3) varies with the parameters λ_f, z_H, and λ_p, where λ_p affects z_0 indirectly via the displacement height. The functional relationship between the urban morphology parameters (λ_p and λ_f) and z_0/z_H is commonly illustrated with the underlying assumption that $\lambda_p = \lambda_f$ (dashed line in Figure 6.1b). We extended Figure 6.1b for several other relations between λ_p and λ_f, and also show how the roughness length z_0 changes with λ_f for constant values of λ_p.

6.1.2 Kanda et al. roughness parameterization

The Kanda et al. (2013) displacement-height parameterization is

$$z_d = \left(c_0 X^2 + \left(a_0 \lambda_p^{b_0} - c_0\right) X\right) z_{\max}, \tag{6.4}$$

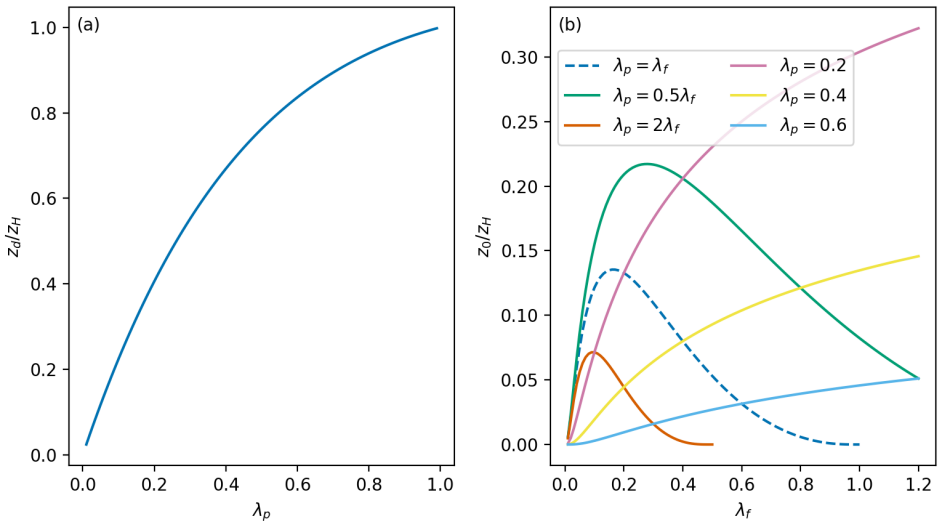

Figure 6.1: MacDonald et al. (1998) parameterization for displacement height and roughness length. (a) Normalised displacement height z_d/z_H for different plan area indices λ_p and (b) normalised roughness length z_0/z_H with different frontal area indices λ_f and different λ_p.

with the building-height ratio parameter

$$X = \frac{\sigma_H + z_H}{z_{\max}}, \tag{6.5}$$

and coefficients $a_0 = 1.29$, $b_0 = 0.36$, and $c_0 = -0.17$. Heterogeneous morphologies have a building-height ratio $0 < X < 1$, where low values represent for example morphologies with isolated tall buildings. Urban morphologies with uniform building heights have $X = 1$, in which case the dispacement height simplfies to $z_d = a_0 \lambda_p^{b_0} z_H$.

Kanda et al.'s parameterization for roughness length (denoted $z_{0,K}$) is a scaling of MacDonald et al. (1998) model ($z_{0,MD}$) with

$$z_{0,K} = (b_1 Y^2 + c_1 Y + a_1) z_{0,MD} \tag{6.6}$$

and

$$Y = \frac{\lambda_p \sigma_H}{z_H}, \tag{6.7}$$

where $a_1 = 0.71$, $b_1 = 20.21$, and $c_1 = -0.77$. Uniform building heights have $Y = 0$, which results in a reduction of the MacDonald et al. roughness length by $a_1 z_{0,MD}$.

Note that the parameterization requires the use of MacDonald et al.'s displacement height (6.2) for the calculation of $z_{0,MD}$ and not their own model (6.4). This is a requirement because Equation 6.3 requires $z_d/z_H \leq 1$ to be well defined, which may not be the case for Kanda et al.'s parameterization of z_d. Equation 6.4 yields displacement heights with $z_d/z_H \leq 1$ only for a limited range of building densities ($\lambda_p \leq 0.5$ for uniform-height morphologies, and even lower limits for heterogeneous morphologies). Kanda et al.'s estimations for displacement height and roughness length are therefore completely separated.

An important difference between the two parameterizations is precisely that the Kanda et al. (2013) model enables displacement heights that exceed the mean building height z_H, which has been well observed for flow over morphologies with heterogeneous building heights (e.g. Xie et al. 2008; Hagishima et al. 2009; Millward-Hopkins et al. 2011; Zaki et al. 2011; Kanda et al. 2013). Kanda et al. (2013) suggest that the maximum building height is a more suitable scaling parameter for the displacement height, and z_d would therefore be bounded by $z_d \leq z_{\max}$. Using $z_d/z_{\max}$ in (6.2) would indeed make the use of Kanda et al.'s displacement height (6.4) compatible with MacDonald et al.'s roughness length for a much larger range of urban morphologies (but the limit of $\lambda_p \leq 0.5$ for uniform morphologies remains).

Figure 6.2 shows the parameter curves of normalised displacement height z_d/z_H and normalised roughness length z_0/z_H for the MacDonald et al. (1998) and Kanda et al. (2013) parameterizations with urban morphology parameter values from the large-eddy simulation study (Table 3.1). The parameter curve for normalised roughness length in Figure 6.2b therefore assumes the relation $\lambda_p = 2.1\lambda_f$. Estimated aerodynamic parameter values of the LES data from the mid-range fitting region (Section 4.3.1) are plotted on top. The figure illustrates that the large spread of values estimated from the LES data is approximated by a smaller range in the Kanda et al. (2013) parameterization and just a single value in the MacDonald et al. (1998) parameterization.

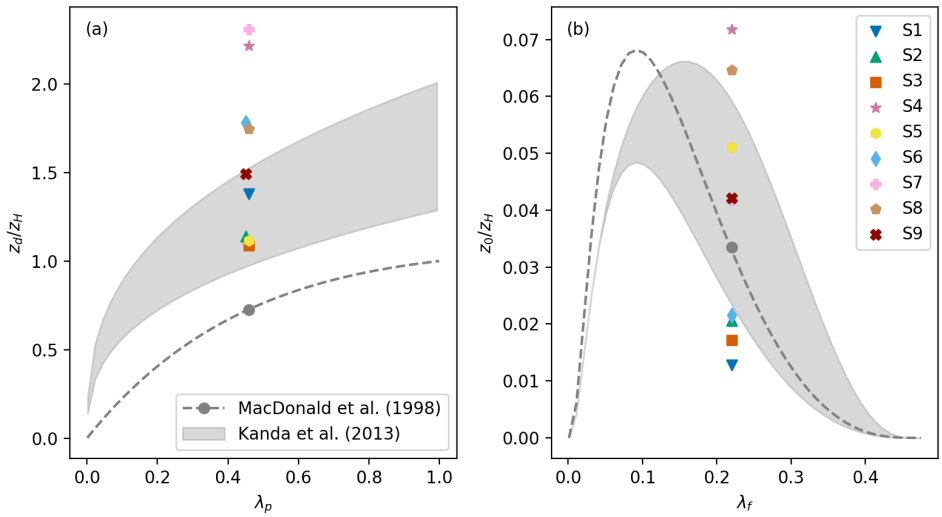

Figure 6.2: Comparison of aerodynamic roughness parameterizations and roughness parameter values from large-eddy simulations S1–S9. Parameter curves for (a) normalised displacement height and (b) normalised roughness length from the MacDonald et al. (1998) (dashed line) and Kanda et al. (2013) (shading) parameterizations, parameter values for MacDonald et al. (1998) (grey dot) and estimated values for simulations S1–S9 from the mid-range fitting region (markers).

6.2 Met Office urban land-surface model

This section reviews the current modelling framework for urban areas in the Met Office Unified Model (UM), which serves as an example of urban land-surface models (which include both an aerodynamic roughness parameterization and a surface energy balance model) in numerical weather prediction. The Unified Model is a numerical model of the atmosphere, which is used for numerical weather prediction, seasonal forecasting, and climate modelling. The model core is identical across the range of spatial and temporal scales and can be used as a global or regional model.

6.2.1 JULES

Urban areas in the Unified Model are modelled by the Joint UK Land Environment Simulator (JULES; Best et al. 2011; Clark et al. 2011), which parameterises surface subgrid-scale processes and their exchange with the atmosphere. The model separates different surface types within a grid box

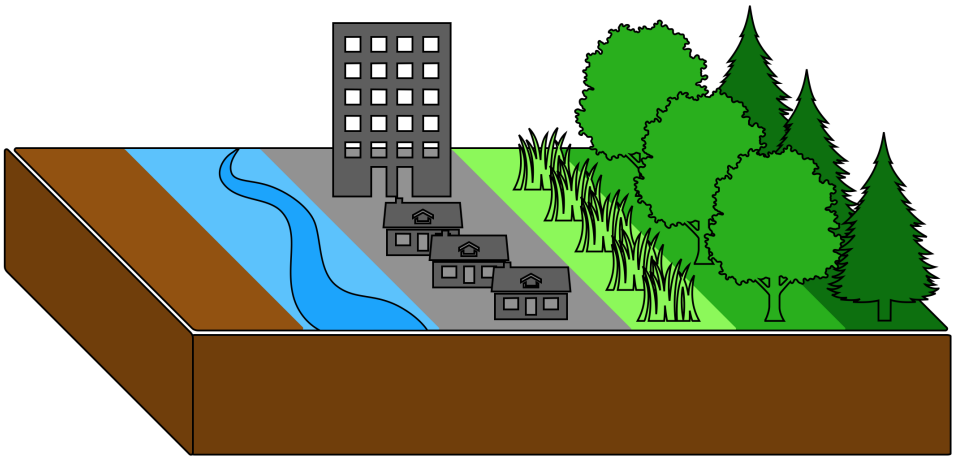

Figure 6.3: Schematic of the tile-based land-surface exchange model JULES.

into tiles (Figure 6.3), where subgrid processes are calculated in parallel for each tile with its own defined properties. JULES consists of vegetated tiles (broad-leaf trees, needle-leaf trees, temperate grass, tropical grass, and shrubs), urban, water, soil and ice tiles. For each of these tiles JULES calculates a separate surface stress and a separate surface energy balance. The results of these calculations are combined into surface exchange fluxes by weighting the contributions from the tiles by their grid-box fraction. The surface fluxes are implicitly coupled to the atmosphere (Best et al. 2004).

The surface exchange flux of momentum, which parameterises frictional and aerodynamic effects of the surface, is modelled by (Best et al. 2004; Lock et al. 2020)

$$\tau_{0,i}(U, u_i) = \rho_0 C_M U \, u_i, \tag{6.8}$$

where ρ_0 is the density of air at the surface, C_M a momentum-exchange coefficient, $U(t)$ the wind speed, and $u_i(t)$ a horizontal wind velocity component, which are evaluated at the lowest model-level height. The momentum-exchange coefficient is modelled by (Lock et al. 2020)

$$C_M = \frac{\kappa^2}{\Phi_m^2} \tag{6.9}$$

where κ is the von Kármán constant and Φ_m a momentum stability function, which is modelled in neutral atmospheric stability conditions as

$$\Phi_m = \ln\left(\frac{z_1 + z_0}{z_0}\right), \tag{6.10}$$

where z_1 is the height of the lowest atmospheric level and z_0 the momentum roughness length of the surface tile. The function Φ_m has modifications for other atmospheric stability conditions (Lock et al. 2020).

The surface exchange flux of sensible heat, Q_H, is modelled as (Porson et al. 2010a; Best et al. 2011)

$$Q_H(T_j, T, U) = \rho_0 c_p C_H U (T_j - T) f_H, \tag{6.11}$$

where $T_j(t)$ is the temperature at the tile surface, $T(t)$ the temperature and $U(t)$ the wind speed at the lowest atmospheric level, c_p is the specific heat capacity of air, C_H a heat-exchange coefficient, and f_H a stability correction. The heat-exchange coefficient is modelled by (Porson et al. 2010a; Lock et al. 2020)

$$C_H = \frac{\kappa^2}{\Phi_m \Phi_h} \tag{6.12}$$

with stability function for heat

$$\Phi_h = \ln\left(\frac{z_1 + z_0}{z_{0h}}\right), \tag{6.13}$$

where z_{0h} is the heat roughness length of the surface tile. The function Φ_h has modifications for other atmospheric stability conditions (Lock et al. 2020). The models for other surface energy balance terms are discussed directly for the urban surface below.

6.2.2 MORUSES

JULES has several schemes for the calculation of urban properties of different complexity, where simpler schemes are for instance used in climate modelling. In regional weather forecasting, the calculation of urban properties within JULES is covered by the Met Office–Reading Urban Surface Exchange Scheme (MORUSES; Porson et al. 2010a,b; Bohnenstengel et al. 2011; Bohnenstengel and Hendry 2016), a single-layer urban canopy model. Urban areas in MORUSES are represented by a generic street canyon with height H, street width W and total width R (see illustration in Figure 6.4). A characterisation of the urban canyon is given by the canyon aspect ratio H/W. For example, a high H/W is characteristic for high-rise buildings with narrow street canyons. The canyon fraction W/R is a characteristic similar to the plan area index.

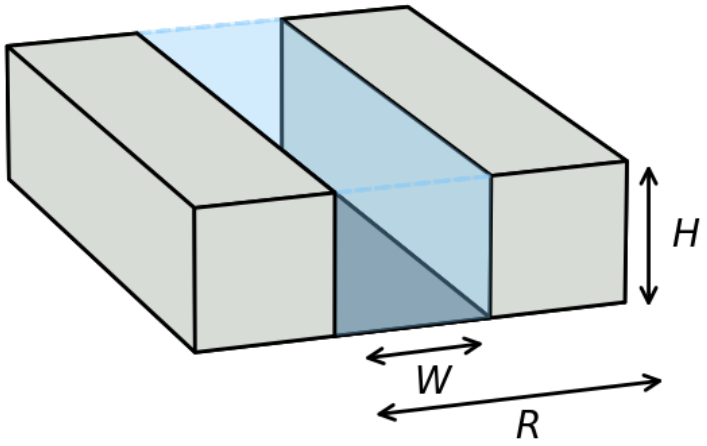

Figure 6.4: Generic street canyon approximation for urban environments in MORUSES.

MORUSES considers two separate urban tiles: the urban fraction of a grid box is split into a flat surface representing the roof area and a 'bulk surface' representing the street canyon, which contains the two building side-walls, the road surface, and the air in between them. The urban roof grid-box fraction is usually set to be equal to the plan area index λ_p, and the canyon grid-box fraction is the remainder of the total urban grid-box fraction as determined from land-cover data.

MORUSES has fixed properties for building-wall-, building-roof-, and road-surfaces, which are derived from the material characteristics of brick (walls), clay (roof), and asphalt (road) (Porson et al. 2010a; Bohnenstengel et al. 2011). The street-canyon geometry varies with each grid box, and MORUSES calculates bulk parameters for the urban tiles based on the canyon geometry and material properties. The surface energy balance for the urban canyon ($k = c$) and urban roof ($k = r$) tiles is (Porson et al. 2010a)

$$C_k \frac{\mathrm{d}T_k}{\mathrm{d}t} + Q_{G,k}(T_k, T_s) = Q_k^*(T_k) - Q_{H,k}(T_k, T, U) + Q_{F,k}, \tag{6.14}$$

where $T_k(t)$ is the tile-surface temperature and $T_s(t)$ the temperature of the soil. Heat storage (ΔQ_S in Equation 6.1) is modelled as the thermal inertia of the buildings $C\,\mathrm{d}T/\,\mathrm{d}t$ with areal heat capacity C, and a ground heat flux Q_G.

The canyon-tile ground heat flux $Q_{G,c}$ is modelled by conductive coupling to the soil, and the roof tile $Q_{G,r}$ is radiatively coupled to the soil. The net

radiation term Q_c^* of the urban canyon tile models multiple reflections and trapping of short- and longwave radiation. The anthropogenic heat flux Q_F is modelled by a fixed flux with daily changing values, scaled by the urban tile fraction (Hertwig et al. 2020). Equation 6.14 does not contain an urban latent heat flux Q_E because there is no parameterization for the effects of urban vegetation within MORUSES. Instead, urban vegetation is modelled by the vegetation tiles of JULES. The parameterizations for ground heat flux Q_G and net radiation Q^* are documented in Appendix C.

The following parameters for the canyon and roof tiles are provided by MORUSES (Section 6.2.4 and Appendix C): tile roughness lengths for momentum z_0 (the same for canyon and roof tiles) and heat $z_{0h,k}$, the tile areal heat capacity C_k, a thermal conductivity parameter λ for the canyon-tile ground heat flux, and tile albedo α_k and emissivity ϵ_k for net radiation.

6.2.3 Building geometry in MORUSES

MORUSES maps the three-dimensional grid-box morphology, given by the input parameters plan area index λ_p, frontal area index λ_f, and mean height z_H, onto the two-dimensional street-canyon representation. In the MORUSES geometry, the 'infinite' canyon length is $D = \lim d \to \infty$, and the total plan area is $A_T = DR$. The building in the street-canyon domain (the street canyon is considered one-sided) has height $B_h = H$, length $B_l = (R - W)$ and width $B_w = D$ for a cross-canyon flow. The urban morphology parameters are therefore given by (cf. Porson et al. 2010a)

$$z_H = H, \tag{6.15}$$

$$\lambda_p = \frac{B_w B_l}{A_T} = \frac{D(R-W)}{DR} = 1 - \frac{W}{R}, \tag{6.16}$$

and

$$\lambda_f = \frac{B_w B_h}{A_T} = \frac{DH}{DR} = \frac{H}{W}\frac{W}{R}. \tag{6.17}$$

Averaging the building width over all wind directions (cf. Equation 5.10) yields

$$\lambda_f = \frac{2(B_w + B_l)B_h}{\pi A_T} = \frac{2H(D+R-W)}{\pi DR} = \frac{2}{\pi}\frac{H}{W}\frac{W}{R}. \tag{6.18}$$

Note that due to the infinite canyon length, the building width in the along-canyon direction is zero in this representation. The canyon geometry parameters are in turn obtained by (Porson et al. 2010a)

$$\frac{W}{R} = 1 - \lambda_p \tag{6.19}$$

and

$$\frac{H}{W} = \frac{\pi}{2}\frac{\lambda_f}{(1-\lambda_p)}. \tag{6.20}$$

6.2.4 Parameter calculations of MORUSES

MORUSES calculates the momentum and heat roughness lengths for the urban tiles, which are used in the momentum exchange (6.9) and heat exchange parameterizations (6.12). The momentum roughness length z_0, which is the same for both urban canyon and roof tiles, is estimated via the MacDonald et al. (1998) parameterization for staggered arrays (see Section 6.1). The roughness length for heat z_{0h} for urban surfaces is parameterised using z_0 and a resistance network that models the conduction of heat (Harman et al. 2004; Porson et al. 2010a). The roughness length for heat is given by

$$z_{0h,k} = H(z_1 + z_0)\left(H\exp\left(\frac{\kappa^2 r_{bulk,k}}{\ln\left(\frac{z_1+z_0}{z_0}\right)}\right)\right)^{-1} \tag{6.21}$$

with the bulk resistance term $r_{bulk,k}$ which is modelled differently for the canyon tile and the roof tile. The resistances consider different flow regimes based on the canyon aspect ratio H/W.

The calculation of the tile heat capacity C_k is presented to illustrate how the geometry of the urban canyon specifies the bulk parameter values. The areal heat capacity C_k depends on the surface volumetric heat capacity c_k and the material thickness Δz_k for the road ($k = b$), wall ($k = w$) and roof ($k = r$) surfaces (Porson et al. 2010a; Bohnenstengel and Hendry 2016). Since the roof tile is a flat surface with the characteristic length $(R - W)$, its geometry is simply represented by

$$(R - W)C_r = (R - W)c_r\Delta z_r, \tag{6.22}$$

and thus the roof tile heat capacity is directly inferred from the material properties of the roof:

$$C_r = c_r \Delta z_r. \tag{6.23}$$

The canyon geometry is represented by a road and two wall surfaces:

$$WC_c = Wc_b \Delta z_b + 2Hc_w \Delta z_w, \tag{6.24}$$

which yields the canyon heat capacity

$$C_c = c_b \Delta z_b + 2\frac{H}{W} c_w \Delta z_w. \tag{6.25}$$

A similar geometric derivation is used for albedo α_k and emissivity ϵ_k of the urban tiles, based on albedos and emissivities of the building- and road-materials, and further involves calculating multi-reflections within the canopy to model radiative trapping (Appendix C).

6.3 Extending JULES for heterogeneous morphologies

This section describes the first attempt to introduce subgrid heterogeneity into the Met Office urban land-surface model JULES, which was made by replacing the MacDonald et al. (1998) parameterization for momentum roughness length with the Kanda et al. (2013) parameterization. However, an underlying assumption on the height coordinate in MORUSES prevents a direct implementation of Kanda et al.'s parameterization into JULES.

Conceptually, JULES estimates the surface exchange at height $z_d + z_0$, where the wind speed of a logarithmic wind profile equals zero (Hertwig et al. 2020). The effective height of the street canyon in MORUSES is therefore at $z_H - z_d - z_0$. MORUSES applies the following scaling to the wind speed U, evaluated at the lowest atmospheric level at height z_1, to obtain the wind speed at the canopy top U_{CT} (Harman et al. 2004, equation 11):

$$\frac{U_{CT}}{U} = \ln\left(\frac{z_H - z_d}{z_0}\right) / \ln\left(\frac{z_1 - z_d}{z_0}\right). \tag{6.26}$$

However, this calculation defaults to zero if $z_d > z_H$, as can be the case in the Kanda et al. (2013) model. The individual resistances in the calculations of

the bulk resistance term r_{bulk} are normalised by the canopy-top wind speed, which causes JULES to fail at the calculation of the heat roughness length (6.21).

6.3.1 Model comparisons

The full Kanda et al. (2013) parameterization can only be used if $z_d/z_H < 1$, otherwise the canopy-top wind speed defaults to zero and JULES fails. We therefore tested two alternative approaches.

First, we used Kanda et al.'s roughness length $z_{0,K}$ (6.6), but left the displacement height to the original MacDonald et al. values $z_{d,MD}$ (6.2). The momentum roughness length in the model is entirely replaced by $z_{0,K}$ (e.g. within the momentum- and heat-exchange coefficients C_M and C_H), but the relative height level of the canopy top is calculated from both $z_{0,K}$ and $z_{d,MD}$, which causes an inconsistency in the modelled heat roughness length (via the bulk resistance term).

Second, we attempted an implementation that would be closest to Kanda et al.'s original proposal, where we replaced the scaling length for displacement height with $z_{\max}$. We used $z_{\max}$ instead of z_H and H in all calculations directly affected by the displacement height, that is: in the interpolation of the wind speed (6.26), in the calculation of the bulk resistances, and in the roughness length for heat (6.21). This change has unclear effects on the representation of the canyon geometry.

The model runs are hereinafter called: MD for the original MacDonald et al. (1998) parameterization, K0 for the full Kanda et al. (2013) parameterization, K1 for using Kanda et al.'s roughness length $z_{0,K}$, and K2 for using Kanda et al.'s parameterization with scaling length $z_{\max}$.

6.3.2 Case set-up

Three test cases were defined to represent a dense city centre, a residential neighbourhood, and a suburban zone, by choosing appropriate values for H/W, W/R, z_H, $z_{\max}$, and σ_H. The urban morphology parameters and aerodynamic roughness parameters derived from MacDonald et al. (1998) and Kanda et al. (2013) for the test cases are listed in Table 6.1. Kanda et al.'s displacement heights $z_{d,K}$ are consistently higher than MacDonald

	H/W	W/R	z_H	$z_{\max}$	σ_H	$z_{d,MD}$	$z_{d,K}$	$z_{0,MD}$	$z_{0,K}$
Sub.	0.3	0.8	7 m	10 m	1 m	3 m	6 m	0.8 m	0.5 m
Res.	1	0.6	13 m	30 m	5 m	9 m	18 m	1 m	1.1 m
City	2	0.4	17 m	180 m	9 m	14 m	32 m	0.5 m	1.2 m

Table 6.1: Urban morphology parameter set-up and derived aerodynamic roughness parameters for three JULES test cases: a suburban zone (Sub.), a residential neighbourhood (Res.), and a dense city centre (City).

et al.'s $z_{d,MD}$, and for the city centre and residential test case they exceed z_H, which means that the original Kanda et al. (2013) model (K0) could only be used for the suburban case. Kanda et al.'s roughness length $z_{0,K}$ is higher for the city centre, approximately equal for the residential case, and lower for the suburban case, compared to MacDonald et al.'s roughness length $z_{0,MD}$.

JULES is used in a single-column, standalone mode with external meteorological forcing from the Met Office observation site at Cardington (Lat 51.10°, Lon -0.42°) for the year 2005. Cardington is not an urban site, however this is unlikely to have an effect in this idealised model comparison. The forcing data consists of wind speed, air temperature, specific humidity, pressure, downward longwave irradiance, downward shortwave irradiance, and rainfall rate at $z_1 = 10$ m elevation and averaged over 30 minutes. There is no anthropogenic heat source in the model simulations.

To simplify the analysis, the JULES simulations are set up to only consist of two tiles, an urban canyon and an urban roof tile. The grid-box fraction between these tiles is determined by the plan area index: the roof fraction is λ_p, and the canyon fraction is $1 - \lambda_p$. MORUSES is used in the standard configuration as described above, i.e. with conductive coupling of the canyon to the soil and radiative coupling of the roof (Bohnenstengel and Hendry 2016; Gilham et al. 2020). The tile capacity for storing water (e.g. in puddles or with pervious surfaces) has been set to zero, such that there is no latent cooling and thus no significant latent heat flux resulting from it. Note that since the wind speed is an external forcing, the momentum exchange in (6.8) does not have any effect on the wind speed in the surface sensible heat flux in (6.11), which would be the case in a fully coupled JULES-atmosphere

simulation. We will therefore only consider surface energy balance terms in the model comparison.

6.3.3 Results

Figure 6.5 shows the mean summer-seasonal diurnal cycles for surface sensible heat flux $Q_H(t)$ and surface temperature $T(t)$ for the different model runs at the three test sites, and Figure 6.6 shows the deviations in mean diurnal cycles of the various Kanda et al. (2013) implementations from the original MacDonald et al. (1998) scheme. The quantities are grid-box averages (i.e. average of canyon tile and roof tile) and show the mean (solid lines), and the maximum and minimum values (shading) of the summer season. The summer season (June, July, August) was chosen for the model comparison because the surface energy balance terms and thus the effects of the different model schemes are largest at this time of the year.

The most striking differences occur for the full implementation of the Kanda et al. (2013) parameterization (K0), which is only applicable for the suburban case. The simulation results in much lower surface sensible heat fluxes and excessively larger surface temperatures with an average of 4° K above the original scheme (K0 in Figure 6.6d). Such drastic changes for a case with little urban density are surprising, and these results indicate that a full implementation of the Kanda et al. (2013) parameterization could require the re-design of other urban surface modelling components.

Higher roughness lengths generally yield lower canopy-top wind speeds (cf. Equation 6.26 and Table 6.2), which results in lower sensible heat fluxes and thus higher surface temperatures through decreased mixing in the near-surface region. This is most evident at the city centre grid box (K1 in Figure 6.6f), which results in a relative warming compared to the original scheme. A relative cooling is found for the suburban test case with the new $z_{0,K}$ (K1 in Figure 6.6d), and only marginal differences (slight temperature increases, K1 in Figure 6.6e) for the residential case.

However, when using $z_{\max}$ as a scaling length for the displacement height $z_{d,K}$ (K2), the canopy-top wind speed increases significantly for both the city-centre and residential test case, and remains approximately equal for the suburban case (Table 6.2). Higher wind speed forcings increase the surface sensible heat flux Q_H, which increases mixing and in turn decreases the sur-

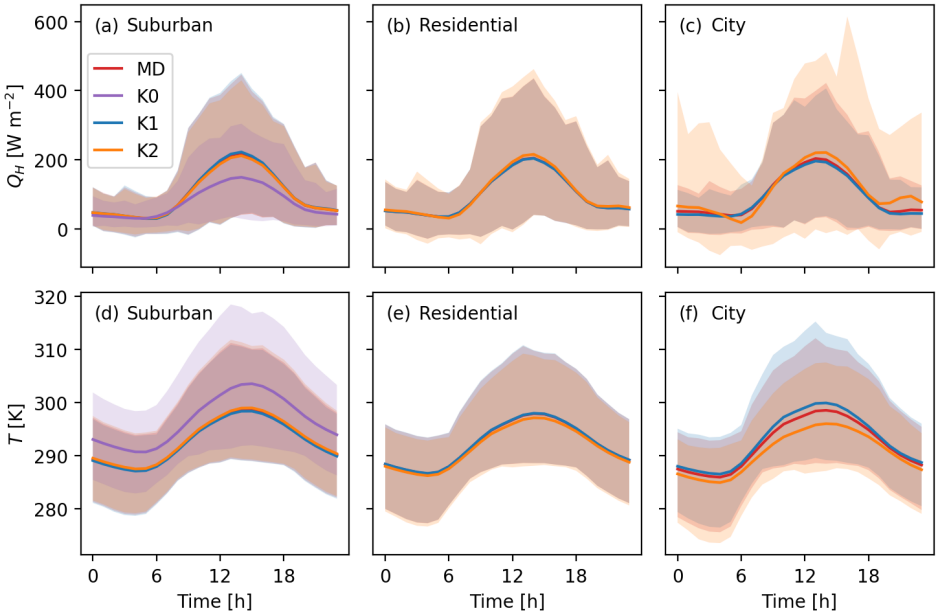

Figure 6.5: Mean summer-seasonal diurnal cycles with range (shading) for surface sensible heat flux $Q_H(t)$ and surface temperature $T(t)$ at a (a, d) suburban, (b, e) residential, and (c, f) city centre JULES grid box. The quantities are grid-box values and averaged over the summer months June, July, and August. The simulations are using the original MacDonald et al. (1998) (MD) model, the Kanda et al. (2013) (K0) model, Kanda et al.'s roughness length $z_{0,K}$ only (K1), and Kanda et al.'s model with scaling length $z_{\max}$ (K2).

face temperature T. This change in U_{CT}/U means that the opposite effects are observed between K1 and K2, even though the momentum roughness length is the same (however the roughness length for heat changes). Particularly for the city-centre setting, the wind-speed scaling in K2 can lead to occasionally very high surface heat fluxes (spread of K2 in Figure 6.5c) and significant temperature reductions (K2 in Figure 6.6f) with an average of around -2° K. These results suggest that wind-speed effects are dominant processes in the turbulent flux calculations, and that the model used for interpolating the wind speed at reference height to the canyon geometry is of great importance.

The representation of heterogeneous morphologies within the current two-dimensional street-canyon geometry is challenging. In particular, the simple assumption on the scaling of the wind speed in the urban canopy

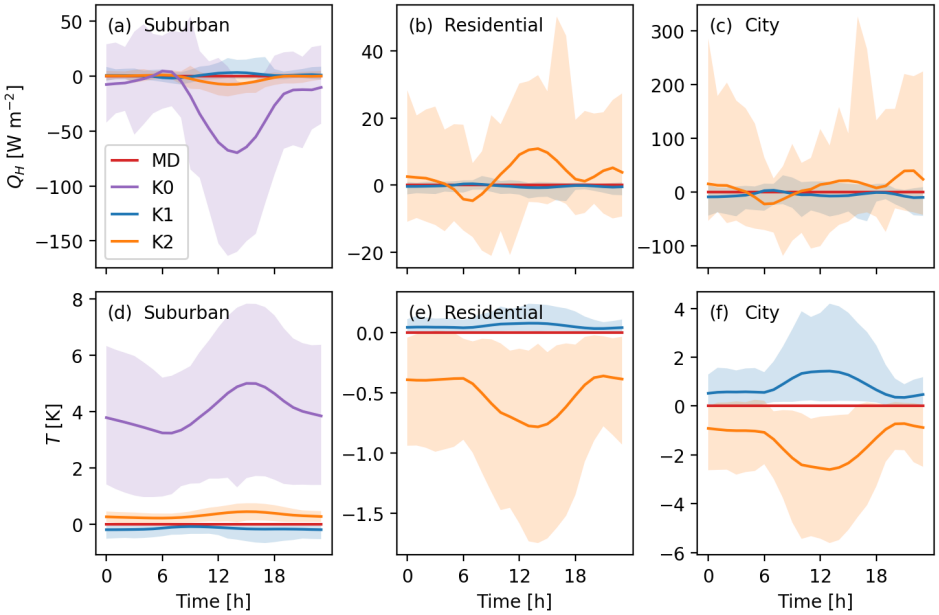

Figure 6.6: Deviations in mean summer-seasonal diurnal cycles from the original MacDonald et al. (1998) model with range (shading) for surface sensible heat flux $Q_H(t)$ and surface temperature $T(t)$ at a (a, d) suburban, (b, e) residential, and (c, f) city centre JULES grid box. The quantities are grid-box values and averaged over the summer months June, July, and August. Note the different scales on the y-axis. The simulations are using the original MacDonald et al. (1998) (MD) model, the Kanda et al. (2013) (K0) model, Kanda et al.'s roughness length $z_{0,K}$ only (K1), and Kanda et al.'s model with scaling length $z_{\max}$ (K2).

(Equation 6.26) is incompatible with more realistic parameterizations of wind speed provided by Kanda et al. (2013). The first step towards more urban subgrid heterogeneity in JULES would therefore need to be aiming at improving the wind speed interpolation in the canyon resistance network. This could potentially be simple to improve, e.g. by replacing the wind speed scaling with a commonly assumed exponential wind profile within the urban canopy (cf. MacDonald (2000), although Castro (2017) showed the limited applicability of this approximation). However, it remains unclear how the street-canyon geometry could be adapted for heterogeneous building heights, and how this affects the parameterised processes that are based on the uniform height assumption, as the test case with changed scaling height (K2) suggests.

Table 6.2: Scaling of the canopy-top wind speed U_{CT}/U for the different JULES model schemes and test cases.

U_{CT}/U	MD1	K0	K1	K2
Suburban	0.64	0.2	0.69	0.67
Residential	0.61	-	0.59	1.04
City	0.57	-	0.38	2.15

The significant depth of the bulk surface representing the urban canyon remains an issue to be solved. Note that although conceptually the height of the surface is lifted to $z_d + z_0$ when using the urban land-surface model, this step is not explicitly implemented in the way JULES is coupled to the atmosphere in the Unified Model. Omitting these modifications to the ground-level height causes an ambiguity on how the model output should be interpreted. When comparing model output variables to observational data at individual grid boxes, the model output is often lifted to the MORUSES coordinate height in post-processing (e.g. Simón-Moral et al. 2019). However, this is inconsistent with how the atmospheric boundary layer is modelled in the UM. When urban drag is modelled as an explicit stress term (Chapter 7) such ambiguity does not exist, since the urban canopy is vertically distributed within the boundary layer and the surface is simply located at the ground level.

7

Distributed drag parameterization in the London Model

This chapter describes the process of incorporating the distributed drag model into a high-resolution numerical weather prediction model, the Met Office London Model. Section 7.1 outlines the model set-up and the modifications to the current urban surface scheme, such that the distributed drag can be added to the momentum equations as an additional stress term. Section 7.2 describes the set-up of a case study for one summer day. LIDAR observations of aerosols over London were available for the case date and are used as additional tool for model evaluation. Three different model configurations are compared in the study: the original model configuration, the standard set-up with updated morphology inputs, and the model with the distributed drag parameterization. Section 7.3 discusses the results from the case study by comparing the model behaviour of the three model runs. The section focuses on surface stresses, wind speed at several vertical levels, and turbulence production by evaluating the height of surface-based vertical mixing. Section 7.4 discusses the implications of this work for future developments of urban parameterizations.

7.1 Model set-up

7.1.1 The London Model

The London Model (LM; Boutle et al. 2016) is a very high resolution version of the Met Office Unified Model. The model domain covers the Greater London area and its surroundings at a horizontal grid length of 0.003° (approximately 333 m). The initial and boundary conditions are given by the main Met Office forecast model for the United Kingdom, the 1.5 km horizontal resolution UKV model (Tang et al. 2013). The data is supplied from a UKV analysis model run, which is a deterministic forecast which incorporates observational data through data assimilation. The UKV model output is horizontally regridded to the London Model; the vertical resolution of the two models are identical. The numerical set-up of the London Model follows the RAL1-M science settings as described in Bush et al. (2020). The model is run with a timestep of 12 s. Both the UKV and the London Model explicitly resolve convection, and urban areas are parameterised with MORUSES (see Section 6.2.2).

7.1.2 Distributed urban drag model

In Chapter 4, a neighbourhood-scale model for height-dependent contributions of urban areas to wind stress was developed using building-resolving large-eddy simulations in neutrally stable conditions. The canopy model represents building effects by a height-distributed frontal area, which allows for a detailed representation of the vertical structure of urban areas. This representation may be particularly important for areas containing high-rise buildings and grid boxes with large subgrid heterogeneity.

As discussed in Chapter 4, the model parameterises the drag force exerted by buildings onto the airflow as an explicit stress term that is added to the momentum equations. The urban drag at time t and height z, for each grid box, is given by

$$\tau_{D,i}(t,z) = \tau_{0,i}(t)s(\zeta(z)), \tag{7.1}$$

where $\tau_{0,i}(t)$ is the total urban canopy drag (or surface stress), $\zeta(z)$ the normalised frontal area, and $s(\zeta)$ is the drag distribution function. Note that in contrast to the previous chapters, the stresses in this chapter are

not kinematic quantities, but express a force per area (in Pascal). The (dimensionless) normalised frontal area is modelled by (see Chapter 5)

$$\zeta(z) = \begin{cases} \dfrac{1 - \exp(\alpha(1 - z/z_{\max}))}{1 - \exp(\alpha)}, & z \leq z_{\max} \\ 0, & z > z_{\max} \end{cases} \tag{7.2}$$

with $\alpha = 1.355 z_{\max}/z_H - 0.7807$, where $z_{\max}$ is the maximum building height and z_H is the mean building height of the grid box.

The drag distribution function $s(\zeta)$ is represented by the third-order polynomial

$$s(\zeta) = C_1\zeta^3 + C_2\zeta^2 + (1 - C_1 - C_2)\zeta \tag{7.3}$$

with $C_1 = 1.88$ and $C_2 = -3.89$. The fact that s is not a linear function of ζ indicates that taller buildings are responsible for a larger proportion of the drag. The coefficients C_1 and C_2 were the result of a best fit from the simulation data of semi-idealised neighbourhoods with identical λ_p and λ_f values (Section 4.5) and are chosen as such because they are currently the only available data. While we expect the general relationship between the urban morphology profiles and distributed drag profiles to hold for a wide range of morphologies, it is not known to which extent the buildings' density, buildings' alignment with respect to wind direction or atmospheric stability influence the cubic fit and parameter values of C_1 and C_2.

In order to predict the total surface stress $\tau_{0,i}(t)$, we adapt the model of Coceal and Belcher (2004) and Belcher (2005) as outlined in Section 4.6. The total canopy drag is parameterised by (cf. Equation 4.14)

$$\tau_{0,i}(t) = \rho_0 \frac{1}{2} c_D \lambda_f U(t)\, u_i(t), \tag{7.4}$$

with drag coefficient c_D, frontal area index λ_f, air density ρ_0, horizontal wind velocities $u_i = u, v$, and wind speed $U = \sqrt{u^2 + v^2}$. Instead of specifying a drag coefficient from the literature, the value of c_D will be chosen such that the distributed drag parameterization can be directly compared to the standard parameterization in the London Model (see Section 7.2.4).

7.1.3 Modifications to the urban surface scheme

The proposed momentum-exchange scheme models urban drag as an explicit, height-dependent stress term in the atmospheric boundary layer, where

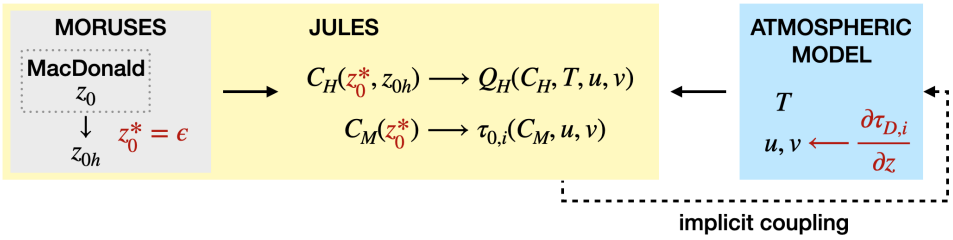

Figure 7.1: Modifications to the urban surface parameterization for the distributed drag scheme. The new model (red) replaces the momentum roughness length z_0 with $\epsilon = 10^{-5}$ m *after* the calculation of the heat roughness length z_{0h}. The horizontal velocities u and v are subject to the additional forcing $\partial \tau_{D,i}/\partial z$.

the vertical gradient of (7.1) is included in the horizontal momentum equations as additional body force. The Unified Model has a parameterization for distributed orographic drag (form drag induced by unresolved small-scale hills, Wood et al. 2001), which was used as the basis for this implementation. Since the urban drag model does not account for the material (scalar) effects of urban areas, MORUSES parameterizations are used for the radiation, heat, and moisture exchange.

Figure 7.1 shows the different model components affected by the distributed drag scheme and highlights the following modifications to the surface exchange scheme, that were required to incorporate the distributed drag. To prevent applying urban form effects twice, i.e. via an effective roughness length in the momentum-exchange coefficient C_M in JULES (Equation 6.8) and a distributed form drag, the momentum roughness length z_0 in MORUSES is reset to the value $\epsilon = 10^{-5}$ m representing a small material roughness length, after z_{0h} has been calculated. The roughness length for heat, z_{0h}, therefore remains unchanged as parameterised by MORUSES using the MacDonald et al. (1998) momentum roughness length (see Section 6.1.1) and a resistance network (cf. Equation 6.21). We note that this set-up causes an inconsistency for the heat-exchange coefficient C_H in JULES (see Equation 6.12), which depends on both the momentum and heat roughness lengths and is calculated with the small momentum roughness length and the 'normal' (MORUSES) heat roughness length. Due to the complex JULES code it was not possible to resolve this inconsistency in the time available. The effects of this inconsistency are further explored in Section 7.3.3.

The urban drag parameterization is set up to replace the MORUSES momentum-exchange scheme in all grid boxes which have a building plan area index of $\lambda_p > 0.1$. This threshold includes suburban grid boxes at the periphery of Greater London and other large towns in the domain, but does not include individual buildings outside these urban patches. The drag scheme replaces MORUSES in 14 % of the domain area. For these areas, the parameterization does not only apply to the lowest vertical model level, but extends to all grid boxes with heights below the maximum building height $z_{\max}$. Figure 7.2 shows the London Model domain with the highest (model-level) heights where the drag parameterization scheme applies.

Most commonly, the distributed drag scheme affects the lowest two or three vertical model levels (up to 22 m and 45 m above ground level (a.g.l.), respectively, Figure 7.2a), whereas in central London (Figure 7.2c) the scheme frequently exerts drag on the fourth model level (45 m to 75 m a.g.l.) and occasionally higher. It reaches the ninth vertical level (262 to 325 m a.g.l.) around the Shard, the tallest building in the domain. Figure 7.2d illustrates profiles of $\lambda_f \zeta(z)$ for some reference neighbourhoods (see Section 7.2.1). This scaled quantity illustrates the frontal area index above height z (with λ_f at ground level), which gives an indication of the magnitude of the stress applied at this height. The $\zeta(z)$ profiles are calculated using (7.2), where mean and maximum building heights are obtained from the neighbourhoods' central grid boxes.

7.2 Case study and model comparison set-up

7.2.1 Case study

The case study period is 26 June 2018 with a 36-hour forecast run using the London Model starting from 25 June 18:00 UTC. This cloud-free period had easterly winds and an average wind speed of 5 m s^{-1} (London City Airport, at 5 m a.g.l.). Analysis of the model behaviour will focus on a 10 × 15 km^2 area of central London (Figure 7.2c and Figure 7.3), which is densely built-up and includes the historical centre and high-rise area of the City. The cluster of high-rise buildings of Canary Wharf is in the east. In the west there are three large parks: The Regent's Park, Hyde Park and Battersea Park. De-

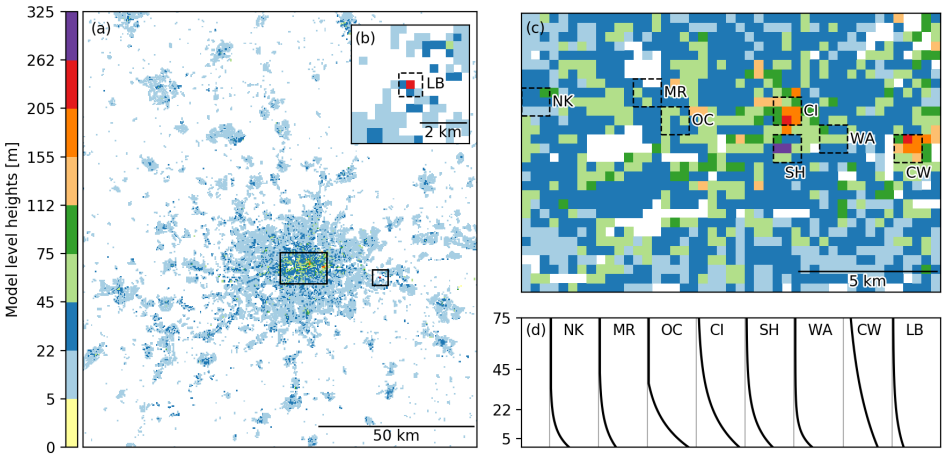

Figure 7.2: Highest vertical model level where the drag parameterization scheme applies for grid boxes with $\lambda_p > 0.1$ for (a) the full London Model domain with rectangles to show the locations of (b) the Thames estuary area, and (c) the central London study area with locations of the (d) vertical profiles of $\lambda_f \zeta(z)$. Profiles are from the centre grid boxes of the reference neighbourhoods. Notation of the reference neighbourhoods is defined in Section 7.2.1.

tailed analysis of 1 km^2 (3×3 grid boxes) neighbourhoods includes: Oxford Circus (OC), City (CI), Shard (SH), Wapping (WA), Canary Wharf (CW), and Littlebrook Power Station (LB). The first five are within the central London area. Littlebrook Power Station (Figure 7.2b), a former coal-fired power station in the Thames estuary with a 211 m high chimney, provides a reference for an isolated tall building in a low-density urban area. The power station ceased operating in March 2015 and the chimney was demolished in December 2019. While the City and Canary Wharf neighbourhoods contain high-rise buildings above 200 m and the Shard (London's tallest building) is 304 m high, neither the Oxford Circus nor Wapping neighbourhoods have buildings above 80 m height. Wapping is, unlike Oxford Circus, outside the highest-density areas of London, situated between the City and Canary Wharf areas. The location and surface-altitude data of the reference neighbourhoods are described in Table 7.1.

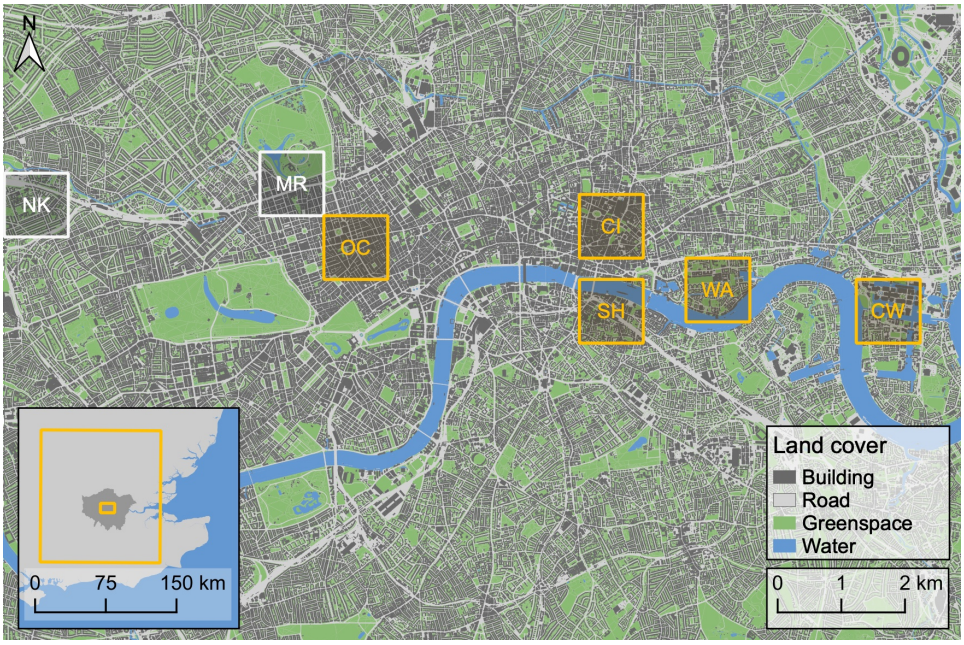

Figure 7.3: Land-cover map of the central London study area with 3 × 3 grid-box neighbourhoods for reference (yellow) and measurement (white) sites. Insert map shows Greater London (dark grey) with central London study area (inner yellow rectangle) and London Model domain (outer yellow rectangle). Land-cover data are supplied from OS MasterMap (Ordnance Survey (GB) 2019b); national (Ordnance Survey (GB) 2005) and Greater London outlines (Ordnance Survey (GB) 2020) are using OS OpenData.

7.2.2 Observations

Automatic LIDAR and Ceilometer (ALC) observations over London from the LUMA network (Grimmond et al. 2021) are used to support the model comparison. ALCs measure the light scattered back from aerosols. The distribution of aerosols in the atmosphere is a result of previous atmospheric mixing, and can therefore be used to characterise boundary-layer dynamics. Vertical profiles of aerosol backscatter are measured at the North Kensington (NK) and Marylebone Road (MR) sites in central London (Figures 7.2c and 7.3) using Vaisala CL31 ceilometers. An automatic algorithm detects the mixed-layer height z_{ML} from the attenuated backscatter profiles (Kotthaus and Grimmond 2018). Kotthaus and Grimmond (2018) report good agreement between z_{ML} inferred from backscatter profiles and mixed-layer

initials	name	Lat, Lon [deg]	altitude [m]
OC	Oxford Circus	51.51, -0.14	36.6
CI	City	51.52, -0.08	33.21
SH	Shard	51.5, -0.08	13.83
WA	Wapping	51.51, -0.06	7.39
CW	Canary Wharf	51.5, -0.02	7.71
LB	Littlebrook Power Station	51.47, 0.24	14.74
NK	North Kensington	51.52, -0.21	25.29
MR	Marylebone Road	51.52, -0.16	35.7

Table 7.1: Description of the reference neighbourhoods and measurement sites of the case study. The location and altitude (above sea level) refer to the grid-box data at the centre of the neighbourhoods.

height inferred from observed temperature inversions for clear-sky summer days. The case study date was therefore chosen accordingly.

7.2.3 Description of model configurations

Three different model runs are compared: (1) the *original* London Model with the current configuration, (2) the *control* run with updated morphology input fields λ_p, λ_f, and z_H derived from the 1 m resolution Ordnance Survey data (Chapter 5), and (3) the *distributed drag* model run with the vertical parameterization of urban drag. Comparisons between (1) and (2) assess the effects of updated urban morphology inputs in MORUSES. Note that the land-cover fractions of the grid boxes have not been updated (since the analysis did not include vegetation and other surface types), and the control run therefore does not represent a fully updated model configuration. This implies that changes to the buildings' plan area and street canyons' aspect ratio are not reflected in the tile-weighting in JULES. Comparisons between (2) and (3) assess the effects of distributing urban drag over several vertical levels. The simulations are also used to assess spatial variability of drag, since urban drag is modelled differently between the two runs. The magnitude of the urban drag is similar between the two cases (see Section 7.2.4).

The output variables that will be compared are the magnitude of the

surface stress, $\tau_0(t,x,y) = \sqrt{\tau_{0,x}^2(t,x,y) + \tau_{0,y}^2(t,x,y)}$, the surface sensible heat flux $Q_H(t,x,y)$, the wind speed $U(t,x,y,z)$ at all vertical model levels, and the mixed-layer heights $z_{ML}(t,x,y)$. The outputs of τ_0, Q_H and U at 10 m are averaged over 15-minute time-intervals. Wind speed at other heights and z_{ML} are instantaneous outputs. A 24-hour timeseries is analysed for each model run, which discards the first six hours as spin-up. Outputs for the measurement sites and 1 km^2 reference neighbourhoods are analysed as 3 $\times$ 3 grid-box averages. The central grid box contains the point of interest (i.e. measurement site or landmark). Note that the location of the data can slightly vary between different output variables, since the Unified Model uses a staggered Arakawa-C grid.

7.2.4 Matching the drag coefficient

The aim of this study is to compare the effects of distributing drag at similar levels of total urban drag, despite the different ways of obtaining $\tau_{0,i}$ in MORUSES and the distributed drag scheme. For this purpose the magnitude of the surface stress τ_0 for the central London study area is matched between the control and the distributed drag run. To achieve this, a suitable drag coefficient c_D for the distributed drag model is estimated using a least-squares fit for

$$c_D = \frac{2\langle\tau_0\rangle}{\rho_0\langle\lambda_f U^2\rangle}, \tag{7.5}$$

with the central London space-averages of surface stress $\langle\tau_0\rangle(t)$ and λ_f-weighted squared wind speed $\langle\lambda_f U^2\rangle(t)$ of the control run. The wind speed is evaluated at the fifth model level at z = 93 m. Since the distributed drag is expected to primarily affect the low level winds, a height sufficiently far away from most buildings is chosen to limit the interference with the effects of the drag scheme. Figure 7.4 shows the c_D data-fit calculated for the 24-hour period of the case date.

A test run of the distributed drag scheme with the resulting drag coefficient c_D = 0.067 was performed, however the space- and time-averaged surface stress over the central London area $\langle\overline{\tau_0}\rangle$ slightly exceeded that of the control run. While the data fit from the control run provides a good approximation on suitable c_D values for the distributed drag run, an exact match is not to be expected because of effects of the distributed drag scheme

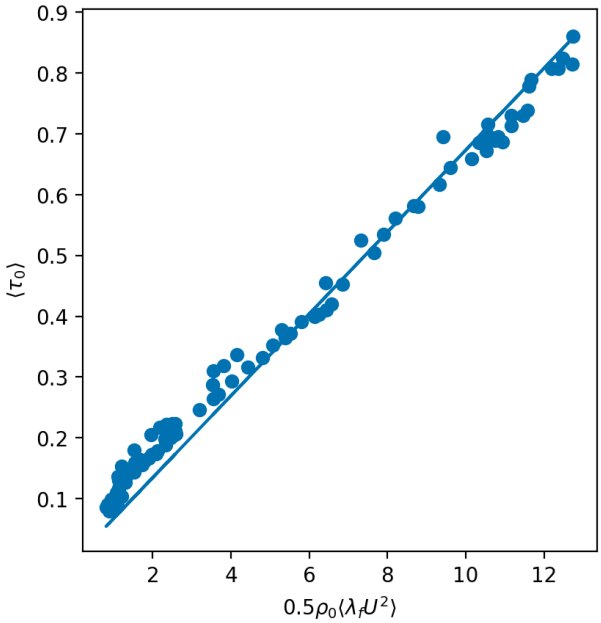

Figure 7.4: Linear regression for estimating the drag coefficient c_D. Central London space-averaged 24-hour data in 15-minute intervals of surface stress $\langle\tau_0\rangle(t)$ fitted to weighted wind speed $0.5\rho_0\langle\lambda_f U^2\rangle(t)$.

on the wind speed. The drag coefficient was therefore re-tuned to $c_D = 0.06$, which yielded an almost exact match in the 24-hour period, where $\langle\overline{\tau_0}\rangle$ of the control and distributed drag run differ by less than 0.01 % (for comparison, $\langle\overline{\tau_0}\rangle$ of the original run is about 13 % lower). The space-averaged surface stresses are also similar over time, which is illustrated by the $\langle\tau_0\rangle(t)$ timeseries for the three model runs in Figure 7.10a (Section 7.3.1). Note that using the least-squares fit (7.5) with the wind speed at the lowest level height (at 2.5 m) instead, the linear regression yields a drag coefficient of approximately $c_D = 1$, an indication of the close link between surface winds and boundary-layer stresses through the implicit coupling of JULES and the atmospheric model component.

We further tested variations of the central London area, which are illustrated in Figure 7.5a. We considered two 10×10 km^2 areas, one including central and south-west London (with the densely built-up area between Hyde Park and the centre; orange outline in Figure 7.5), and the other one including central London and the high-rise Canary Wharf area (pink outline), and

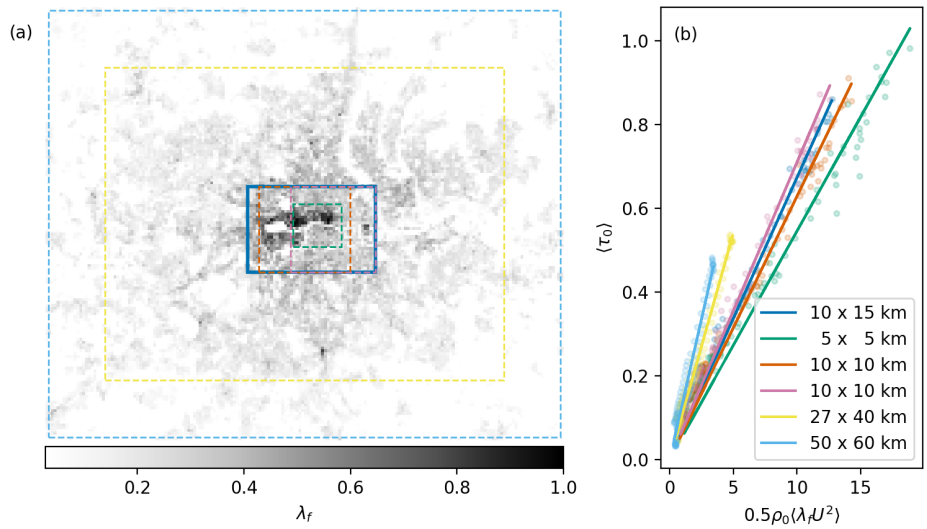

Figure 7.5: Linear regression for estimating the drag coefficient c_D for (a) different areas of the London Model and (b) space-averaged 24-hour data in 15-minute intervals of surface stress $\langle\tau_0\rangle(t)$ fitted to weighted wind speed $0.5\rho_0\langle\lambda_f U^2\rangle(t)$.

further a 5×5 km^2 area of the centre (green outline), an area containing most of Greater London (we defined a 27×40 km^2 area; yellow outline) and all of Greater London (a 50×60 km^2 area; blue outline). The data-fits are shown in Figure 7.5b. Fitting the drag coefficient to these areas yield fairly similar values for the 5×5 km^2 and 10×10 km^2 areas (c_D ranges from 0.05 to 0.07). Larger fitting areas yield a substantial increase in the drag coefficient (0.11 and 0.13). The increase results from lower space-averages $\langle\lambda_f U^2\rangle(t)$, which is mainly due to much smaller values of λ_f outside the most central areas of London. In summary, finding a suitable drag coefficient c_D for the total canopy model (7.4) will depend on the overall model set-up, and the value of $c_D = 0.06$ used in this case study may not be a representative value for other studies.

7.2.5 Changes in the input morphology

The urban morphology input data for the Unified Model are based on land-cover data from the Institute of Terrestrial Ecology (Bunce et al. 1990). The plan area index, frontal area index and mean building height are derived from the urban land-cover fraction F_U of a grid box using empirical relationships

established in Bohnenstengel et al. (2011) and Bohnenstengel and Hendry (2016), with an updated version in Gilham et al. (2020). The empirical polynomial relations are based on high-resolution building data from London (Evans et al. 2006), which are now 15 years old, and urban fractions at 1 km resolution. With λ_p, λ_f and z_H being functions of F_U, the three parameters are linked and the parameter space is reduced to one degree of freedom.

The standard morphology datasets of the London Model are calculated by these empirical polynomials applied to the London Model urban fractions (with a resolution of approximately 333 m). The morphology data of the original run are therefore not only based on relatively old data, but also on an empirical parameter relationship that was established for a different grid resolution. In contrast, the urban morphology datasets of the control run are derived directly from the 1 m resolution Ordnance Survey building data. The control run therefore has a much more accurate representation of the urban morphology than the original run, particularly since many new high-rise buildings have been built in London in recent years. Note that for this case study the dataset may also contain a small number of anachronistic buildings, since the case study is set in June 2018 and the building data originate from April 2019.

Figure 7.6 shows the distributions of the original and new morphology grid-box values λ_p, λ_f, z_H, and $z_{\max}$ in the central London study area. The distributions of the plan area indices λ_p in Figure 7.6a are largely similar, and differ only in the amount of grid boxes for very low building densities (λ_p below 0.1) and around the mean value. The mean value of λ_p decreases from 0.3 to 0.28 with the new data, the maximum value increases slightly from 0.61 to 0.66. The higher original mean is an effect of using the empirical polynomials at the London Model resolution. Higher grid resolutions (i.e. 333 m compared to 1 km grid length) increase the likelihood of having grid boxes that contain only very few buildings. Appendix D shows examples of different grid resolutions for the central London area, where this grid-length dependency for λ_p is clearly noticeable (Figure D.2). The empirical relations based on the 1-km resolution therefore overestimate the plan area index for low values of the urban land-cover fraction compared to the directly calculated values of λ_p. Spatially, the original and new plan area indices of the central London area appear relatively similar overall (Figure 7.7). The

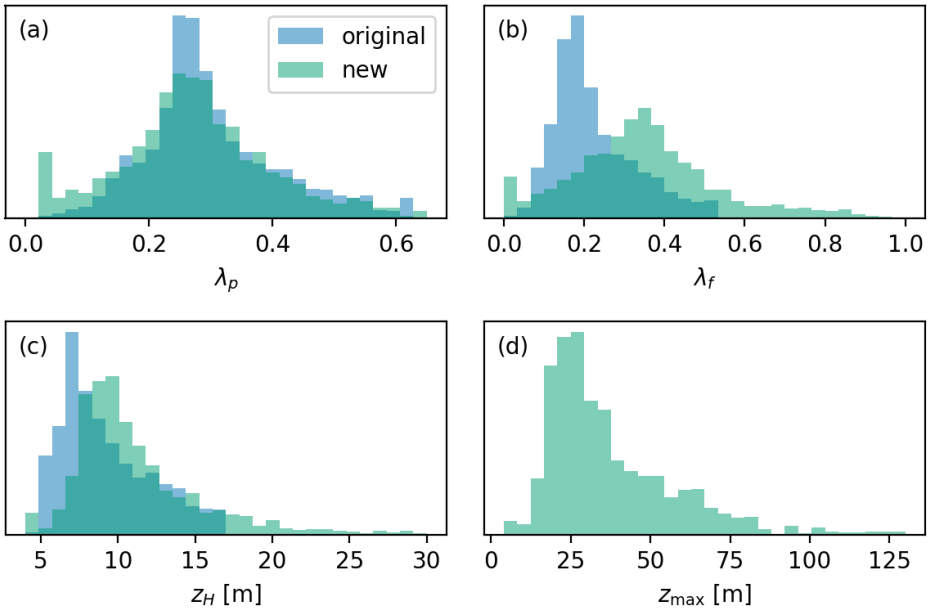

Figure 7.6: Frequency distributions of urban morphology grid-box values in the central London study area. Original (blue) and new (green) data for (a) plan area index λ_p, (b) frontal area index λ_f, (c) mean building height z_H, and (d) maximum building height $z_{\max}$ (new data only).

new data have a larger cluster of high-density grid boxes north of the river Thames; the original data have more individual grid boxes with higher plan area index outside the most densely built-up area.

The new frontal area index distribution in Figure 7.6b is considerably different from the original data distribution, with the mean shifted from 0.22 to 0.35, the maximum value reaching 1.2 (0.5 previously) and a much broader distribution of values. Figure 7.8 shows a striking difference between the original and new frontal area indices of the central London area. The new frontal area indices are higher overall, and much higher in the most densely built-up areas north of the river and around Canary Wharf. Both datasets show low frontal-area indices along the river and at the three large parks in the west. The higher overall values of the new data may partly be attributed to the definition we applied for the frontal area index, which estimates higher frontal areas than other methods (cf. Section 5.1); however the data also clearly reflects the large increase in high-rise buildings in London over the last decades.

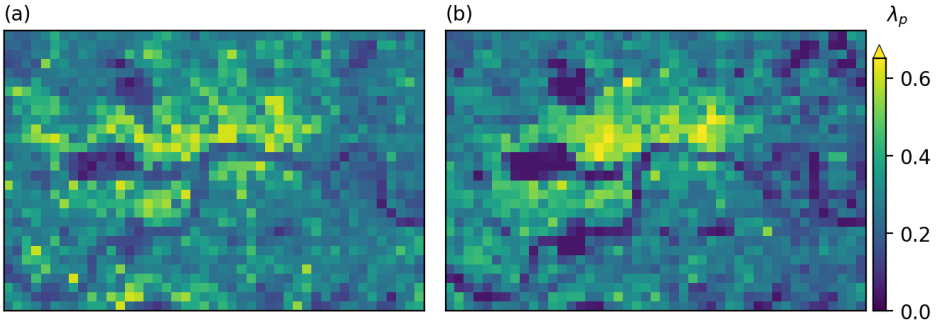

Figure 7.7: Plan area index λ_p of the central London study area from the (a) original and (b) new datasets. For scale see Figure 7.2.

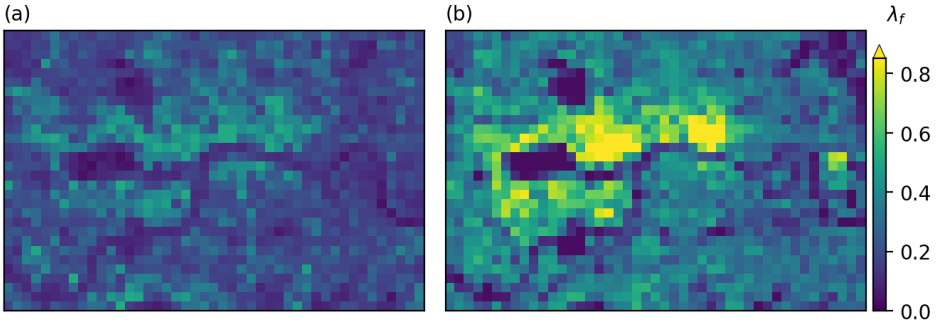

Figure 7.8: Frontal area index λ_f of the central London study area from the (a) original and (b) new datasets. For scale see Figure 7.2.

The original and new data distributions for the mean building height z_H are illustrated in Figure 7.6c. The mean value increases from 9 m to 11 m and the distribution has a longer tail, with more grid boxes with higher mean building heights in the new dataset. The maximum z_H is at 59 m (up from 17 m). Decoupling the mean-height calculations from the urban land-cover fraction results in considerable spatial differences between the original and new z_H data (Figure 7.9). The new data indicate three areas with high average building heights: the City (area around CI neighbourhood), Canary Wharf (area around CW) and a narrow band south of the river (east of Battersea Park) from the Battersea Power Station to Vauxhall. The area around the former Battersea Power Station is currently under development with only a few, but relatively tall buildings being completed. The plan and frontal area indices (cf. Figures 7.7 and 7.8) are therefore below average

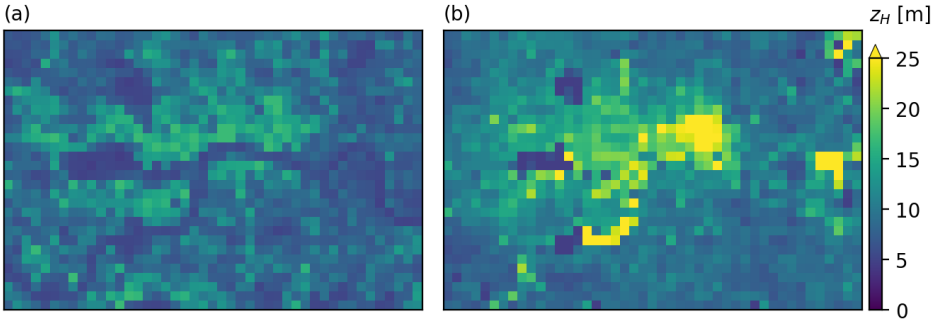

Figure 7.9: Mean building height z_H of the central London study area from the (a) original and (b) new datasets. For scale see Figure 7.2.

in this area. Contrary to the original data (which are linked to the urban fraction), the new z_H data do not indicate the location of the river; this is because grid boxes that are primarily occupied by the river also contain some buildings and therefore have average values for which reflect this mix. The distribution of the new input parameter $z_{\max}$ in Figure 7.6d is of comparable shape to the z_H distribution of the new data. The mean is at 39 m and the maximum at 304 m.

Table 7.2 lists the new morphology values for the centre grid box of the selected neighbourhoods and measurement sites. Table 7.3 indicates the relative difference to the old values. The tables also show the maximum to mean building-height ratio discussed in Chapter 5, and displacement height and roughness length as calculated by MORUSES using the MacDonald et al. (1998) parameterization.

7.3 Results from the case study

This section compares results from the three different model runs: the original run with the standard LM set-up, the control run with updated urban morphology data, and the distributed drag run with the new parameterization.

7.3.1 Surface stresses

Figure 7.10 shows the magnitude of the surface stress τ_0 for the central London area. The space-averaged $\langle\tau_0\rangle(t)$ are largely similar over time for

	λ_p	λ_f	z_H [m]	$z_{\max}$ [m]	$z_{\max}/z_H$	z_d [m]	z_0 [m]
OC	0.58	0.81	18.78	37	1.97	15.49	0.84
CI	0.53	0.85	27.19	202	7.43	21.48	1.69
SH	0.5	0.54	19.86	304	15.3	15.19	1.09
WA	0.26	0.35	10.23	59	5.77	5.09	1.49
CW	0.27	0.69	54.5	200	3.67	27.89	10.9
LB	0.33	0.22	22.32	211	9.45	13.23	1.6
NK	0.27	0.37	10.74	34	3.17	5.52	1.55
MR	0.27	0.33	14.77	43	2.91	7.66	1.95

Table 7.2: New urban morphology data $\lambda_p, \lambda_f, z_H$, and $z_{\max}$, building-height ratio $z_{\max}/z_H$, and aerodynamic roughness parameters z_d and z_0 calculated from MacDonald et al. (1998) for the centre grid box of selected neighbourhoods.

the three model runs, but the surface stress of the original run is consistently less than the other two model runs (Figure 7.10a). Spatially, the surface stresses have large variations over the central London area for the 24-hour time averaged $\overline{\tau_0}(x, y)$ fields (Figure 7.10b–d).

In the original model run (Figure 7.10b), surface stresses across urban areas are relatively uniform and the spatial structure of London is only visible through the lack of urban characteristics (i.e. large parks and the river). High surface stresses in the control run (Figure 7.10c) occur in the Canary Wharf area. Higher stresses than in the original run also occur in areas with comparatively low building density in south-west London. Open areas such as the river are not evident. The distributed drag run (Figure 7.10d) has high surface stresses for Canary Wharf, the City, and over the most densely built-up area in the centre of London. Distinctively low stresses are found at the parks and river. Overall, the spatial variability of surface stresses is largest with the distributed drag model and include the full range of local features (built-up areas, high-rise building clusters, parks, and the river), such that the spatial patterns reflect the heterogeneity of the urban area.

The spatial variability between the different model runs comes from changes in morphology inputs and the different parameterizations for the surface stress (Equations 6.8 and 7.4). The surface stresses of the distributed drag run correlate with the frontal area index λ_f (cf. Figure 7.8b), which

	λ_p [%]	λ_f [%]	z_H [%]	z_d [%]	z_0 [%]
OC	12	86	23	30	33
CI	30	157	115	149	105
SH	21	60	56	74	34
WA	-7	75	20	13	99
CW	8	315	650	696	1593
LB	92	92	272	512	185
NK	11	131	51	63	144
MR	9	97	100	113	199

Table 7.3: Relative difference of the new urban morphology data $\lambda_p, \lambda_f, z_H$, and $z_{\max}$ and new aerodynamic roughness parameters z_d and z_0 compared to original data for the centre grid box of selected neighbourhoods.

results from incorporating λ_f in the distributed drag model (Equation 7.4). The momentum roughness length z_0 is the key element of the standard momentum-exchange parameterization (Equation 6.8). Figure 7.11 shows the spatial and frequency distributions of the momentum roughness length z_0, as calculated by MORUSES using the MacDonald et al. (1998) parameterization from the original and new morphology datasets. The original values of z_0 are concentrated between 0.5–1 m and have little spatial variability. Non-urban features such as the parks and the river are most distinct. Roughness lengths from the new morphology inputs are higher and values have a wider range. In Canary Wharf, z_0 reaches a maximum of 12 m. The river can no longer be identified as a result of spatial changes in the mean height (through decoupling of z_H from the urban land-cover fraction).

The roughness length data is most strongly correlated to the mean building height z_H. The MacDonald et al. (1998) parameterization relates z_0 primarily to z_H, where λ_p and λ_f give a weighting to the mean building height. The proportion of z_H is higher for low values of λ_p and λ_f, or low values of λ_p and high values of λ_f (cf. Figure 6.1b). This weighting is the reason for the extremely high values of z_0 around Canary Wharf and the Battersea development site in the new dataset. Roughness length values that are ten times higher than typical for urban areas seem to be a gross overestimation; although there are almost no measured values in high-rise

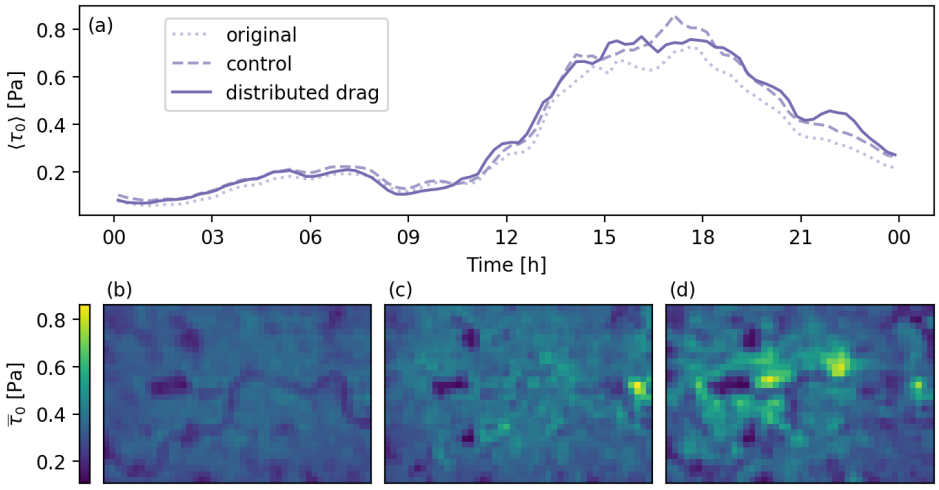

Figure 7.10: Surface stress τ_0 for the central London area. (a) Space averaged $\langle\tau_0\rangle(t)$ timeseries with original (dotted line), control (dashed line) and distributed drag run (solid line). 24-hour time averaged $\overline{\tau_0}(x, y)$ fields with (b) original, (c) control and (d) distributed drag run. For scale see Figure 7.2.

areas to say this with any certainty (Grimmond and Oke 1999). The strong correlation to the mean height is also the reason why there are no longer any distinctively low z_0 values along the Thames in the new dataset.

More accurate urban morphology does not automatically yield better roughness length estimations. On the contrary, the mean height that is coupled to the urban fraction gives a clearer distinction between urban and non-urban neighbourhoods, and although more realistic z_H values produce a wider range of roughness lengths, they also have extreme outliers. These differences suggest the possibility of a limit on the applicability of MacDonald et al. (1998), such that the model is less appropriate for high-resolution models like the LM.

Figure 7.12 shows the timeseries of surface stresses $\tau_0(t)$ for selected neighbourhoods. Higher surface stresses for Canary Wharf (control and distributed drag), the City (distributed drag), and Oxford Circus (distributed drag) are examples of the model behaviour discussed above. In Wapping, which is outside the highest-density areas of London, the surface stress of the distributed drag is below the control run with the updated morphologies. The tall chimney of Littlebrook Power Station is only represented in the

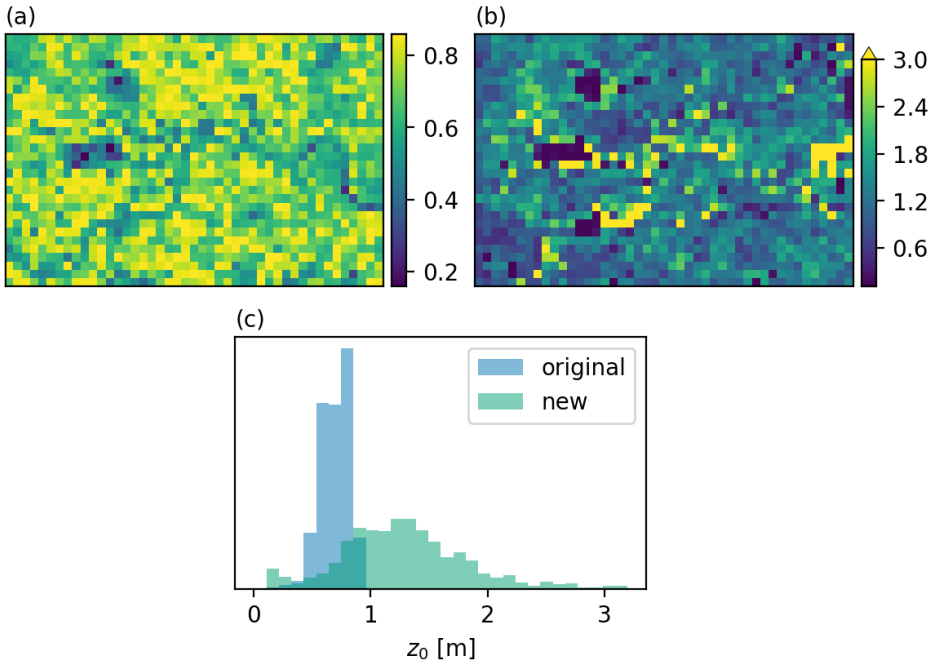

Figure 7.11: Momentum roughness length z_0 of the central London study area from the (a) original and (b) new datasets calculated by MORUSES using the MacDonald et al. (1998) parameterization, and (c) frequency distribution of the data values. Note that the fields in (a) and (b) are shown with a different colour range. For length scale see Figure 7.2.

urban morphology of the control run and distributed drag run, but not in the original run. However, the surface stresses at Littlebrook Power Station are similar for all three model runs, suggesting that a single tall structure in a low-density urban area has little effect on the surface stress in both the MORUSES scheme and distributed drag scheme. Note however that the tile fractions in the control run have not been updated, and the urban (canyon and roof tile) roughness lengths have therefore less weight in the grid-box average than they would have under a fully updated model configuration.

7.3.2 Wind speed

Figure 7.13 shows the wind speed $U(t)$ at 10 m above ground level for the reference neighbourhoods. At this height, the wind speeds from the different model runs differ considerably. Wind speeds of the original run are

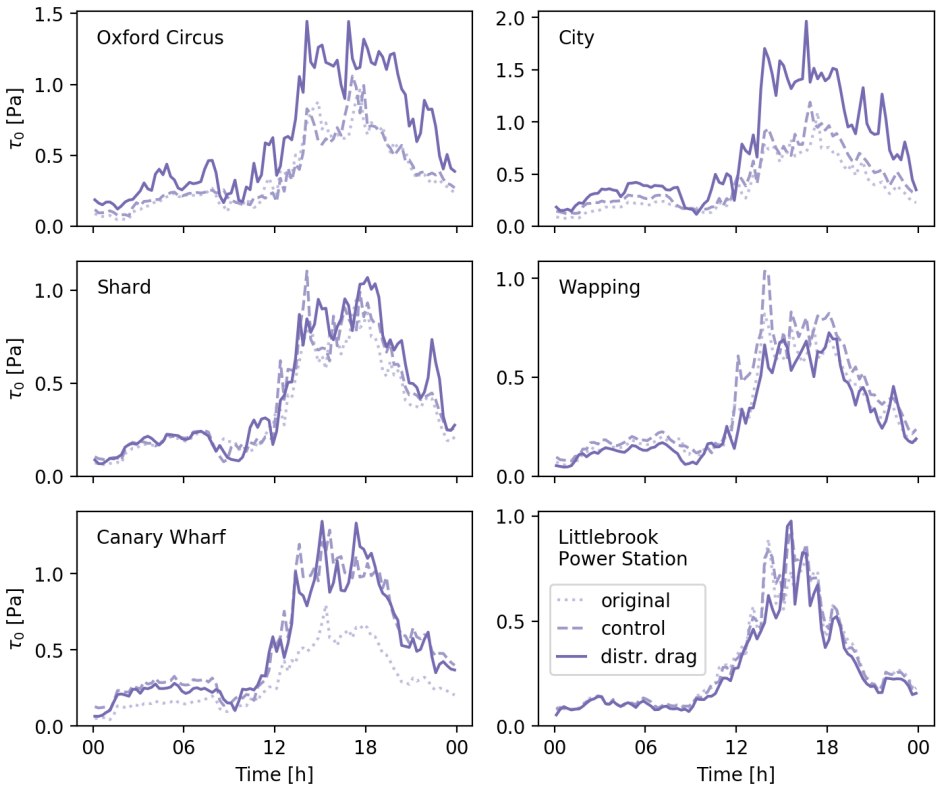

Figure 7.12: Surface stress $\tau_0(t)$ for selected neighbourhoods with original (dotted line), control (dashed line) and distributed drag run (solid line). The profiles are 3 $\times$ 3 grid-box averages.

generally higher than the control run, which shows the effect of lower surface friction in the original run. The distributed drag and control run have comparable wind speeds in the lower-density neighbourhoods of Wapping and Littlebrook Power Station, but larger differences at the other neighbourhoods. In the second half of the day, the distributed-drag wind speeds are generally lower than the wind speeds of the other two model runs. At these times, surface stresses are also higher (particularly Oxford Circus and the City, cf. Figure 7.12). Only at Canary Wharf, the control-run wind speeds are consistently lower than the distributed drag run.

Vertical profiles of wind speed $U(z)$ at 19:00 UTC for the reference neighbourhoods illustrate representative features of the different model runs (Figure 7.14), because vertical mixing through convection is lower than during times of the day where solar radiation is stronger. The wind profiles of

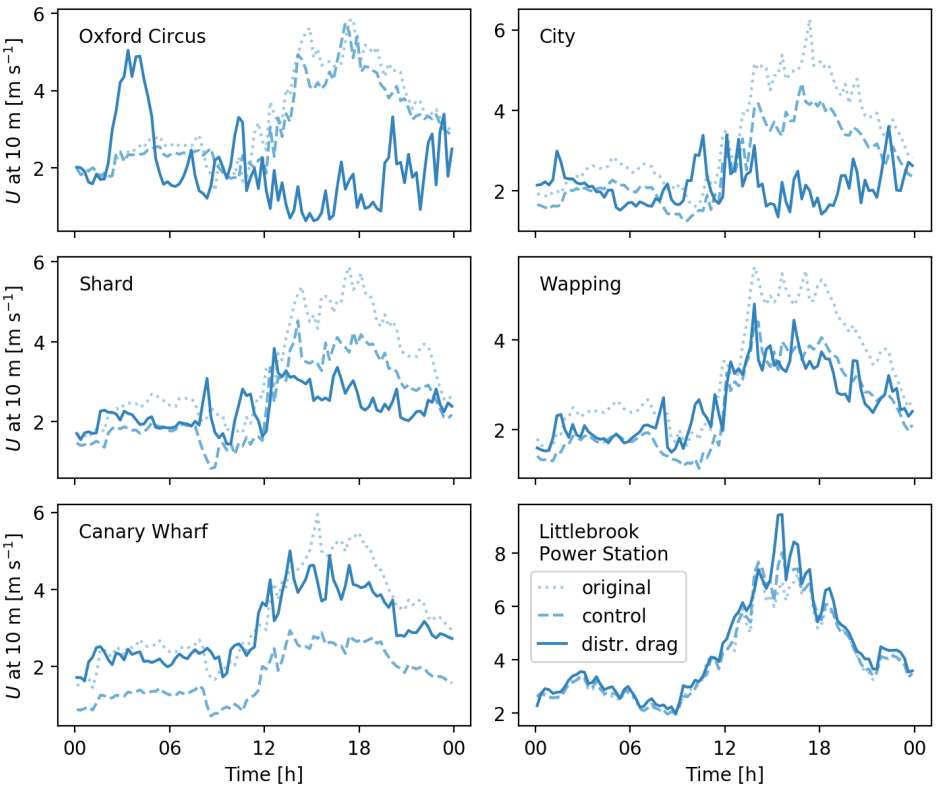

Figure 7.13: Timeseries of wind speed $U(t)$ at 10 m height for selected reference points with original (dotted line), control (dashed line) and distributed drag run (solid line). The profiles are 3 × 3 grid-box averages.

the original and control run are relatively similar at all neighbourhoods and have the typical boundary-layer profile of air flowing over a flat surface. The wind-speed profiles with the distributed drag scheme are much more diverse. The City and Oxford Circus differ the most in the lower model levels compared to the other neighbourhoods. The distributed-drag wind profiles change gradually in height as the wind speeds in the lower vertical levels are lower. Wind speeds become similar to the other two model runs at several hundred metres above the ground.

At Canary Wharf, the large difference in surface stress between the original and control run is reflected in the data from lower model levels, where the control-run wind speed is smaller than the original run. At similar surface stress, the height-distribution effects of the distributed drag scheme become apparent, with velocities near ground level higher than in the control

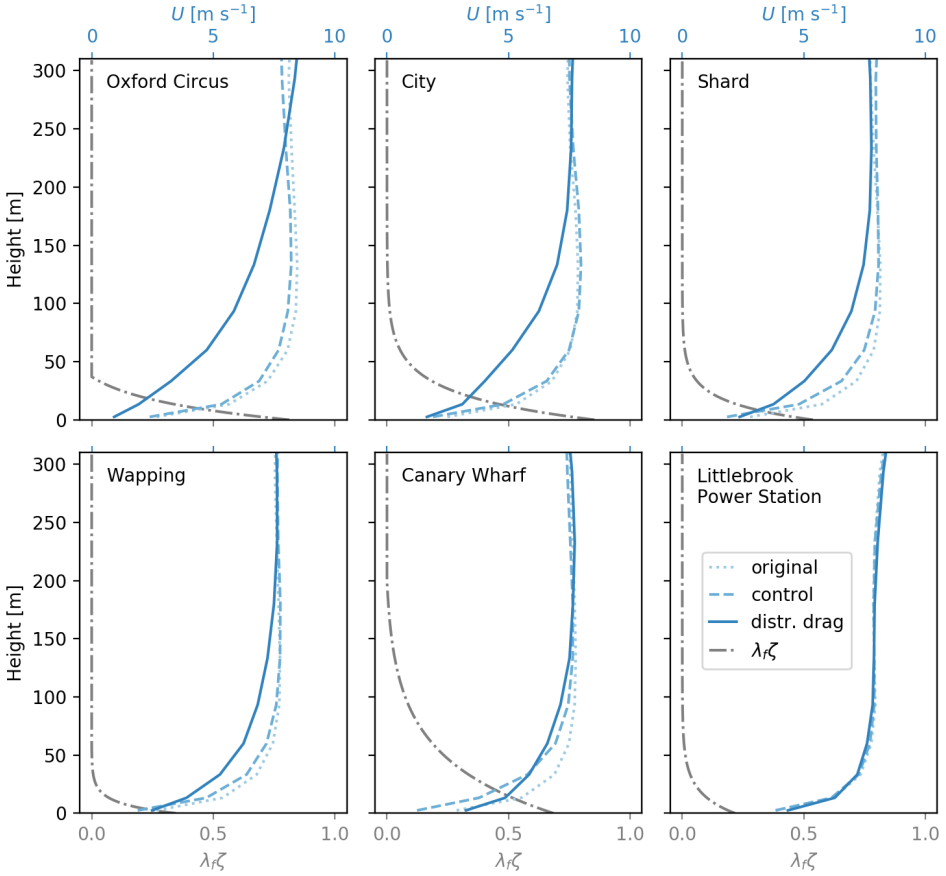

Figure 7.14: Vertical profiles of wind speed $U(z)$ at 1900 UTC for selected neighbourhoods (Figure 7.2) with original (dotted line), control (dashed line) and distributed drag run (solid line). The profiles are 3 × 3 grid-box averages. Frontal area index function $\lambda_f\zeta(z)$ for the centre grid box of the neighbourhood (dashed dotted line).

run, but below the control-run velocities between approximately 50–100 m. No significant differences between the model runs are evident for the isolated tall chimney of the Littlebrook Power Station.

The frontal area index function $\lambda_f\zeta(z)$ for the centre grid box of each neighbourhood illustrates the different underlying building representations of the drag model (Figure 7.14). The effects of distributed drag can go beyond the height of the parameterization ζ, as the Oxford Circus case illustrates. The maximum building height at the centre grid box is is 37 m, but the distributed-drag wind speed does not approach the speed of the

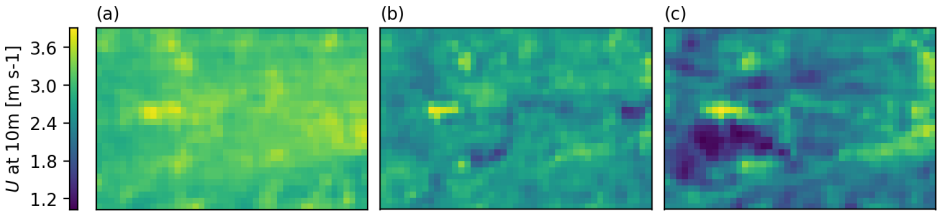

Figure 7.15: Central London 24-hour time-averaged wind speed $\overline{U}(x, y)$ at 10 m for (a) original, (b) control and (c) distributed drag run. For scale see Figure 7.2.

other model runs until 250 m. The high-density urban surroundings of Oxford Circus are likely to be contributing to the large effects on the wind.

Indeed, the effect of large-scale urban areas under the distributed drag scheme is evident in Figure 7.15, which shows 24-hour time-averaged wind-speed fields $\overline{U}(x, y)$ at 10 m for the central London area. The distributed-drag run shows relatively high average wind speeds to the east side of the study area (Figure 7.15c), where easterly winds with high wind speeds along the Thames estuary approach central London. A large wake with low average wind speeds is found downwind of the city centre to the west. This spatial pattern suggests that local disturbances introduced by the distributed drag are advected and grow vertically in the downstream direction, forming an internal boundary layer. Therefore, with an easterly wind, a neighbourhood downwind of the city centre such as Oxford Circus experiences large impacts of the distributed drag model.

In contrast, the spatial patterns of the original and control run resemble largely the patterns of the surface stresses (cf. Figure 7.10). The original run has higher average wind speeds at the parks and river, where friction is smaller, and the control run has particularly low wind speeds around Canary Wharf and south-west London, where friction is high (cf. Section 7.2.5). But there is little evidence in the 10-m wind field of any extended wake regions, or the growth of internal boundary layers.

These differences between the distributed drag and the other runs relate back to the question of which height the model surface represents (cf. discussion in Section 6.3.3). If 10-m model height in the original and control run is interpreted as 10 m above $z_d + z_0$, then any wake would be below this height and therefore does not appear in these fields. However, given

the large values of displacement height above urban areas, it is inconsistent to not address this height change in the model (e.g. by adding $z_d + z_0$ to the surface altitude). At the same time, since also the differences between neighbouring grid boxes become larger with increasing resolution (particularly the displacement height, see Figure D.9 in Appendix D), this poses the question whether such different surface conditions can at all be incorporated into the model in a meaningful way (think of the 10-m model height representing wind at 40 m above ground level in Canary Wharf and wind at maybe 5 m in the neighbouring grid box, and the horizontal exchange between these grid boxes). As it stands, the buildings are currently 'buried' in the ground. The distributed drag scheme in contrast provides a consistent modelling approach, where building effects are represented at their true height, and the wind speed at 10 m has the unambiguous interpretation of 10 m above ground.

Figure 7.16 shows the change between the control and distributed drag run for space-averaged wind speed $\langle U \rangle(t, z)$ in the central London area, giving a direct comparison between the standard parameterization and the distributed drag scheme. This shows that, with distributed drag, wind speeds are considerably higher at the lowest model level, but tend to be lower for the model heights just above the lowest level and up to several hundred metres. The distributed drag model increases the central London averaged wind-speed at the lowest level often by more than 50 %. A band of higher wind speeds on top of lower winds in the morning hours suggests a lower boundary-layer height for the distributed drag run at these times. This is probably related to a reduction in the sensible heat flux (Section 7.3.3). At other times, there is no clear trend above the lowest few hundred metres and the relative difference becomes smaller at higher levels. This suggests that the overall impact of distributed drag on the boundary layer is relatively small.

7.3.3 Mixed-layer height

Roughness and thermal effects of urban areas generate turbulence which induces vertical mixing in the atmosphere. The height of the mixed layer z_{ML} above cities is therefore an indication of how much turbulence is generated by surface processes. The model mixed-layer height is determined as the max-

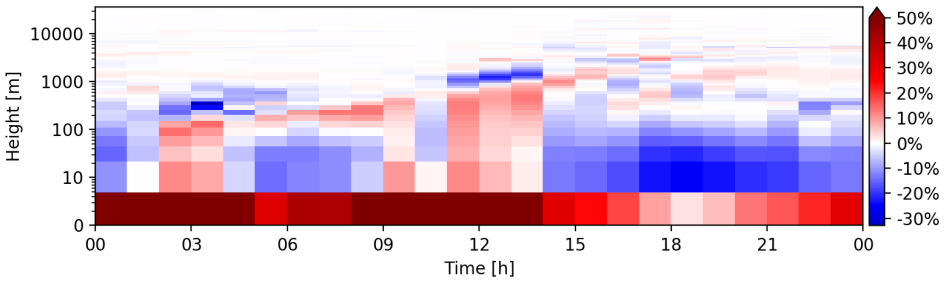

Figure 7.16: Change in central London space-averaged wind speed $\langle U \rangle(t, z)$ between control and distributed drag run. Note that the height axis is logarithmic except near the surface, and the colour scale is capped at 50 %, which is exceeded in the lowest model height level.

imum of the surface-based mixed-layer height, which is the depth through which a positively buoyant parcel released at the surface would ascend, and the boundary-layer depth diagnosed by a threshold for the Richardson number, which marks the transition to the stable conditions of the capping inversion (Lock et al. 2020).

In this section model mixed-layer heights are evaluated against mixed-layer heights estimated from ALC observations of aerosol-backscatter data. The observed mixed-layer heights at the two measurement sites in central London are largely similar in the morning and afternoon, and differ somewhat at their maximum height at midday. Reasonably good agreement between the observed and modelled mixed-layer heights is found, but the observations suggest that all simulations underestimate z_{ML} (Figure 7.17). However, z_{ML} of the distributed drag run are below those of the original and control run for the day investigated in this study. A typical error estimate for a measurement is around ± 10 m, thus much smaller than the difference between observations and modelled z_{ML}.

The lower mixed-layer height in the distributed drag run is likely caused by an underprediction of the surface sensible heat flux Q_H. Recall that Q_H is modelled as a function of the surface heat-exchange coefficient C_H, the lowest model-level winds, and temperature differences between the surface and the lowest model level (Equation 6.11). The distributed drag scheme yields higher velocities than the standard MORUSES parameterization at the lowest level, however, the surface exchange coefficient C_H is based on the

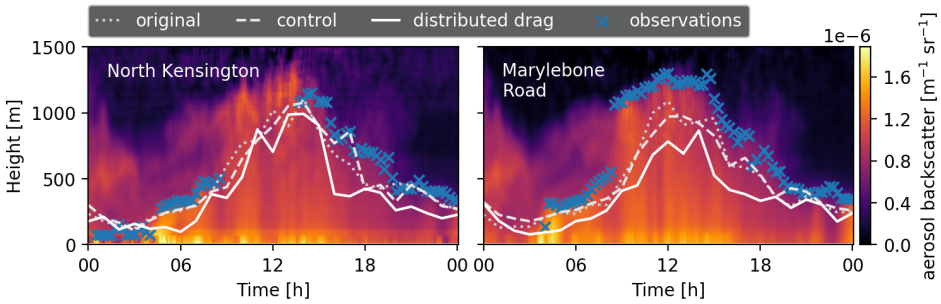

Figure 7.17: Aerosol backscatter and mixed-layer height observed at the measurement sites (markers) and hourly model mixed-layer height of the original (dotted line), control (dashed line), and distributed-drag run (solid line). The model data are 3 × 3 grid-box neighbourhood averages around the measurement site (Figure 7.2).

heat roughness length and the altered momentum roughness length $z_0 = \epsilon$ (cf. Figure 7.1), and C_H is therefore much lower than in the control run. As a result, surface sensible heat fluxes throughout the day are greatly reduced compared to the standard scheme. For example, sensible heat fluxes at the Shard, Wapping, and Canary Wharf are reduced to half at midday (Figure 7.18). A smaller but significant reduction is also found at Oxford Circus and the City. Night-time sensible heat fluxes are more alike and can be even slightly higher in the distributed drag run (e.g. at Oxford Circus). Figure 7.19 shows afternoon and evening time-averages of the surface sensible heat flux $\overline{Q_H}(x, y)$ for the central London area. The figure demonstrates the large day-time reduction of the surface sensible heat flux in the distributed drag run compared to the original and control run, while night-time Q_H is approximately similar between distributed drag and control run.

7.4 Discussion

Comparison of the model behaviour of three different configurations (standard model set-up with original and updated morphology inputs, model with distributed drag implementation) has shown profound effects in the lower levels of the atmospheric boundary layer. Spatial variations in the surface stresses highlight the importance of the urban morphology inputs and modelling decisions. Originally, plan area index, frontal area index, and mean

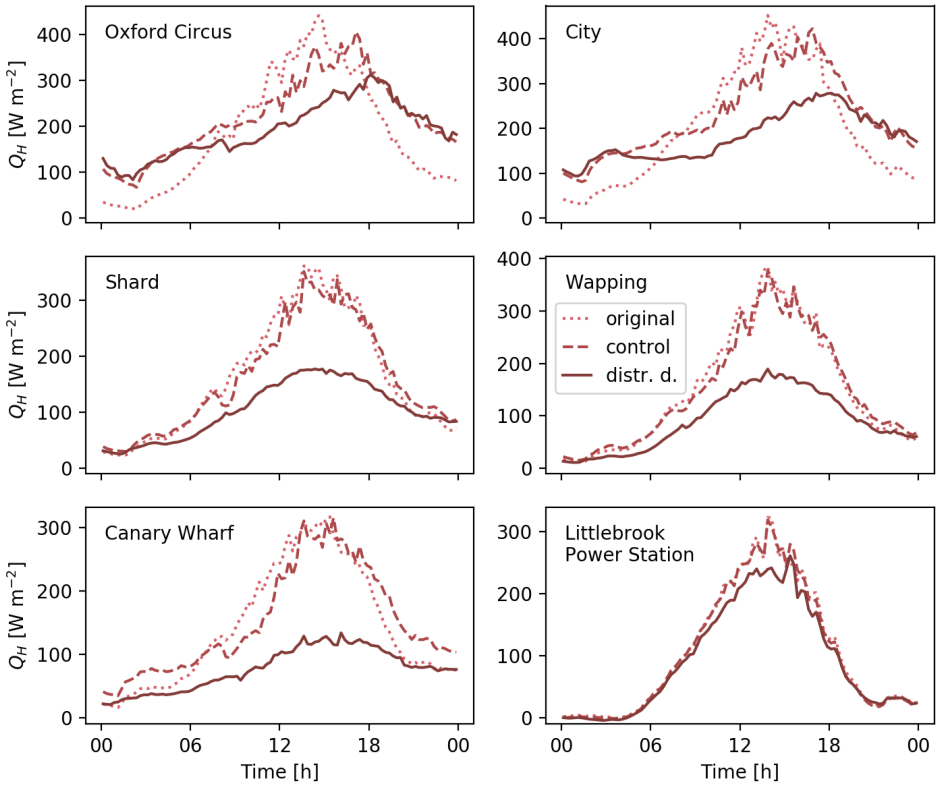

Figure 7.18: Surface sensible heat fluxes $Q_H(t)$ at selected neighbourhoods for original (dotted line), control (dashed line) and distributed-drag run (solid line). The timeseries are 3 × 3 grid-box neighbourhood averages.

height were all dependent on the urban land-cover fraction of the grid boxes. After decoupling these parameters, regions with high-rise buildings experience higher surface stresses, but other local distinctions like the Thames river disappear. The surface stresses under the distributed drag parameterization show entirely different spatial patterns, with more emphasis on densely built-up areas with a large frontal area index. These differences suggest the possibility of a limit on the applicability of the MacDonald et al. (1998) parameterization such that, at high horizontal resolution, a bluff-body modelling approach (i.e. one that considers frontal areas) may become more appropriate. Further research is required on this subject.

The distributed drag scheme strongly affects the wind in the lower atmospheric levels and causes much more variation in the wind speed over central London than the standard parameterization. The friction gener-

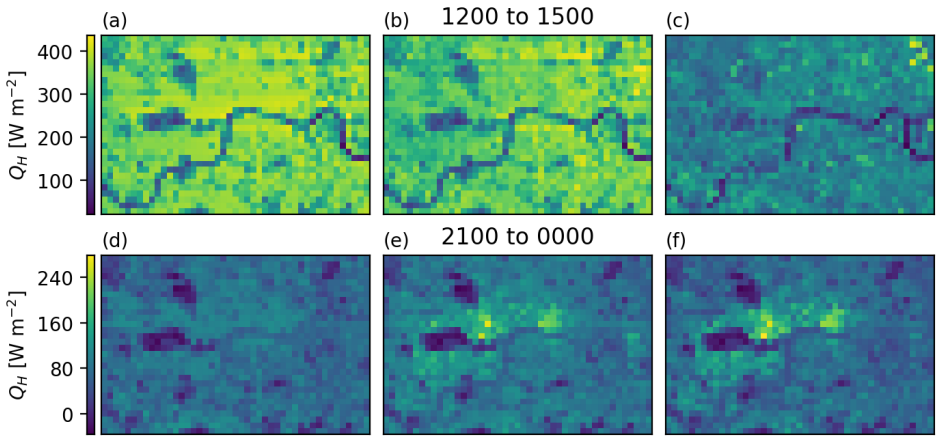

Figure 7.19: Time-averaged sensible heat fluxes $\overline{Q_H}(x, y)$ of the central London area. Afternoon average 1200 to 1500 UTC (a–c) and night average 2100 to 0000 UTC (d–f) for original (a, d), control (b, e) and distributed-drag run (c, f).

ated by clusters of high-rise buildings cause extensive wakes that reduce wind speeds over extended areas downstream, and the perturbations also grow in the vertical direction. However, the surface sensible heat fluxes are under-predicted with the current implementation of the distributed drag scheme, which can affect the height of the boundary layer. Note that a similar conclusion was drawn for the distributed orographic scheme in a study on inland water (Rooney and Bornemann 2013): while the distributed orographic drag produces more realistic low-level winds than the orographic roughness scheme, it also produces unrealistic lower temperatures with the current model physics settings in JULES. In order to obtain accurate predictions of sensible heat fluxes with the current model, a re-calibration of the scalar exchange coefficients would be required.

However, these effects are the symptom of an underlying mismatch: while the form effects of the buildings are modelled at the height of their impact, the material effects of the buildings are still imposed as boundary conditions at ground level. A consequent re-parameterization of urban areas would ultimately need to represent both the drag and scalar (heat, moisture) exchange in a distributed manner, taking into account that momentum- and scalar-exchange are intrinsically coupled.

8

Conclusion

The aim of this thesis was to develop a parameterization for drag that better represents the heterogeneity of urban environments in numerical weather prediction models. Urban flow of neighbourhoods with heterogeneous building morphology was investigated using large-eddy simulations. Findings from the flow-structure analysis were translated to a distributed drag parameterization of urban environments. A forecasting run of the entire region of Greater London showcased the city-scale effects of the new drag parameterization and demonstrate potential improvements to urban weather forecasting. The following sections provide a summary of the research contributions of this thesis (Section 8.1) and draw the main conclusions from analysing numerical simulations on neighbourhood- and city-scale (Section 8.2). Potential for future work resulting from this study is outlined in Section 8.3.

8.1 Summary of contributions

Climate-related challenges for cities and their population are manifold. They reach from dealing with severe weather hazards like heat waves, water stress, flooding, and dangerously high air pollution, to managing the transition to sustainable resource consumption and climate-change resilient infrastructure. Urban climate modelling helps in addressing these challenges, and the increasing resolution of numerical weather prediction models to sub-

kilometre scale allows for modelling urban weather at unprecedented detail. For that, an accurate representation of the urban built-up environment is necessary. In the current models, buildings are figuratively 'buried in the ground', since their effects on the atmosphere are modelled at ground level. A model representation that raises buildings to their actual height-levels is required to make full use of the advantages of higher resolutions, particularly given the now numerous and fast growing number of high-rise buildings in cities worldwide. In the scope of urban planning and climate-adaptations, a better representation of buildings has implications for the study of pedestrian comfort, building design, and energy usage, by improving the modelling of wind, heat, and pollution transport.

Neighbourhood scale The first part of the study described in this thesis focused on urban flow on neighbourhood scale (Chapters 3 and 4). Numerical experiments with large-eddy simulations were set out to investigate the role of the urban form within morphologies that would be represented in an identical way by most existing urban parameterizations. Nine different urban morphologies were designed that have similar surface-cover parameters, but vary in complexity with different building heights, plan areas, and street geometries. The morphologies have identical buildings' plan- and frontal-area indices, which implies that the same scaling of mean building height is used to approximate the morphologies' roughness length (e.g. in the MacDonald et al. (1998) parameterization).

Analysis of mean-flow- and turbulence-structures showed a large spread between the different morphologies, and indicated that the height extent and height variability play an important role in shaping the flow: The mean-wind profiles of simulations with non-uniform building heights are evidently distinct from simulations with uniform building heights, and a high variation in estimated logarithmic wind profiles below the height of $2z_{\max}$ suggest that log-profiles are not suitable to represent wind velocities of heterogeneous morphologies at these heights. At equal average wind speed, the total urban drag varies as much as almost a factor two between a uniform and strongly heterogeneous morphology, and the variations in drag and estimated roughness parameters between the different morphologies are strongly correlated to the maximum building height rather than the average height.

Neither the MacDonald et al. (1998) nor Kanda et al. (2013) roughness parameterizations were able to adequately capture the large spread observed in the simulation data.

The key step for translating these findings into a model for drag was to describe urban morphology as a height-dependent profile, by using a new normalised frontal area function $\zeta(z)$, rather than a scalar parameter. With the framework for quantifying drag in a distributed manner (Chapter 2) and the distributed morphology profiles $\zeta(z)$, a drag parameterization was developed that used a third-order polynomial function of the morphology profile in ζ.

City scale The second part of the thesis studied how urban areas in numerical weather prediction are represented by this novel modelling approach. A case study was set up to investigate effects of the new drag parameterization in a forecast run over Greater London. Vertical morphology profiles $\zeta(z)$ were calculated for the entire London region at high horizontal resolution. Analysis showed that the profiles could be accurately approximated by an exponential distribution with the building-height ratio $z_{\max}/z_H$ as grid-box parameter, such that they can be included in a numerical weather prediction model (Chapter 5). The total urban canopy drag τ_0 in the parameterization was based on a model by Coceal and Belcher (2004) and Belcher (2005) with the grid-box frontal area index λ_f as scaling parameter. The new parameterization models the aerodynamic effects of buildings as a body force directly within the governing equations and thus dependent on height, rather than as boundary condition to the horizontal wind velocities at ground level.

The case study with the Met Office's high-resolution London Model demonstrated substantial changes to the lower levels of the atmospheric boundary layer compared to the standard surface-exchange scheme (Chapter 7). The simulation showed increased horizontal spatial variability in total surface stress τ_0, such that the diverse range of local morphology features (densely built-up areas, high-rise building clusters, parks, and the river) are clearly distinct. Vertical effects included heterogeneous wind profiles analogous to the profiles from the neighbourhood-scale simulations, extended building wakes on the downwind side of dense neighbourhoods, and perhaps also the formation of internal boundary layers.

8.2 Conclusions

Lifting buildings from the ground The findings from this study challenge the common practise in NWP to model urban areas as boundary condition to the atmosphere at ground level. First, standard parameterizations used in NWP implicitly assume simple and uniform morphologies, but the LES results showed that wind profiles of heterogeneous morphologies differ substantially from the profiles of homogeneous urban neighbourhoods. Second, we highlighted practical challenges with implementing paramterizations that account for heterogeneity into current urban surface schemes (Chapter 6). Third, characterising the morphology of London revealed a large amount of variation (e.g. $z_{\max}/z_H$ ratios reaching from 1 to 17), exposed that buildings in urban areas are generally much taller than the height of the lowest atmospheric level, and that some areas in central London have buildings protruding into the atmosphere as far as the ninth vertical level. Fourth, we presented a height-dependent parameterization for urban drag that is relatively easy to implement (it requires just one additional input parameter, the maximum building height $z_{\max}$) and showed potential for improved wind modelling across the entire urban boundary layer.

However, the model is far from complete: further research is required on how to approximate the total canopy drag τ_0; the distribution function for drag (i.e. the polynomial $s(\zeta)$) is only based on neutral stability and a limited set of numerical simulations and therefore needs further investigations; and most importantly it does not address the distribution of scalars (heat and moisture), even though momentum- and scalar-transport are intrinsically linked. Nevertheless, the model is a novel approach to represent height-distributed building drag and it is the first implementation in the Met Office Unified Model where building effects have risen from the ground to the real height of their occurrence. It hopefully inspires further research into modelling urban areas in a distributed manner.

Urban heterogeneity Much of the complexity of urban climates arises from heterogeneity within and across scales. For instance, various building shapes and street layouts within urban neighbourhoods form heterogeneous morphologies. The flow characteristics of different heterogeneous morpho-

logies may differ considerably, and that in turn leads to spatially varied and complex flow patterns across the entire city, where the individual heterogeneous neighbourhoods blend into a heterogeneous urban landscape. The urban boundary-layer flow is not just the aggregated flow over each neighbourhood, but crucially depends on interactions between the neighbourhoods, such that more profound effects are found downwind of agglomerations of densely built-up neighbourhoods with highly variable buildings. The case study with London's morphology has shown that very few neighbourhoods are completely uniform, and that if heterogeneity on the smaller neighbourhood scale is represented, heterogeneous flow on the larger city scale can unfold.

However, urban heterogeneity is difficult to quantify. This study set out to explain the flow response and total magnitude of urban drag in terms of the heterogeneity of different morphologies. The Urban Landscape Generator was created to manage aspects of heterogeneity related to the urban form on neighbourhood scale. The ULG facilitates investigating morphologies of intermediate complexity, such as in the presented study on the effect of subgrid heterogeneity in NWP models (heterogeneous layouts with similar morphology representation). However, the study was yet unable to identify a unique parameter linked to the flow response of the different morphologies, and it therefore does not offer a conclusive answer to the question of how heterogeneity of urban form ought to be characterised. The study does however add to the growing evidence in literature that building-height variability is an important aspect of urban flow that requires explicit consideration (e.g Xie et al. 2008; Millward-Hopkins et al. 2011; Kanda et al. 2013; Kent et al. 2017; Fuka et al. 2018; Hertwig et al. 2019), and offers a new approach to include height variability in urban parameterizations.

Vertical profiles of urban environments The urban morphology profiles introduced in this study, the buildings' total width $L(z)$ and normalised frontal area $\zeta(z)$, embrace the height-variability of urban areas. The results from the case study suggest that these profiles are able to model aerodynamic effects that are not represented by surface-based parameterizations (e.g. wakes extending over several grid boxes, internal boundary layers). Also radiative processes are inherently height-dependent: on one side, the

height of large surface areas (such as building roofs) is important for absorption and reflection of radiation, on the other side, there are complex interactions of shadowing effects and trapping of longwave radiation within the street canyon (cf. Theeuwes et al. 2014). The link between the frontal area and the canyon aspect ratio (e.g. in MORUSES, Porson et al. 2010a) gives reason to assume that the urban morphology profiles are transferable to studying distributed radiation exchange. Anthropogenic heat is another important parameter in the urban energy balance, and the height-dependent total floor plan area $A_P(z)$ may well be a proxy for height-distributed energy consumption.

8.3 Future work

Model evaluation with observational data The case study with the distributed drag model revealed interesting features attributed to urban flows that did not occur with the standard modelling approach, such as the wakes downwind of the city centre. To address the question whether the new parameterization indeed improves the urban wind modelling, the model outputs require evaluation against observational data, ideally vertical profiles of wind speed within the surface layer, and testing for different weather conditions and atmospheric stability.

Towards a fully distributed model Aerodynamic effects of buildings include a reduced wind speed and modified vertical velocity profiles that reflect the shape of the built-up environment. These effects were modelled by the drag force, which is the representation of the momentum sink of urban areas. Buildings also affect momentum transport by generating turbulence and introducing significant dispersive fluxes (as discussed in Chapter 2 and analysed in Chapter 4), however neither of these effects have been explicitly represented in the modified London Model. To account for these effects, the model would require a production term for turbulent kinetic energy due to the buildings and a change in the turbulent mixing and dissipation length scale (cf. Schoetter et al. 2020), as for example included in the multi-layer urban canopy model from Martilli et al. (2002). The modelling of dispersive fluxes, which are for instance important for accurate predictions of scalar

concentrations in urban areas (Martilli et al. 2013; Giometto et al. 2016), has only recently gained attention and requires further research.

Furthermore, the vertical distribution of processes related to the urban energy balance, such as radiation, heat storage, energy usage, and turbulent heat exchange, yet need to be addressed for a fully distributed parameterization of urban areas. A similar modelling framework as presented in this study could be applied for investigating these thermal effects, by using the Urban Landscape Generator to create different morphologies and uDALES with its capabilities of modelling heated street- and building-surfaces (Suter 2018; Grylls et al. 2020). Both the ULG and uDALES are also capable of modelling urban vegetation (Grylls and van Reeuwijk 2021), such that latent heat fluxes in the urban canopy could also be investigated. For that, the addition of urban vegetation profiles (e.g. a leaf area density per height) may be useful.

Broader study and improvements to drag parameterization A pragmatic approach was chosen to model the drag distribution function (the third-order polynomial s), based on the clear relation between the morphology profiles $\zeta(z)$ and the cumulative stress profiles $\tau_D(z)$ of the neighbourhood-scale simulations. However, the study was limited to simulations of nine idealised heterogeneous layouts, and it would be interesting to see how the relation between these profiles emerges for various plan- and frontal-area densities and different flow directions. Equally interesting would be an investigation of this relation for large datasets of realistic morphologies such as from the Kanda et al. (2013) study. The current morphology profiles do not account for shielding effects between buildings. Particularly for clusters of high-rise buildings, this may be an important physical process to represent explicitly, and may further complicate the drag distribution and estimations of total canopy drag.

The parameterization of the total canopy drag τ_0 remains to be addressed. The present study contrasted the roughness-length based approach from the standard model set-up with a bluff-body (i.e. frontal area based) approach from Coceal and Belcher (2004). The results from the case study indicate that there could be a resolution dependence that determines which modelling approach may be more appropriate, and further investigation is

needed to determine at which grid length a different model might be beneficial.

Heterogeneity across scales Most studies on canopy drag including this study currently assume steady-state flows, which means that a neighbourhood is locally in equilibrium with the atmosphere above. However, this is rarely the case for urban areas. Instead, flow over urban landscapes is time-dependent and develops spatially with the transition between the rural and urban interface and between different heterogeneous neighbourhoods, such that the flow closer to the ground may be in a local equilibrium, while regions higher up still carry characteristics from surfaces further upwind. Such a heterogeneous flow is driven by heterogeneity in the urban form and fabric at scales below. The different time- and length-scales over which the boundary-layer flow adjusts are important for a better understanding and modelling of the mixing properties of flow at different locations. Studying developing boundary-layer flows and these time scales could therefore also bring further insight on the implications of different grid resolutions and appropriate modelling approaches.

Bibliography

Aliaga, Daniel G., Carlos A. Vanegas and Bedřich Beneš (2008). Interactive example-based urban layout synthesis. *ACM Transactions on Graphics* 27(5), 1. DOI: 10.1145/1409060.1409113.

Barlow, Janet F. (2014). Progress in observing and modelling the urban boundary layer. *Urban Climate* 10, 216–240. DOI: 10.1016/j.uclim.2014.03.011.

Barlow, Janet F., Martin J. Best, Sylvia I. Bohnenstengel, Peter A. Clark, C. Sue B. Grimmond et al. (2017). Developing a research strategy to better understand, observe and simulate urban atmospheric processes at kilometre to sub-kilometre scales. *Bulletin of the American Meteorological Society*. DOI: 10.1175/bams-d-17-0106.1.

Batty, Michael and Paul A. Longley (1994). *Fractal cities: a geometry of form and function*. Academic press.

Belcher, Stephen E. (2005). Mixing and Transport in Urban Areas. *Philosophical Transactions of the Royal Society A: Mathematical, Physical and Engineering Sciences* 363(1837), 2947–2968. DOI: 10.1098/rsta.2005.1673.

Best, Martin J., Anton Beljaars, J. Polcher and P. Viterbo (2004). A Proposed Structure for Coupling Tiled Surfaces with the Planetary Boundary Layer. *Journal of Hydrometeorology* 5(6), 1271–1278. DOI: 10.1175/JHM-382.1.

Best, Martin J. and C. Sue B. Grimmond (2015). Key Conclusions of the First International Urban Land Surface Model Comparison Project. *Bulletin of the American Meteorological Society* 96(5), 805–819. DOI: 10.1175/bams-d-14-00122.1.

Best, Martin J., M. Pryor, D. B. Clark, Gabriel G. Rooney, R. L. H. Essery et al. (2011). The Joint UK Land Environment Simulator (JULES),

model description – Part 1: Energy and water fluxes. *Geoscientific Model Development* 4(3), 677–699. DOI: 10.5194/gmd-4-677-2011.

Biljecki, Filip, H. Ledoux and J. Stoter (2016). Generation of Multi-LOD 3D City Models in Citygml with the Procedural Modelling Engine Random3Dcity. *ISPRS Annals of Photogrammetry, Remote Sensing and Spatial Information Sciences* IV-4/W1, 51–59. DOI: 10.5194/isprs-annals-iv-4-w1-51-2016.

Bohnenstengel, Sylvia I., Stephen Evans, Peter A. Clark and Stephen E. Belcher (2011). Simulations of the London urban heat island. *Quarterly Journal of the Royal Meteorological Society* 137(659), 1625–1640. DOI: 10.1002/qj.855.

Bohnenstengel, Sylvia I. and Margaret A. Hendry (2016). *Report on implementation and evaluation of MORUSES in the UKV (PS37)*. Tech. rep. Met Office.

Boutle, I. A., Anke Finnenkoetter, Adrian P. Lock and H. Wells (2016). The London Model: forecasting fog at 333 m resolution. *Quarterly Journal of the Royal Meteorological Society* 142(694), 360–371. DOI: 10.1002/qj.2656.

Bunce, R. G. H., C. J. Barr, R. T. Clarke, D. C. Howard and A. M. J. Lane (1990). ITE Land Classification of Great Britain 1990. DOI: 10.5285/ab320e08-faf5-48e1-9ec9-77a213d2907f.

Bush, Mike R., T. Allen, C. Bain, I. Boutle, John M. Edwards et al. (2020). The first Met Office Unified Model–JULES Regional Atmosphere and Land configuration, RAL1. *Geoscientific Model Development* 13(4), 1999–2029. DOI: 10.5194/gmd-13-1999-2020.

Carpentieri, Matteo, Alan G. Robins and Sandro Baldi (2009). Three-Dimensional Mapping of Air Flow at an Urban Canyon Intersection. *Boundary-Layer Meteorology* 133(2), 277–296. DOI: 10.1007/s10546-009-9425-z.

Castro, Ian P. (2017). Are Urban-Canopy Velocity Profiles Exponential? *Boundary-Layer Meteorology* 164(3), 337–351. DOI: 10.1007/s10546-017-0258-x.

Castro, Ian P., Zheng-Tong Xie, Vladimír Fuka, Alan G. Robins, Matteo Carpentieri et al. (2017). Measurements and Computations of Flow in an Urban Street System. *Boundary-Layer Meteorology* 162(2), 207–230. DOI: 10.1007/s10546-016-0200-7.

Cheng, Wai-Chi and Fernando Porté-Agel (2015). Adjustment of Turbulent Boundary-Layer Flow to Idealized Urban Surfaces: A Large-Eddy Simulation Study. *Boundary-Layer Meteorology* 155(2), 249–270. DOI: 10.1007/s10546-015-0004-1.

Clark, D. B., L. M. Mercado, S. Sitch, C. D. Jones, N. Gedney et al. (2011). The Joint UK Land Environment Simulator (JULES), model description – Part 2: Carbon fluxes and vegetation dynamics. *Geoscientific Model Development* 4(3), 701–722. DOI: 10.5194/gmd-4-701-2011.

Coceal, Omduth and Stephen E. Belcher (2004). A canopy model of mean winds through urban areas. *Quarterly Journal of the Royal Meteorological Society* 130(599), 1349–1372. DOI: 10.1256/qj.03.40.

Coceal, Omduth, T. Glyn Thomas, Ian P. Castro and Stephen E. Belcher (2006). Mean Flow and Turbulence Statistics Over Groups of Urban-like Cubical Obstacles. *Boundary-Layer Meteorology* 121(3), 491–519. DOI: 10.1007/s10546-006-9076-2.

Department for Transport (2007). *Manual for streets*. URL: https://www.gov.uk/government/publications/manual-for-streets.

Di Sabatino, Silvana, Laura S. Leo, Rosella Cataldo, Carlo Ratti and Rex E. Britter (2010). Construction of Digital Elevation Models for a Southern European City and a Comparative Morphological Analysis with Respect to Northern European and North American Cities. *Journal of Applied Meteorology and Climatology* 49(7), 1377–1396. DOI: 10.1175/2010jamc2117.1.

Di Sabatino, Silvana, E. Solazzo, P. Paradisi and Rex E. Britter (2008). A Simple Model for Spatially-averaged Wind Profiles Within and Above an Urban Canopy. *Boundary-Layer Meteorology* 127(1), 131–151. DOI: 10.1007/s10546-007-9250-1.

Evans, Stephen, Andrew Hudson-Smith and Michael Batty (2006). 3-D GIS: Virtual London and beyond. An exploration of the 3-D GIS experience involved in the creation of Virtual London. *Cybergeo: European Journal of Geography*. DOI: 10.4000/cybergeo.2871.

Finnigan, John J. (2000). Turbulence in plant canopies. *Annual review of fluid mechanics* 32(1), 519–571. DOI: 10.1146/annurev.fluid.32.1.519.

Fuka, Vladimír, Zheng-Tong Xie, Ian P. Castro, Paul Hayden, Matteo Carpentieri and Alan G. Robins (2018). Scalar Fluxes Near a Tall Building

in an Aligned Array of Rectangular Buildings. *Boundary-Layer Meteorology* 167(1), 53–76. DOI: 10.1007/s10546-017-0308-4.

Garuma, Gemechu Fanta (2018). Review of urban surface parameterizations for numerical climate models. *Urban Climate* 24, 830–851. DOI: https://doi.org/10.1016/j.uclim.2017.10.006.

Gilham, R., Margaret A. Hendry, John M. Edwards, Gabriel G. Rooney and G. A. Folberth (2020). *Coupling the JULES Land Surface Model to the Unified Model*. Unified Model Documentation Paper C03. Met Office.

Giometto, Marco G., Andreas Christen, P. E. Egli, Manuel F. Schmid, R. T. Tooke et al. (2017). Effects of trees on mean wind, turbulence and momentum exchange within and above a real urban environment. *Advances in Water Resources* 106, 154–168. DOI: 10.1016/j.advwatres.2017.06.018.

Giometto, Marco G., Andreas Christen, Charles Meneveau, J. Fang, M. Krafczyk and Marc B. Parlange (2016). Spatial Characteristics of Roughness Sublayer Mean Flow and Turbulence Over a Realistic Urban Surface. *Boundary-Layer Meteorology* 160(3), 425–452. DOI: 10.1007/s10546-016-0157-6.

Gough, Hannah L., M.-F. King, P. Nathan, C. Sue B. Grimmond, Alan G. Robins et al. (2019). Influence of neighbouring structures on building façade pressures: Comparison between full-scale, wind-tunnel, CFD and practitioner guidelines. *Journal of Wind Engineering and Industrial Aerodynamics* 189, 22–33. DOI: 10.1016/j.jweia.2019.03.011.

Grimmond, C. Sue B., Kit Benjamin, William Morrison and Ting Sun (2021). Multi-City Urban Hydrometeorology Database. URL: https://muhd.readthedocs.io/.

Grimmond, C. Sue B., M. Blackett, Martin J. Best, Janet F. Barlow, J.-J. Baik et al. (2010). The International Urban Energy Balance Models Comparison Project: First Results from Phase 1. *Journal of Applied Meteorology and Climatology* 49(6), 1268–1292. DOI: 10.1175/2010jamc2354.1.

Grimmond, C. Sue B. and Timothy R. Oke (1999). Aerodynamic Properties of Urban Areas Derived from Analysis of Surface Form. *Journal of Applied Meteorology* 38(9), 1262–1292. DOI: 10.1175/1520-0450(1999)038<1262:APOUAD>2.0.CO;2.

Grylls, Tom (2019). Simulating air pollution in the urban microclimate. PhD thesis. Imperial College London.

Grylls, Tom, Clémence M. A. Le Cornec, Pietro Salizzoni, Lionel Soulhac, Marc E. J. Stettler and Maarten van Reeuwijk (2019). Evaluation of an operational air quality model using large-eddy simulation. *Atmospheric Environment: X* 3, 100041. DOI: 10.1016/j.aeaoa.2019.100041.

Grylls, Tom, Ivo L. Suter and Maarten van Reeuwijk (2020). Steady-state large-eddy simulations of convective and stable urban boundary layers. *Boundary-Layer Meteorology* 175(3), 309–341. DOI: 10.1007/s10546-020-00508-x.

Grylls, Tom and Maarten van Reeuwijk (2021). Tree model with drag, transpiration, shading and deposition: Identification of cooling regimes and large-eddy simulation. *Agricultural and Forest Meteorology* 298-299, 108288. DOI: 10.1016/j.agrformet.2020.108288.

Hagishima, Aya, Jun Tanimoto, Koji Nagayama and Sho Meno (2009). Aerodynamic Parameters of Regular Arrays of Rectangular Blocks with Various Geometries. *Boundary-Layer Meteorology* 132(2), 315–337. DOI: 10.1007/s10546-009-9403-5.

Harman, Ian N., Janet F. Barlow and Stephen E. Belcher (2004). Scalar Fluxes from Urban Street Canyons Part II: Model. *Boundary-Layer Meteorology* 113(3), 387–410. DOI: 10.1007/s10546-004-6205-7.

Hertwig, Denise (2013). On Aspects of Large-Eddy Simulation Validation for Near-Surface Atmospheric Flows. PhD thesis. Universität Hamburg.

Hertwig, Denise, Hannah L. Gough, C. Sue B. Grimmond, Janet F. Barlow, Christoph W. Kent et al. (2019). Wake Characteristics of Tall Buildings in a Realistic Urban Canopy. *Boundary-Layer Meteorology* 172(2), 239–270. DOI: 10.1007/s10546-019-00450-7.

Hertwig, Denise, C. Sue B. Grimmond, Margaret A. Hendry, Beth Saunders, Zhengda Wang et al. (2020). Urban signals in high-resolution weather and climate simulations: role of urban land-surface characterisation. *Theoretical and Applied Climatology*. DOI: 10.1007/s00704-020-03294-1.

Heus, Thijs, Chiel C. van Heerwaarden, Harm J. J. Jonker, A. Pier Siebesma, S. Axelsen et al. (2010). Formulation of the Dutch Atmospheric Large-Eddy Simulation (DALES) and overview of its applications. *Geoscientific Model Development* 3(2), 415–444. DOI: 10.5194/gmd-3-415-2010.

Hoegh-Guldberg, Ove, Daniela Jacob, Michael Taylor, Marco Bindi, Sally Brown et al. (2018). Impacts of 1.5 °C global warming on natural and

human systems. In: *Global Warming of 1.5° C: An IPCC Special Report on the Impacts of Global Warming of 1.5° C Above Pre-industrial Levels and Related Global Greenhouse Gas Emission Pathways, in the Context of Strengthening the Global Response to the Threat of Climate Change, Sustainable Development, and Efforts to Eradicate Poverty*. Ed. by V. Masson-Delmotte, P. Zhai, H.-O. Pörtner, Roberts D., J. Skea et al. Intergovernmental Panel on Climate Change. URL: https://www.ipcc.ch/sr15/chapter/chapter-3/.

Jackson, P. S. (1981). On the displacement height in the logarithmic velocity profile. *Journal of Fluid Mechanics* 111, 15–25. DOI: 10.1017/S0022112081002279.

Jimenez, Javier (2004). Turbulent Flows over Rough Walls. *Annual Review of Fluid Mechanics* 36(1), 173–196. DOI: 10.1146/annurev.fluid.36.050802.122103.

Kanda, Manabu (2006). Large-Eddy Simulations on the Effects of Surface Geometry of Building Arrays on Turbulent Organized Structures. *Boundary-Layer Meteorology* 118(1), 151–168. DOI: 10.1007/s10546-005-5294-2.

Kanda, Manabu, Atsushi Inagaki, Takashi Miyamoto, Micha Gryschka and Siegfried Raasch (2013). A New Aerodynamic Parametrization for Real Urban Surfaces. *Boundary-Layer Meteorology* 148(2), 357–377. DOI: 10.1007/s10546-013-9818-x.

Kelly, George and Hugh McCabe (2006). A survey of procedural techniques for city generation. *The ITB Journal* 7(2), 5. DOI: 10.21427/D76M9P.

Kent, Christoph W., C. Sue B. Grimmond, Janet F. Barlow, David Gatey, Simone Kotthaus et al. (2017). Evaluation of urban localscale aerodynamic parameters: implications for the vertical profile of wind speed and for source areas. *Boundary-Layer Meteorology* 164(3), 183–213. DOI: 10.1007/s105460170248z.

Kotthaus, Simone and C. Sue B. Grimmond (2018). Atmospheric boundary-layer characteristics from ceilometer measurements. Part 1: A new method to track mixed layer height and classify clouds. *Quarterly Journal of the Royal Meteorological Society* 144(714), 1525–1538. DOI: 10.1002/qj.3299.

Lean, Humphrey W., Janet F. Barlow and Christos H. Halios (2019). The impact of spin-up and resolution on the representation of a clear convective boundary layer over London in order 100 m grid-length versions of the Met Office Unified Model. *Quarterly Journal of the Royal Meteorological Society*. DOI: 10.1002/qj.3519.

Lock, Adrian P., John M. Edwards and I. Boutle (2020). *The Parametrization of Boundary Layer Processes*. Unified Model Documentation Paper 024. Met Office.

MacDonald, R. W. (2000). Modelling The Mean Velocity Profile In The Urban Canopy Layer. *Boundary-Layer Meteorology* 97(1), 25–45. DOI: 10.1023/A:1002785830512.

MacDonald, R. W., R. F. Griffiths and D. J. Hall (1998). An improved method for the estimation of surface roughness of obstacle arrays. *Atmospheric Environment* 32(11), 1857–1864. DOI: 10.1016/S1352-2310(97)00403-2.

Maronga, Björn, S. Banzhaf, C. Burmeister, T. Esch, R. Forkel et al. (2020). Overview of the PALM model system 6.0. *Geoscientific Model Development* 13(3), 1335–1372. DOI: 10.5194/gmd-13-1335-2020.

Martilli, Alberto, Alain Clappier and Mathias W. Rotach (2002). An Urban Surface Exchange Parameterisation for Mesoscale Models. *Boundary-Layer Meteorology* 104(2), 261–304. DOI: 10.1023/A:1016099921195.

Martilli, Alberto, Jose Luis Santiago and Francisco Salamanca (2013). On the representation of urban heterogeneities in mesoscale models. *Environmental Fluid Mechanics* 15(2), 305–328. DOI: 10.1007/s10652-013-9321-4.

Masson, Valéry (2000). A physically-based scheme for the urban energy budget in atmospheric models. *Boundary-layer meteorology* 94(3), 357–397. DOI: 10.1023/A:1002463829265.

Millward-Hopkins, J. T., Alison S. Tomlin, L. Ma, D. B. Ingham and M. Pourkashanian (2011). Estimating Aerodynamic Parameters of Urban-Like Surfaces with Heterogeneous Building Heights. *Boundary-Layer Meteorology* 141(3), 467–467. DOI: 10.1007/s10546-011-9658-5.

Millward-Hopkins, J. T., Alison S. Tomlin, L. Ma, D. B. Ingham and M. Pourkashanian (2012). Aerodynamic Parameters of a UK City Derived

from Morphological Data. *Boundary-Layer Meteorology* 146(3), 447–468. DOI: 10.1007/s10546-012-9761-2.

Moszynska, Maria (2006). *Selected Topics in Convex Geometry*. 1st ed. Birkhäuser Boston.

Neophytou, Marina K.-A., C. N. Markides and P. A. Fokaides (2014). An experimental study of the flow through and over two dimensional rectangular roughness elements: Deductions for urban boundary layer parameterizations and exchange processes. *Physics of Fluids* 26(8), 086603. DOI: 10.1063/1.4892979.

Nepf, Heidi M. (2012). Flow and Transport in Regions with Aquatic Vegetation. *Annual Review of Fluid Mechanics* 44(1), 123–142. DOI: 10.1146/annurev-fluid-120710-101048.

Nikora, Vladimir, Ian McEwan, Stephen McLean, Stephen Coleman, Dubravka Pokrajac and Roy Walters (2007). Double-averaging concept for rough-bed open-channel and overland flows: Theoretical background. *Journal of Hydraulic Engineering* 133(8), 873–883. DOI: 10.1061/(ASCE)0733-9429(2007)133:8(873).

Oke, Timothy R., Gerald Mills, Andreas Christen and James A. Voogt (2017). *Urban Climates*. Cambridge University Press. DOI: 10.1017/9781139016476.

Ordnance Survey (GB) (2005). GB National Outlines. Scale 1:250000, Updated: June 2005, Using: EDINA Digimap Ordnance Survey Service. URL: https://digimap.edina.ac.uk.

Ordnance Survey (GB) (2017). *OS MasterMap Topography Layer – Building Height Attribute Product Guide*. Tech. rep. Ordnance Survey.

Ordnance Survey (GB) (2019a). OS MasterMap Building Height Attribute. Scale 1:2500, Updated: April 2019, Using: EDINA Digimap Ordnance Survey Service. URL: https://digimap.edina.ac.uk.

Ordnance Survey (GB) (2019b). OS MasterMap Topography Layer. Scale 1:1250, Updated: May 2019, Using: EDINA Digimap Ordnance Survey Service. URL: https://digimap.edina.ac.uk.

Ordnance Survey (GB) (2020). Boundary-Line. Scale 1:2500, Updated: March 2020, Using: EDINA Digimap Ordnance Survey Service. URL: https://digimap.edina.ac.uk.

Parish, Yoav I. H. and Pascal Müller (2001). Procedural modeling of cities. In: *Proceedings of the 28th annual conference on Computer graphics and interactive techniques*. ACM, pp. 301–308. DOI: 10.1145/383259.383292.

Pope, Stephen B. (2000). *Turbulent flows*. Cambridge University Press.

Porson, Aurore, Peter A. Clark, Ian N. Harman, Martin J. Best and Stephen E. Belcher (2010a). Implementation of a new urban energy budget scheme in the MetUM. Part I: Description and idealized simulations. *Quarterly Journal of the Royal Meteorological Society* 136(651), 1514–1529. DOI: 10.1002/qj.668.

Porson, Aurore, Peter A. Clark, Ian N. Harman, Martin J. Best and Stephen E. Belcher (2010b). Implementation of a new urban energy budget scheme into MetUM. Part II: Validation against observations and model intercomparison. *Quarterly Journal of the Royal Meteorological Society* 136(651), 1530–1542. DOI: 10.1002/qj.572.

Raupach, Michael R. (1994). Simplified expressions for vegetation roughness length and zero-plane displacement as functions of canopy height and area index. *Boundary-Layer Meteorology* 71(1), 211–216. DOI: 10.1007/BF00709229.

Raupach, Michael R. and Roger H. Shaw (1982). Averaging procedures for flow within vegetation canopies. *Boundary-Layer Meteorology* 22(1), 79–90. DOI: 10.1007/BF00128057.

Resler, Jaroslav, Pavel Krč, Michal Belda, Pavel Juruš, Nina Benešová et al. (2017). PALM-USM v1. 0: A new urban surface model integrated into the PALM large-eddy simulation model. *Geoscientific Model Development* 10(10), 3635. DOI: 10.5194/gmd-10-3635-2017.

Rooney, Gabriel G. and F. Jorge Bornemann (2013). The performance of FLake in the Met Office Unified Model. *Tellus A: Dynamic Meteorology and Oceanography* 65(1), 21363. DOI: 10.3402/tellusa.v65i0.21363.

Salim, Mohamed H., K. Heinke Schlünzen, David Grawe, Marita Boettcher, Andrea M. U. Gierisch and Björn H. Fock (2017). The Microscale Obstacle Resolving Meteorological Model MITRAS: Model Theory. *Geosci. Model Dev. Discuss.* DOI: 10.5194/gmd-2017-250.

Schmid, Manuel F., Gregory A. Lawrence, Marc B. Parlange and Marco G. Giometto (2019). Volume Averaging for Urban Canopies. *Boundary-Layer Meteorology* 173(3), 349–372. DOI: 10.1007/s10546-019-00470-3.

Schoetter, R., Y. T. Kwok, C. de Munck, K. K. L. Lau, W. K. Wong and V. Masson (2020). Multi-layer coupling between SURFEX-TEB-v9.0 and Meso-NH-v5.3 for modelling the urban climate of high-rise cities. *Geoscientific Model Development* 13(11), 5609–5643. DOI: 10.5194/gmd-13-5609-2020.

Sievers, Uwe (2016). *Das kleinskalige Strömungsmodell MUKLIMO_3*. Teil 2: Thermodynamische Erweiterungen. Deutscher Wetterdienst.

Simón-Moral, Andrés, Anurag Dipankar, Matthias Roth, Claudio Sánchez, Erik Velasco and Xiang-Yu Huang (2019). Application of MORUSES single-layer urban canopy model in a tropical city: Results from Singapore. *Quarterly Journal of the Royal Meteorological Society*. DOI: 10.1002/qj.3694.

Simon, Helge (2016). Modeling urban microclimate - Development, implementation and evaluation of new and improved calculation methods for the urban microclimate model ENVI-met. PhD thesis. Johannes Gutenberg-Universität.

Smelik, Ruben M., Tim Tutenel, Rafael Bidarra and Bedřich Beneš (2014). A survey on procedural modelling for virtual worlds. In: *Computer Graphics Forum*. Vol. 33. (6). Wiley Online Library, pp. 31–50. DOI: 10.1111/cgf.12276.

Stull, Roland B. (1988). *An introduction to boundary layer meteorology*. Springer Science & Business Media.

Suter, Ivo L. (2018). Simulating the impact of blue-green infrastructure on the microclimate of urban areas. PhD thesis. Imperial College London. DOI: 10.25560/78715.

Sützl, Birgit S., Gabriel G. Rooney, Anke Finnenkoetter, Sylvia I. Bohnenstengel, C. Sue B. Grimmond and Maarten van Reeuwijk (2021a). Distributed urban drag parameterization for sub-kilometre scale numerical weather prediction. in preparation.

Sützl, Birgit S., Gabriel G. Rooney and Maarten van Reeuwijk (2021b). Drag distribution in idealized heterogeneous urban environments. *Boundary-Layer Meteorology* 178, 225–248. DOI: 10.1007/s10546-020-00567-0.

Sützl, Birgit S. and Maarten van Reeuwijk (2020). Urban Landscape Generator. DOI: 10.5281/zenodo.3747475. URL: https://github.com/bss116/citygenerator.

Tang, Yongming, Humphrey W. Lean and F. Jorge Bornemann (2013). The benefits of the Met Office variable resolution NWP model for forecasting convection. *Meteorological Applications* 20(4), 417–426. DOI: 10.1002/met.1300.

Tennekes, Hendrik (1973). The logarithmic wind profile. *Journal of the Atmospheric Sciences* 30(2), 234–238. DOI: 10.1175/1520-0469(1973)030<0234:TLWP>2.0.CO;2.

Theeuwes, Natalie E., Gert-Jan Steeneveld, Reinder J. Ronda, B. G. Heusinkveld, L. W. A. van Hove and Albert A. M. Holtslag (2014). Seasonal dependence of the urban heat island on the street canyon aspect ratio. *Quarterly Journal of the Royal Meteorological Society* 140(684), 2197–2210. DOI: 10.1002/qj.2289.

Tomas, Jasper M. (2016). Obstacle-resolving large-eddy simulation of dispersion in urban environments Effects of stability and roughness geometry. PhD thesis. TU Delft. DOI: 10.4233/uuid:5d93a697-be49-4f63-b871-b763bc327139.

Tomas, Jasper M., M. J. B. M. Pourquie and Harm J. J. Jonker (2015). The influence of an obstacle on flow and pollutant dispersion in neutral and stable boundary layers. *Atmospheric Environment* 113, 236–246. DOI: 10.1016/j.atmosenv.2015.05.016.

Tomas, Jasper M., M. J. B. M. Pourquie and Harm J. J. Jonker (2016). Stable Stratification Effects on Flow and Pollutant Dispersion in Boundary Layers Entering a Generic Urban Environment. *Boundary-Layer Meteorology* 159(2), 221–239. DOI: 10.1007/s10546-015-0124-7.

United Nations (2019). *World Urbanization Prospects: The 2018 Revision*. Tech. rep. Department of Economic and Social Affairs, Population Division. URL: https://population.un.org/wup.

Uno, I., X.-M. Cai, D. G. Steyn and S. Emori (1995). A simple extension of the Louis method for rough surface layer modelling. *Boundary-Layer Meteorology* 76(4), 395–409. DOI: 10.1007/BF00709241.

van Reeuwijk, Maarten, J. Christos Vassilicos and John Craske (2021). Unified description of turbulent entrainment. *Journal of Fluid Mechanics* 908, A12. DOI: 10.1017/jfm.2020.836.

Vreman, A. W. (2004). An eddy-viscosity subgrid-scale model for turbulent shear flow: Algebraic theory and applications. *Physics of fluids* 16(10), 3670–3681. DOI: 10.1063/1.1785131.

Walters, D., A. J. Baran, I. Boutle, M. Brooks, P. Earnshaw et al. (2019). The Met Office Unified Model Global Atmosphere 7.0/7.1 and JULES Global Land 7.0 configurations. *Geoscientific Model Development* 12(5), 1909–1963. DOI: 10.5194/gmd-12-1909-2019.

Whitaker, Stephen (1985). A Simple Geometrical Derivation of the Spatial Averaging Theorem. *Chemical Engineering Education*.

Wood, N., Andrew R. Brown and F. E. Hewer (2001). Parametrizing the effects of orography on the boundary layer: An alternative to effective roughness lengths. *Quarterly Journal of the Royal Meteorological Society* 127(573), 759–777. DOI: https://doi.org/10.1002/qj.49712757303.

Xie, Zheng-Tong, Omduth Coceal and Ian P. Castro (2008). Large-Eddy Simulation of Flows over Random Urban-like Obstacles. *Boundary-Layer Meteorology* 129(1), 1–23. DOI: 10.1007/s10546-008-9290-1.

Xie, Zheng-Tong and Vladimír Fuka (2018). A Note on Spatial Averaging and Shear Stresses Within Urban Canopies. *Boundary-Layer Meteorology* 167(1), 171–179. DOI: 10.1007/s10546-017-0321-7.

Zaki, S. Ahmad, Aya Hagishima, Jun Tanimoto and Naoki Ikegaya (2011). Aerodynamic Parameters of Urban Building Arrays with Random Geometries. *Boundary-Layer Meteorology* 138(1), 99–120. DOI: 10.1007/s10546-010-9551-7.

A

Decomposing the product of flow variables

Applying the decomposition to the product of two variables, e.g. the wind components u_i and u_j, yields

$$u_i u_j = \left(\langle \overline{u}_i \rangle + \overline{u}_i'' + u_i'\right)\left(\langle \overline{u}_j \rangle + \overline{u}_j'' + u_j'\right) \tag{A.1}$$

$$= \langle \overline{u}_i \rangle \langle \overline{u}_j \rangle + \langle \overline{u}_i \rangle \overline{u}_j'' + \langle \overline{u}_i \rangle u_j' + \overline{u}_i'' \langle \overline{u}_j \rangle + \overline{u}_i'' \overline{u}_j'' \tag{A.2}$$

$$+ \overline{u}_i'' u_j' + u_i' \langle \overline{u}_j \rangle + u_i' \overline{u}_j'' + u_i' u_j'. \tag{A.3}$$

A time-space average of the product then gives

$$\langle \overline{u_i u_j} \rangle = \langle \overline{u}_i \rangle \langle \overline{u}_j \rangle + \langle \overline{u}_i \rangle \langle \overline{u}_j'' \rangle + \langle \overline{u}_i \rangle \langle \overline{u_j'} \rangle + \langle \overline{u}_i'' \rangle \langle \overline{u}_j \rangle + \langle \overline{u}_i'' \overline{u}_j'' \rangle \tag{A.4}$$

$$+ \langle \overline{\overline{u}_i'' u_j'} \rangle + \langle \overline{u_i'} \rangle \langle \overline{u}_j \rangle + \langle \overline{u_i' \overline{u}_j''} \rangle + \langle \overline{u_i' u_j'} \rangle, \tag{A.5}$$

in which we extracted constant terms $\langle \overline{u} \rangle$ from the averages and applied $\overline{\overline{u}''} = \overline{u}''$. Since $\overline{u'} = 0$ and $\langle \overline{u}'' \rangle = 0$ and space and time averages commute, we have

$$\langle \overline{u_i u_j} \rangle = \langle \overline{u}_i \rangle \langle \overline{u}_j \rangle + 0 + 0 + 0 + \langle \overline{u}_i'' \overline{u}_j'' \rangle \tag{A.6}$$

$$+ \langle \overline{\overline{u}_i'' u_j'} \rangle + 0 + \langle \overline{u_i' \overline{u}_j''} \rangle + \langle \overline{u_i' u_j'} \rangle. \tag{A.7}$$

Further since $\overline{u}''$ does not depend on time we can extract the term from the time average and see that $\langle \overline{\overline{u}_i'' u_j'} \rangle = \langle \overline{u}_i'' \overline{u_j'} \rangle$ and $\langle \overline{u_i' \overline{u}_j''} \rangle = \langle \overline{u_i'} \overline{u}_j'' \rangle$ and thus the

cross-terms are also zero. We obtain the averaged product

$$\langle \overline{u_i u_j} \rangle = \langle \overline{u}_i \rangle \langle \overline{u}_j \rangle + \langle \overline{u}_i'' \overline{u}_j'' \rangle + \langle \overline{u_i' u_j'} \rangle. \tag{A.8}$$

which decomposes into the sum of product of mean quantities, product of spatial deviations of temporal mean and product of fluctuations, which are all generally nonzero.

B

Building-width projections

The projection of vector $\mathbf{x} = (x_1, x_2)$ onto unit wind vector $\mathbf{e}_{\perp\theta} = (\sin\theta, -\cos\theta)$ with wind angle θ is expressed by the matrix-vector product $Q\mathbf{x}$ with the projection matrix

$$Q = \mathbf{e}_{\perp\theta}{\mathbf{e}_{\perp\theta}}^T = \begin{pmatrix} (\sin\theta)^2 & -\sin\theta\cos\theta \\ -\sin\theta\cos\theta & (\cos\theta)^2 \end{pmatrix}. \tag{B.1}$$

The distance between the vectors $\mathbf{x} = (x_1, x_2)$ and $\mathbf{y} = (y_1, y_2)$ after their projection onto $\mathbf{e}_{\perp\theta}$ is:

$$\begin{aligned}
\|Q\mathbf{x} - Q\mathbf{y}\| = \Big(& [(\sin\theta)^2(x_1 - y_1) - \sin\theta\cos\theta(x_2 - y_2)]^2 && \text{(B.2)} \\
& + [-\sin\theta\cos\theta(x_1 - y_1) + (\cos\theta)^2(x_2 - y_2)]^2 \Big)^{1/2} && \text{(B.3)} \\
= \Big(& (\sin\theta)^4(x_1 - y_1)^2 - 2(\sin\theta)^3\cos\theta(x_1 - y_1)(x_2 - y_2) && \text{(B.4)} \\
& + (\sin\theta)^2(\cos\theta)^2(x_2 - y_2)^2 && \text{(B.5)} \\
& + (\sin\theta)^2(\cos\theta)^2(x_1 - y_1)^2 && \text{(B.6)} \\
& - 2\sin\theta(\cos\theta)^3(x_1 - y_1)(x_2 - y_2) && \text{(B.7)} \\
& + (\cos\theta)^4(x_2 - y_2)^2 \Big)^{1/2} && \text{(B.8)} \\
= \Big(& (\sin\theta)^2(x_1 - y_1)^2[(\sin\theta)^2 + (\cos\theta)^2] && \text{(B.9)} \\
& - 2\sin\theta\cos\theta(x_1 - y_1)(x_2 - y_2)[(\sin\theta)^2 + (\cos\theta)^2] && \text{(B.10)} \\
& + (\cos\theta)^2(x_2 - y_2)^2[(\sin\theta)^2 + (\cos\theta)^2] \Big)^{1/2} && \text{(B.11)}
\end{aligned}$$

$$= \Big([\sin\theta(x_1 - y_1)]^2 - 2\sin\theta\cos\theta(x_1 - y_1)(x_2 - y_2) \tag{B.12}$$

$$+ [\cos\theta(x_2 - y_2)]^2 \Big)^{1/2} \tag{B.13}$$

$$= |\sin\theta(x_1 - y_1) - \cos\theta(x_2 - y_2)|. \tag{B.14}$$

C

MORUSES parameterizations

Ground heat flux

The canyon ground heat flux $Q_{G,c}$ is represented by conductive coupling of the road surface to the soil with (Bohnenstengel and Hendry 2016)

$$Q_{G,c}(T_c, T_s) = -\lambda \frac{2(T_s - T_c)}{\Delta z_s}, \tag{C.1}$$

where $T_c(t)$ is the temperatures of the canyon tile, $T_s(t)$ the temperature and Δz_s the material thickness of the soil, and λ is the thermal conductivity parameter set by MORUSES. The roof tile is radiatively coupled to the soil by a ground heat flux

$$Q_{G,r}(T_r, T_s) = \sigma T_r^4 - \sigma T_s^4, \tag{C.2}$$

where $T_r(t)$ is the temperature of the roof tile and σ the Stefan–Boltzmann constant.

Net radiation

Radiative heat exchange Q_k^* between the atmosphere and the tile ($k = c$ for urban canyon tile, $k = r$ for urban roof tile) is formulated using an

effective albedo α_k for incoming net shortwave radiation K_k^* and an effective emissivity ϵ_k for outgoing net longwave radiation L_k^* (Porson et al. 2010a):

$$Q_k^* = K_k^* + L_k^* = (1 - \alpha_k)K^{\downarrow} + \epsilon_k(L^{\downarrow} - \sigma T_k^4) \tag{C.3}$$

with tile surface temperature $T_k(t)$, incident solar radiation density $K^{\downarrow}(t)$, and downward longwave radiation density $L^{\downarrow}(t)$. Albedo α_r and emissivity ϵ_r for the urban roof tile are a directly derived from the material properties. The effective canyon albedo is calculated by

$$\alpha_c = (\Psi_b + \Upsilon_b) + \frac{2H}{W}(\Psi_w + \Upsilon_w), \tag{C.4}$$

where $\Psi_b(t)$ and $\Psi_w(t)$ represent the fractions of incoming solar radiation reaching the road and the walls respectively, after sky diffusion and shadowing effects. The multi-reflections of solar radiation within the canyon is represented by the net exchange-diffuse radiation densities $\Upsilon_b(t)$ for road and $\Upsilon_w(t)$ walls. These terms, and therefore also the canyon albedo, vary with solar zenith angle (Hertwig et al. 2020). Similar considerations are used to define an effective canyon emissivity ϵ_c with the same urban geometry weighting (see Porson et al. 2010a).

D

London's morphology at different resolutions

This appendix illustrates how urban morphologies change with the size of the unit area, that is with the grid resolution of NWP models. The morphologies are calculated from the Ordnance Survey building data (Section 5.2.1), approximating the 10 × 15-km^2 central London area (Section 7.2.1) at four different resolutions: 1.5 km, 1 km, 333 m, and 100 m. The 1.5 km resolution showcases the level of detail for UKV inputs (although note that the grid does not necessarily align with the UKV grid). The 1 km resolution corresponds to the level of detail for which the empirical relations were derived (Bohnenstengel et al. 2011), which are the basis of the UM's standard morphology input datasets, and the 100 m resolution corresponds to an experimental set-up of the London Model which has been used to investigate the effects of high resolutions on boundary-layer dynamics (cf. Lean et al. 2019). Note that the 333-m resolution data are not post-processed, and therefore may be slightly different from the data in the case study, which were adjusted to the minimum values of the standard LM inputs. Aerodynamic roughness parameters are further derived from these morphologies using the MacDonald et al. (1998) parameterization.

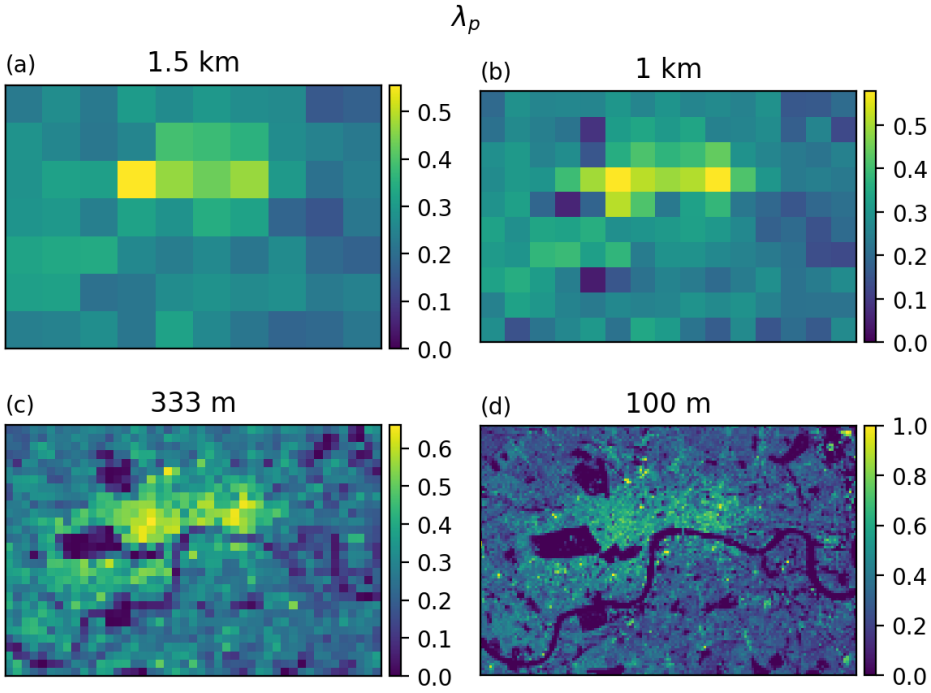

Figure D.1: Plan area index λ_p of central London for (a) 1.5 km, (b) 1 km, (c) 333 m, and (d) 100 m resolution. Note the different colour scales.

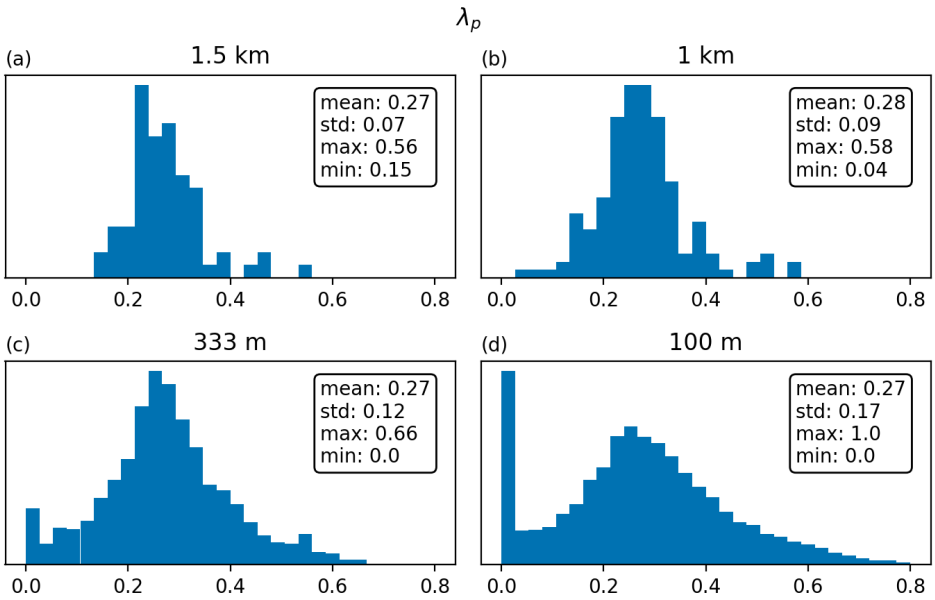

Figure D.2: Distributions of plan area index λ_p grid-box values in central London for (a) 1.5 km, (b) 1 km, (c) 333 m, and (d) 100 m resolution.

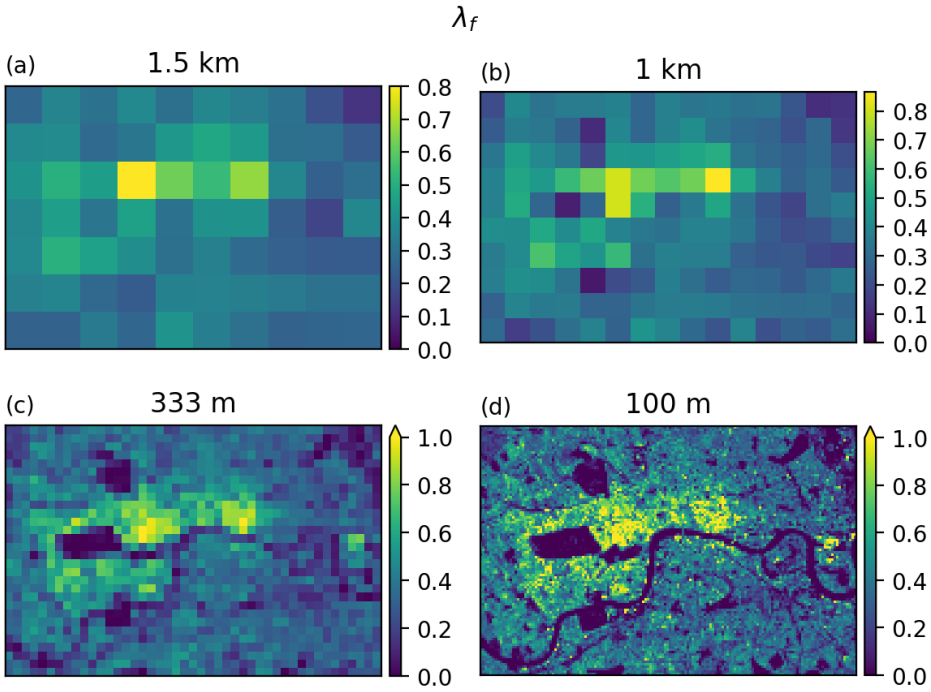

Figure D.3: Frontal area index λ_f of central London for (a) 1.5 km, (b) 1 km, (c) 333 m, and (d) 100 m resolution. Note the different colour scales.

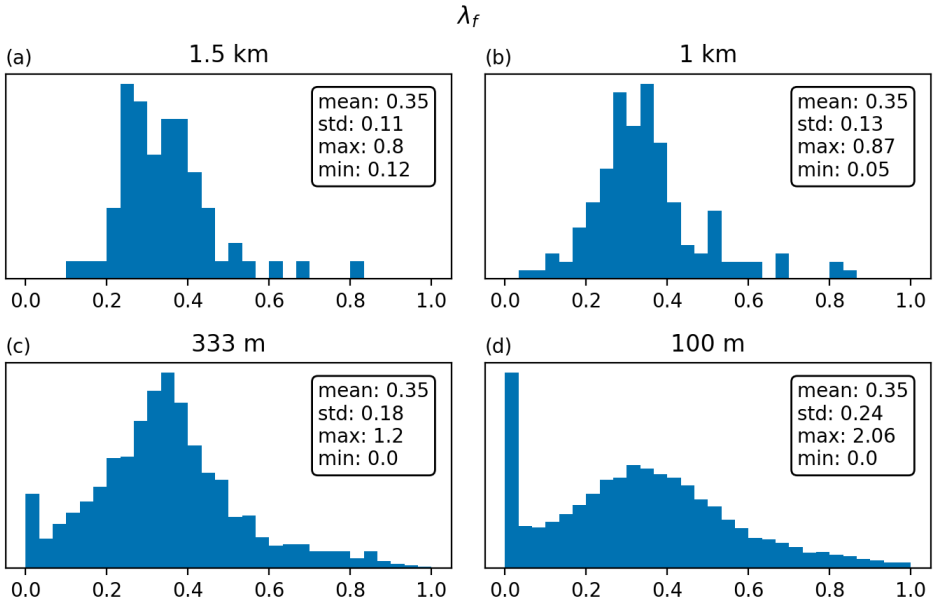

Figure D.4: Distributions of frontal area index λ_f grid-box values in central London for (a) 1.5 km, (b) 1 km, (c) 333 m, and (d) 100 m resolution.

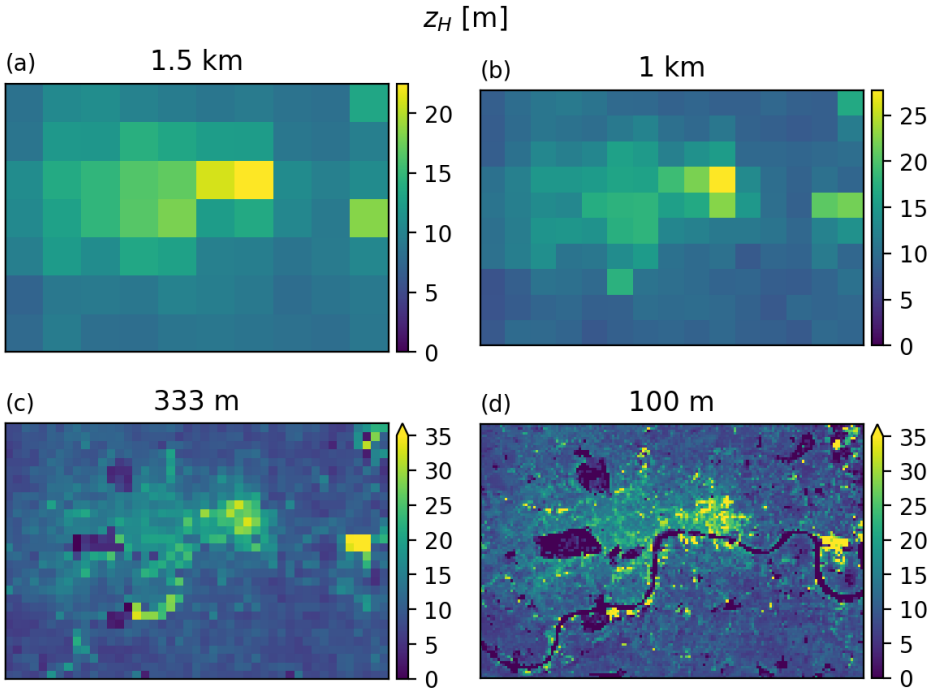

Figure D.5: Mean building height z_H of central London for (a) 1.5 km, (b) 1 km, (c) 333 m, and (d) 100 m resolution. Note the different colour scales.

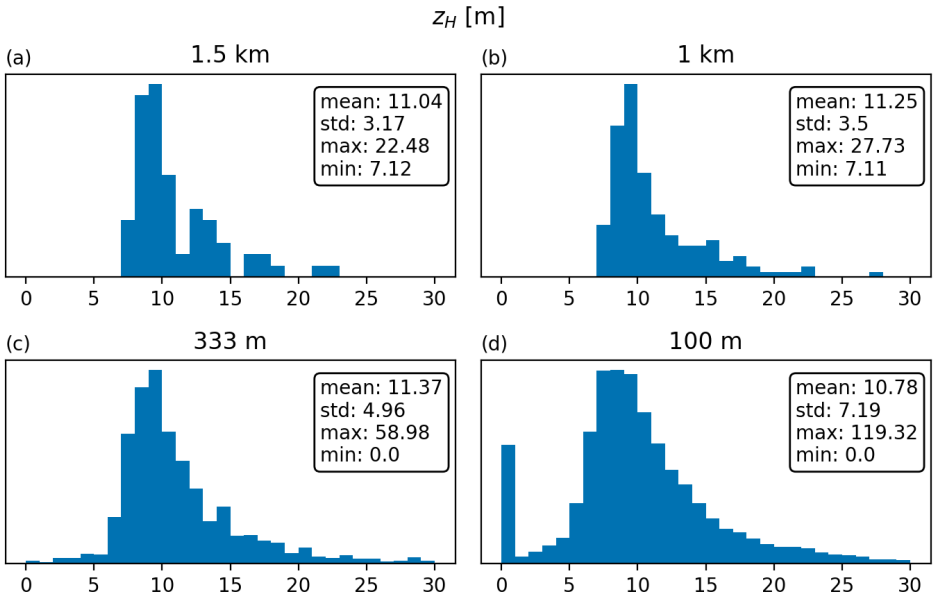

Figure D.6: Distributions of mean building height z_H in central London for (a) 1.5 km, (b) 1 km, (c) 333 m, and (d) 100 m resolution.

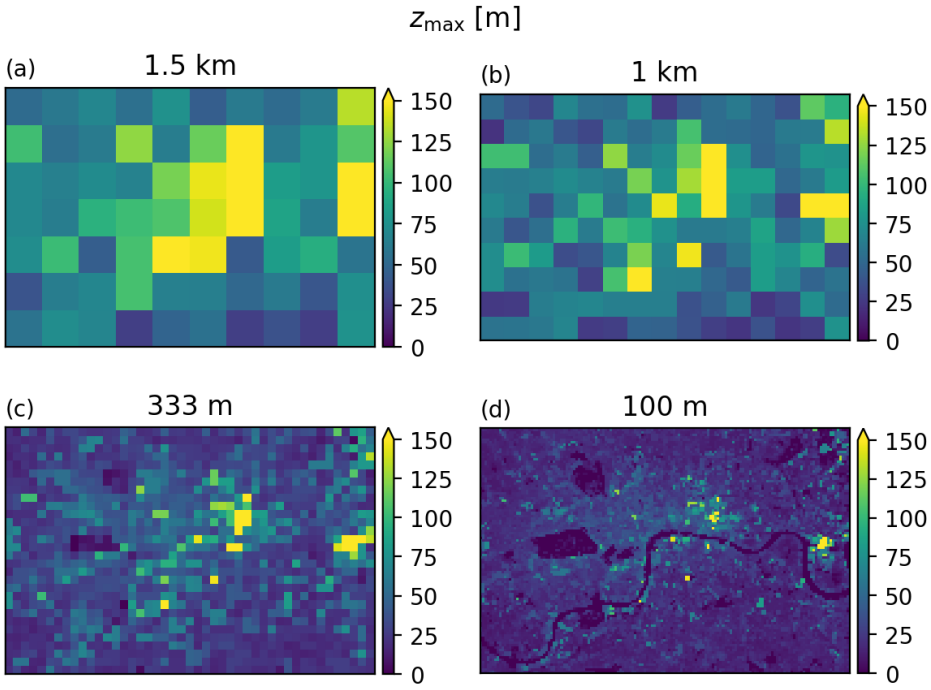

Figure D.7: Maximum building height z_{max} of central London for (a) 1.5 km, (b) 1 km, (c) 333 m, and (d) 100 m resolution.

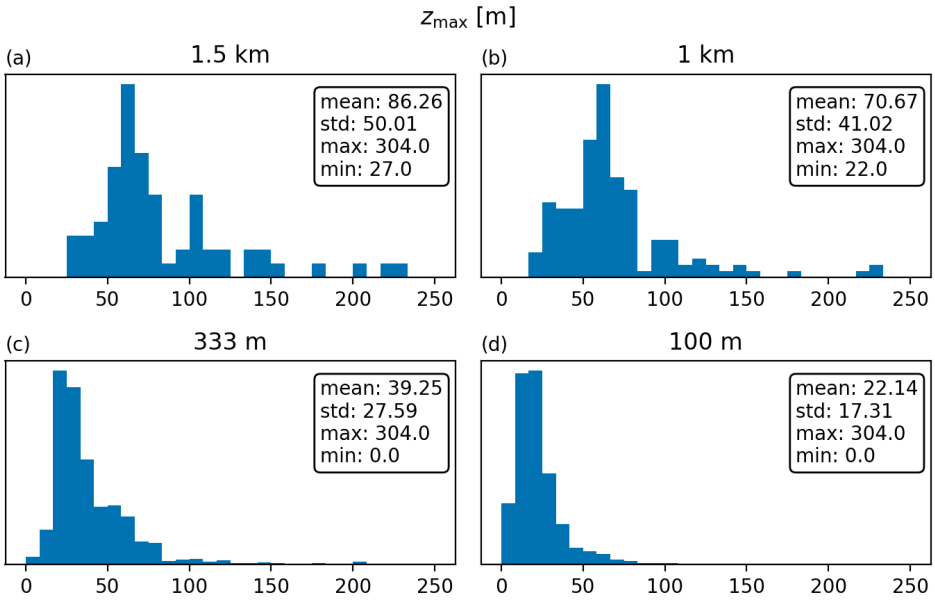

Figure D.8: Distributions of maximum building height z_{max} in central London for (a) 1.5 km, (b) 1 km, (c) 333 m, and (d) 100 m resolution.

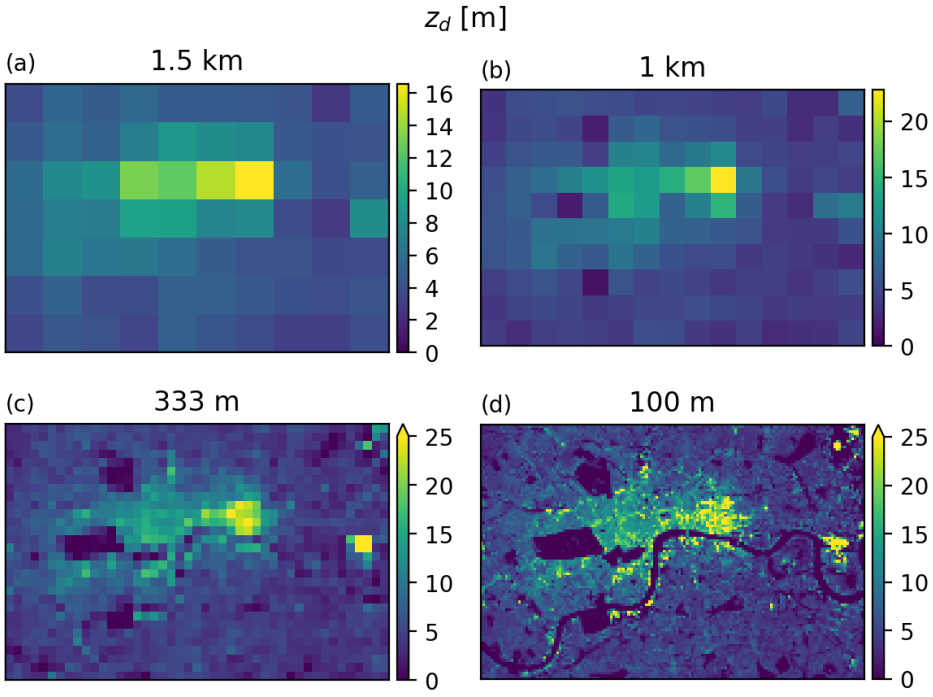

Figure D.9: MacDonald et al. (1998) displacement height z_d for (a) 1.5 km, (b) 1 km, (c) 333 m, and (d) 100 m resolution. Note the different colour scales.

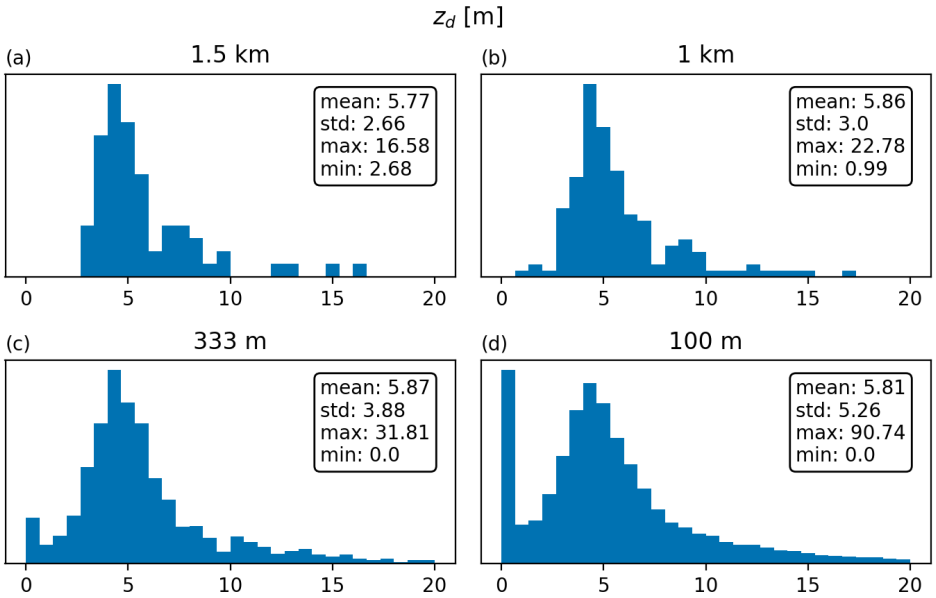

Figure D.10: Distributions of the MacDonald et al. (1998) displacement height z_d in central London for (a) 1.5 km, (b) 1 km, (c) 333 m, and (d) 100 m resolution.

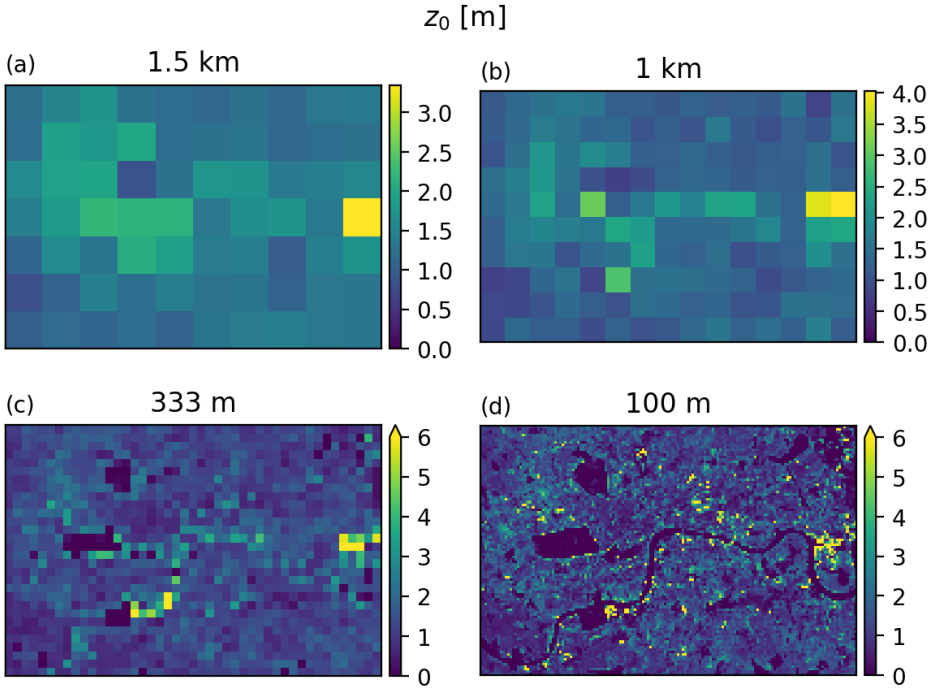

Figure D.11: MacDonald et al. (1998) roughness length z_0 for (a) 1.5 km, (b) 1 km, (c) 333 m, and (d) 100 m resolution. Note the different colour scales.

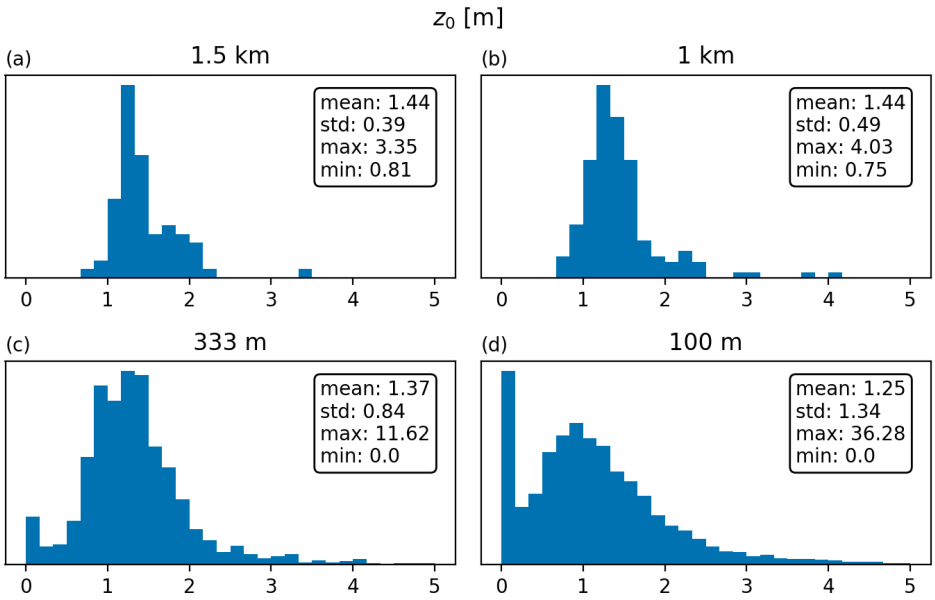

Figure D.12: Distributions of the MacDonald et al. (1998) roughness length z_0 in central London for (a) 1.5 km, (b) 1 km, (c) 333 m, and (d) 100 m resolution.